Low Temperature Quasiparticle Transport in d-Wave Superconductors

by

Adam Craig Durst

M.Phil., Cambridge University 1997
B.S.E., Princeton University 1996

Submitted to the Department of Physics
in partial fulfillment of the requirements for the degree of

Doctor of Philosophy

at the

MASSACHUSETTS INSTITUTE OF TECHNOLOGY

September 2002

Author ..... Adam Durst
Department of Physics
July 17, 2002

Certified by .....
Patrick A. Lee
William and Emma Rogers Professor of Physics
Thesis Supervisor

Accepted by ..... Thomas J. Greytak
Thomas J. Greytak
Professor, Associate Department Head for Education

Low Temperature Quasiparticle Transport in d-Wave Superconductors

by

Adam Craig Durst

Submitted to the Department of Physics
on July 17, 2002, in partial fulfillment of the
requirements for the degree of
Doctor of Philosophy

Abstract

Experiments have now established that the order parameter (gap) in the high-T_c cuprate superconductors exhibits d-wave symmetry, vanishing at four nodal points on the Fermi surface. Near each of these four gap nodes, quasiparticles are easily excited and behave more like massless relativistic particles than electrons in a metal. In this thesis, we study the transport properties of these nodal quasiparticles, providing theoretical interpretations for the results of low temperature thermal and (microwave) electrical transport experiments in the cuprates.

We begin by considering the very low temperature regime in which transport is dominated by quasiparticles induced by the very presence of impurities. This is known as the universal limit because prior calculations indicate that the transport coefficients obtain universal (scattering-independent) values. We improve upon prior results by including the contribution of vertex corrections and find that while the electrical conductivity obtains a scattering-dependent correction, the thermal and spin conductivity maintain their universal values.

We then focus on the microwave electrical conductivity and consider the slightly higher temperature regime where quasiparticles are excited thermally. Since measurements in detwinned samples yield results that are inconsistent with simple models of impurity scattering, we hypothesize that line defects, remnant from the process of removing twin boundaries, may provide an additional scattering mechanism. We calculate the self-energy and microwave conductivity due to line defect scattering and obtain results that agree well with experiment.

Finally, we turn on a magnetic field and consider thermal transport in the mixed (vortex) state. In the weak-field regime, the thermal conductivity tensor can be expressed in terms of the cross section for quasiparticle scattering from a single vortex. We calculate this cross section and thereby obtain both the longitudinal thermal conductivity and the thermal Hall conductivity in surprisingly good qualitative agreement with the measured data. The transparent nature of our calculation allows us to obtain a physical understanding of the features seen in experiments.

Thesis Supervisor: Patrick A. Lee
Title: William and Emma Rogers Professor of Physics

Acknowledgments

I have had the great fortune to share the past few years with a fantastic group of people. Without their assistance, tutelage, kindness, and friendship, the research reported in this thesis would not have been possible.

I would like to begin by expressing my sincere gratitude to my advisor, Patrick Lee. I consider it an honor and a privilege to have had the opportunity to work with and learn from him. Patrick has an incredible physical intuition. While most of us understand physics through the reflection of formulas and equations, he has the amazing ability, through some combination of experience and genius, to understand physics directly, capturing its essence in his mind. This is a trait which I sincerely hope can be learned, but which I fear is simply a gift bestowed by nature. Any success I have had as his student has been achieved by taking hold of one of his many ideas and spending the next six months doing the mathematics. But what is most impressive about Patrick, and what I am most grateful for, is his simple kindness, and in the face of his tremendous accomplishments, his graceful humility. Beyond just teaching me physics, he has shown me the right way to be a physicist.

In addition to Patrick, I would like to thank all of the other professors from whom I have taken courses at MIT: Nihat Berker, Daniel Freedman, Kerson Huang, John Joannopoulos, Mehran Kardar, Leonid Levitov, and Xiao-Gang Wen. Their detailed lectures and thoughtful guidance were sincerely appreciated. In many cases, their lecture notes and problem sets have served as a trusted reference, reviewed often through the course of my research. Thanks also to Senthil Todadri for his advice while I was teaching the recitations for his course, helpful conversations about my research, and his contagiously enthusiastic disposition. I am also grateful to Senthil and Marc Kastner for agreeing to serve on my thesis committee.

The CMT corridor has been an inspirational and fun place to do physics, not only because of its fashion-savvy green and purple carpets, but also because of the great people who inhabit it. Let me start by thanking my officemates, the residents of room 12-105 whose stay here has coincided with mine. They are, in chronological order: Catherine Pepin, Jan Brinkmann, Olav Syljuasen, Sasha Abanov, Kevin Beach, Jung-Tsung Shen, Jun Kishine, Patrick Sit, Ashvin Vishwanath, and Carsten Honerkamp. These individuals have provided a tremendous resource for me, answering my incessant questions, helping to plug the many holes in my physics knowledge, providing a sounding board for new ideas, and infusing a sense of camaraderie into what can sometimes be a rather solitary occupation. Moving beyond the walls of my office, I want to extend my thanks to all of the other students, postdocs, and visitors who I have had the pleasure to interact with on a daily basis. While there are too many to name them all, the list includes: Misha Fogler, Ilya Gruzberg, Zoran Hadzibabic, Karl Hanf, Casey Huang, Dima Ivanov, Yacov Kantor, Don Kim, Vincent Liu, Olexei Motrunich, Joel Moore, Yoshifumi Morita, Dima Novikov, Mehmet Oktel, Michelle Povinelli, Walter Rantner, Tiago Ribeiro, Darren Segall, Alex Seidel, Maksim Skorobogatiy, Joshua Weitz, and Dicle Yesilleten.

Several individuals require special thanks. First among these is my fellow graduate student and long-time officemate, Kevin Beach. Kevin has made tremendous

contributions to both my research and my peace of mind. He willingly listens as I bore him with the daily minutia of my calculations, provides insightful answers to my countless questions, and makes my workday a lot of fun. I am also grateful to Walter Rantner, who began graduate school with me, has been a friend and colleague for five years, and will be graduating with me this summer. Thanks also to Sasha Abanov, who, during his postdoc at MIT, was always willing to share with me his formidable knowledge of physics. Finally, I would like to express my sincere gratitude to Ashvin Vishwanath, who I had the privilege of collaborating with on the research discussed in Chapter 4. Ashvin, like Patrick, has the gift of a well-tuned physical intuition. I look forward to the day when he is a big shot in our field and I can proudly brag that I knew him early on.

There are also many people outside of MIT to whom I owe a debt of gratitude. Thanks to John Berlinsky and Catherine Kallin for helpful conversations that contributed to the work in Chapters 2 and 3. Thanks also to Louis Taillefer, Doug Bonn, Phuan Ong (and all their collaborators) whose beautiful experiments served as motivation for the calculations in Chapters 2, 3, and 4 respectively. I am particularly grateful to Richard Harris (at UBC) for providing the YBCO crystal detwinning information presented in Chapter 3 and to Yuexing Zhang (at Princeton) for providing the unpublished longitudinal thermal conductivity data that was used in Chapter 4. The Fall semester of my fourth year was spent as a graduate fellow at the Institute for Theoretical Physics at UCSB. I thoroughly enjoyed the experience on both a professional and personal level and am extremely grateful to the ITP and everyone I encountered there. In particular, thanks to my officemate, Seungwon Lee, as well as Ehud Altman, Leon Balents, David Carpentier, Matthew Fisher, Jung Hoon Han, Jiangping Hu, Courtney Lannert, and Smitha Vishveshwara. Also, I would like to thank my undergraduate advisor, Ravin Bhatt, for his mentorship and continued support, as well as my high school physics teachers, Angela Lukaszewski and Richard Lesse, for getting me interested in physics in the first place.

Lastly, it is my great pleasure to thank my parents, Lynne and David, and my sister, Alyssa, for their constant support, encouragement, and love throughout the decade-long process of my higher education. Above all, I thank my wonderful wife, Sarah, who is my inspiration, my best friend, and the love of my life.

Contents

List of Figures

Chapter 1

Introduction

To learn the transport by the pain,
As blind men learn the sun ...

Emily Dickinson

Mutual was the sudden transport;
Breathless questions followed fast,
Years contracting to a moment,
Each word greedier than the last.

William Wordsworth

1.1 Background and Motivation

Superconductivity is the quintessential example of a macroscopic quantum phenomenon. It was first discovered in 1911 when Kamerlingh Onnes [1] cooled mercury to liquid helium temperatures and found that its electrical resistivity drops suddenly to zero at $T = 4.2$ K. In 1933, Meissner and Ochsenfeld [2] observed that superconductors also exclude magnetic flux and are therefore both perfect conductors and perfect diamagnets. Many common metals and alloys have since been shown to undergo a phase transition to a superconducting state at some low transition temperature, T_c. While increasingly advanced phenomenological theories were developed by Gorter and Casimir [3] (in 1934), London and London [4] (in 1935), and Ginsburg and Landau [5] (in 1950), it was not until 1957, 46 years after the initial discovery, that Bardeen, Cooper, and Schrieffer (BCS) [6] provided a microscopic explanation for superconductivity. The delay can be forgiven, however, as the theory required the invention of quantum mechanics and many-body theory in the intervening years.

The BCS theory does a fantastic job of explaining the behavior of what are now called conventional superconductors, those metals and alloys which become superconducting at relatively low transition temperatures ($T_c < 20$ K). It describes how the ground state energy of a metal can be lowered by taking advantage of phonon-mediated electron-electron interactions to pair up electrons and form Cooper pairs.

Pair-pair correlations imposed by the Pauli exclusion principle then require that Cooper pairs move coherently, marching together in lock-step [7]. The result is a macroscopic quantum ground state in which electrons work collectively to exhibit the behaviors described above. Since electrons are paired, it costs a finite amount of energy, called the energy gap, to break a Cooper pair and form a single particle excitation known as a Bogoliubov quasiparticle, the quantum superposition of an electron and a hole. In conventional superconductors, quasiparticles are exponentially scarce at temperatures small compared to the energy gap. Thus, while their excitation via experimental probe yields interesting results, their small number limits their overall importance [8].

For the 29 years following the work of BCS, superconductivity was, for the most part, a solved problem. That all changed in 1986 when Bednorz and Muller [9] discovered superconductivity in the layered perovskite $(La\text{-}Ba)_2CuO_4$ with $T_c = 33$ K. Over the next few months, T_c was pushed up significantly further with the discovery of similar compounds including $YBa_2Cu_3O_7$ with $T_c = 92$ K. These materials exhibit a crystal structure composed of stacked CuO_2 planes and are therefore known as the cuprates. It was quickly realized that, beyond the high transition temperatures, the cuprate superconductors represented something very new and different. Soon after the initial discovery, Anderson identified three essential features of cuprate superconductivity: (1) the physics is that of the quasi-two-dimensional CuO_2 plane, (2) superconductivity results from doping (adding holes to) a Mott insulator (a material which is insulating due to electron-electron interactions), and (3) the combination of two-dimensionality and proximity to a Mott insulator results in fundamentally new physics [10].

Over the 16 years between then and now, this prediction of new physics has been confirmed. Though the initial excitement regarding technological benefits of high-T_c superconductivity (now as high as 160 K) has since diminished (to some extent), cuprate superconductivity has remained a dominant focus of condensed matter physics. Through a wide range of experiments, the cuprates have been shown to exhibit many strange and fascinating properties including a very abnormal (non-Fermi-liquid) metallic state and a superconducting state that is not well described by conventional BCS theory. In response, a multitude of theories (some more successful than others) have been proposed, debated, and often abandoned. However, while the theoretical community has achieved a (limited) consensus regarding several key issues, the definitive microscopic theory of the cuprates has yet to be established.

In this thesis, we shall not attempt to provide a microscopic theory. Rather, we will concentrate on the superconducting state and study the low temperature properties via a phenomenological approach. The superconducting state in the cuprates, like that in conventional superconductors, is characterized by an order parameter which denotes the energy gap for single particle excitations. However, in contrast to the conventional case where the gap is approximately momentum-independent (of s-wave symmetry), the energy gap in the cuprates is strongly momentum-dependent. Thanks to a series of very clever experiments [11], it is now well established that the gap exhibits d-wave symmetry (as discussed further in the following section). As a result, there are four points on the (2D) Fermi surface (known as gap nodes) at

which the energy gap vanishes. Quasiparticles in the vicinity of these nodal points can therefore be excited at a very low energy cost. Thus, unlike the s-wave case where quasiparticles are exponentially scarce, quasiparticles are prevalent in d-wave superconductors. This means that d-wave quasiparticles are both more important and more easily probed than their s-wave counterparts. Since the excitation of quasiparticles yields a significant reduction of the superfluid density, it contributes to the thermal destruction of superconductivity [12]. Furthermore, present in significant numbers, quasiparticles can be effectively probed via low temperature electrical and thermal transport experiments. From a theoretical point of view, this presents a two-fold opportunity. By studying low temperature quasiparticle transport in d-wave superconductors, we can learn, guided by transport experiments in the cuprates, about the interesting behavior of nodal quasiparticles. In turn, we can apply any knowledge gained toward a better understanding of the superconducting state of the cuprates. These are the goals of our investigation.

1.2 d-Wave Superconductivity

To say that a superconductor is a d-wave superconductor is merely an empirical observation about the symmetry of the order parameter (energy gap), Δ_k. Yet it is an observation that has some very interesting consequences. Consider the diagrams in Fig. 1-1 where we compare the structure of the gap for an s-wave and a d-wave superconductor. For the s-wave case, the gap is constant over the entire Fermi surface, $\Delta_k = \Delta_0$. Thus, there are no quasiparticle states at energies less than the gap. By contrast, for the d-wave case, the gap takes the form

$$\Delta_k = \frac{\Delta_0}{2}\left[\cos(k_x a) - \cos(k_y a)\right] \tag{1.1}$$

where a is the lattice constant. It is clearly momentum-dependent and changes sign from plus to minus to plus to minus as we move along the Fermi surface. Consequently, there exist four points on the Fermi surface, the gap nodes, at which the energy gap vanishes and quasiparticles can be excited at no cost. In the vicinity of a node, the gap varies linearly with the component of momentum parallel to the local Fermi surface, k_2. Similarly, the electron dispersion varies linearly with the momentum component normal to the local Fermi surface, k_1. Hence

$$\epsilon_k \approx v_f k_1 \qquad \Delta_k \approx v_2 k_2 \tag{1.2}$$

where v_f is the Fermi velocity, v_2 is the slope of the gap, and k_1 and k_2 are both measured from the nodal point. The quasiparticle excitation energy therefore takes the form

$$E_k = \sqrt{v_f^2 k_1^2 + v_2^2 k_2^2} \tag{1.3}$$

which describes a cone-shaped dispersion compressed along one axis. In analogy with the cone-shaped dispersion of massless relativistic particles, this is known as an anisotropic Dirac spectrum. In contrast with the s-wave case, these d-wave nodal

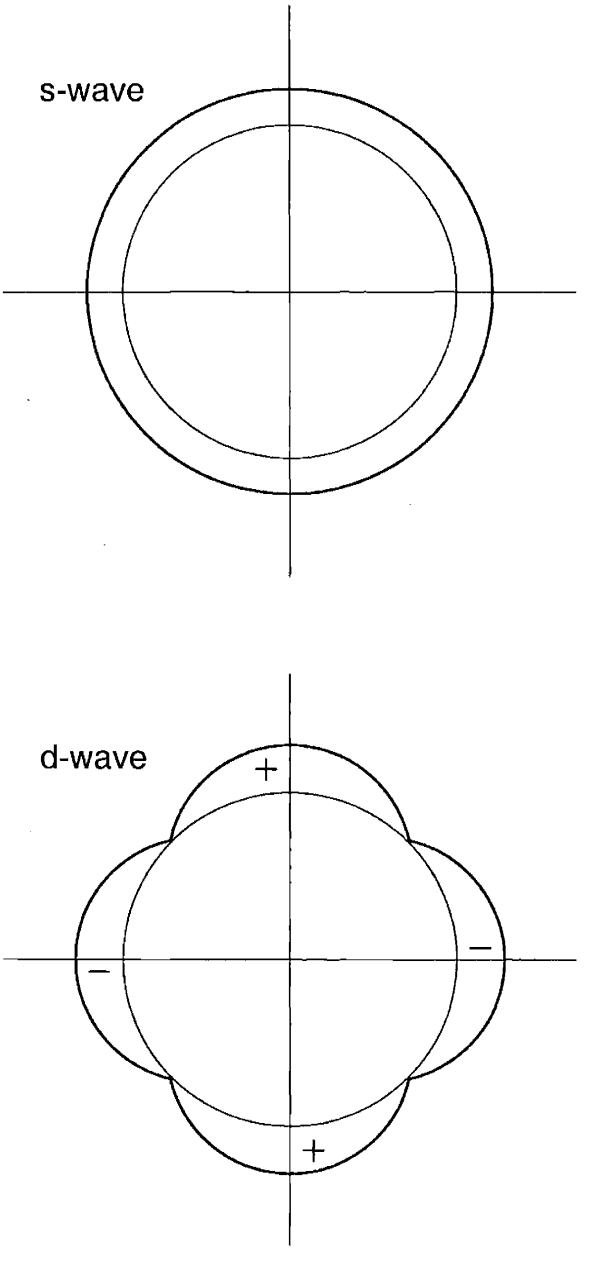

Figure 1-1: Comparison of s-wave and d-wave order parameters.

quasiparticles are very easily excited. The result is a quasiparticle density of states that is linear down to zero energy.

The physics of a nodal quasiparticle in a d-wave superconductor is clearly very different from that of an electron in a metal. In a metal (a Fermi liquid), electrons are governed by the physics of a Fermi surface. The Fermi energy, E_F, provides an inherent energy scale for all calculations. The density of states is nonzero at the Fermi energy and therefore can usually be approximated as a constant in the vicinity of the Fermi surface. By contrast, in a d-wave superconductor, nodal quasiparticles are governed by the physics of a point, the nodal point, rather than a surface. In the vicinity of a node, there is no inherent energy scale. Furthermore, the density of states is far from constant, vanishing linearly at the node and thereby introducing an extra factor of energy into the calculation of many physical quantities. As shall be demonstrated in this thesis, these unusual features inherent in the physics of nodal particles result in quasiparticle transport coefficients that exhibit some very interesting properties.

1.3 Electrical and Thermal Transport

The usual way to probe the low energy excitations of a condensed matter system is to apply a weak perturbation and measure the response. (Or more to the point, give it a gentle kick and see what happens!) Two standard probes are electrical and thermal transport. Electrical transport is probed by applying an electric field, $\mathbf{E}$, and measuring the resulting electrical current density, $\mathbf{j}^e$. Thermal transport is probed by applying a thermal gradient, ∇T, and measuring the resulting heat current density, $\mathbf{j}^Q$. Such measurements yield the electrical and thermal conductivity tensors via

$$j_i^e = \sigma_{ij} E_j \qquad j_i^Q = \kappa_{ij} (-\nabla T)_j \tag{1.4}$$

where $i, j = \{x, y\}$. In order to probe the nodal quasiparticles, and not some other aspect of the system, one must either apply the perturbation in such a way that it is only felt by the quasiparticles or find a way to isolate the quasiparticle response from that of the rest of the system. Over the years, the experimental community has developed and implemented a number of very clever tricks to make this possible. Listed below are some of the experimental techniques that have been used to probe quasiparticle transport in the cuprates. In this thesis, we provide corresponding calculations based on the physics of nodal quasiparticles.

Measuring the electrical transport of nodal quasiparticles is complicated by one tiny detail – the supercurrent! If a DC electric field is applied to the superconductor, the ground state condensate responds (without resistance) and produces a supercurrent. As a result, the DC electrical response of the quasiparticles, while nonzero, is completely shorted out. The solution is to apply an AC electric field. Though the supercurrent only has a DC component, the quasiparticle excitations also respond to nonzero-frequency perturbations. Thus, the quasiparticle response can be measured via microwave experiments. We consider this microwave conductivity in

Chapters 2 and 3.

Thermal transport has the advantage that heat is carried by the quasiparticle excitations but not by the ground state condensate. Unfortunately, heat is also transmitted by vibrations of the crystal lattice. Thus, the thermal conductivity has both an electronic (quasiparticle) contribution and a phononic contribution. The experimentalists can get around this problem in several ways. One way is to consider only very low temperatures where the phonons have been effectively frozen out. The thermal conductivity in this very low temperature limit is considered in Chapter 2. Another way is to apply a perpendicular magnetic field. In the presence of a magnetic field, the quasiparticle contribution to the longitudinal thermal conductivity, κ_{xx}, is field-dependent while the phononic contribution is not. Thus, by fitting the field-dependence to an empirical model, the phononic part can be subtracted out. Furthermore, the magnetic field induces a transverse component, κ_{xy}, which is known as the thermal Hall conductivity. Since the only contribution to κ_{xy} is that of the quasiparticles, it can be measured directly. The nature of this field-dependent thermal conductivity tensor is considered in Chapter 4.

1.4 Review: Conductivity in Simple Metals

In order to introduce some of the concepts that will be important in the body of this thesis, we present here a brief review of the calculation of low temperature conductivity in a simple metal, modeled as a Fermi gas of non-interacting electrons. In a Fermi gas, the ground state electron distribution is that of a sphere in momentum space with energy states occupied up to the Fermi surface. If we apply an electric field, $\mathbf{E}$, the electrons are accelerated, shifting the Fermi sphere in momentum space. The resulting current is limited by the drag induced by impurity scattering, the dominant scattering mechanism at low temperatures. The simplest way to calculate the conductivity is to describe the electron distribution via a quasi-classical distribution function, $f(\mathbf{k})$, and solve the resulting Boltzmann equation [13, 14, 15]. Assuming that the rate of change of the distribution due to scattering is proportional to the deviation from equilibrium, the Boltzmann equation takes the simple form

$$\frac{\partial \mathbf{k}}{\partial t} \cdot \nabla_k f = \left(\frac{df}{dt}\right)_{coll} = -\frac{f(\mathbf{k}) - f_0(\mathbf{k})}{\tau_{tr}} \tag{1.5}$$

where $f_0(\mathbf{k})$ is the equilibrium distribution function and we have introduced the transport scattering rate, $1/\tau_{tr}$. Since the acceleration is equal to the force on the electron due to the electric field, we set $\partial \mathbf{k}/\partial t = -e\mathbf{E}$. For a weak electric field, the deviation of $f(\mathbf{k})$ from equilibrium is small and can be neglected on the left hand side of the Boltzmann equation. We can therefore write $\nabla_k f \approx \nabla_k f_0 = (\mathbf{k}/m)(\partial f_0/\partial \epsilon_k)$, where ϵ_k is the electron dispersion. Solving Eq. (1.5) by inspection we obtain the perturbed distribution function

$$f(\mathbf{k}) = f_0(\mathbf{k}) + \mathbf{k} \cdot \mathbf{E} \frac{e\tau_{tr}}{m} \frac{\partial f_0}{\partial \epsilon_k}. \tag{1.6}$$

The electrical current is then given by $\mathbf{J} = -en\langle \mathbf{v} \rangle$ where n is the electron density and the velocity is averaged over the perturbed distribution function. The resulting momentum integral yields

$$\mathbf{J} = \sigma \mathbf{E} \qquad \sigma = \frac{ne^2 \tau_{tr}}{m} \tag{1.7}$$

which is simply the Drude formula for electrical conductivity. We can find an expression for the transport scattering rate by evaluating the collision term of the Boltzmann equation in terms of the scattering matrix element, $T_{kk'}$, weighted by the occupation probabilities for initial and final states. Noting that impurity scattering is elastic, this yields

$$\frac{f(\mathbf{k}) - f_0(\mathbf{k})}{\tau_{tr}} = 2\pi n_i \int \frac{d^3k'}{(2\pi)^3} \delta(\epsilon_k - \epsilon_{k'}) |T_{kk'}|^2 \left[f(\mathbf{k})(1 - f(\mathbf{k}')) - f(\mathbf{k}')(1 - f(\mathbf{k})) \right] \tag{1.8}$$

where n_i is the density of impurities. Plugging Eq. (1.6) into the above, we obtain

$$\frac{1}{\tau_{tr}} = 2\pi n_i \int \frac{d^3k'}{(2\pi)^3} \delta(\epsilon_k - \epsilon_{k'}) |T_{kk'}|^2 (1 - \cos\theta) \tag{1.9}$$

where θ is the angle between the incident and scattered momentum. Note that this transport scattering rate differs from the relaxation rate (the average time between scattering events)

$$\frac{1}{\tau} = 2\pi n_i \int \frac{d^3k'}{(2\pi)^3} \delta(\epsilon_k - \epsilon_{k'}) |T_{kk'}|^2 \tag{1.10}$$

by a factor of $(1 - \cos\theta)$ within the momentum integral. This factor favors large-angle scattering and accounts for the fact that back scattering is far more effective in degrading a current than forward scattering.

This quasi-classical Boltzmann approach gives a very physical answer but is not easily generalized to more complicated situations, like those considered in the body of this thesis. It is therefore instructive to see how we can reproduce this simple result by using the more complicated, yet more easily generalizable, diagrammatic techniques of many-body theory [13]. This is accomplished by using the Kubo formula to express the temperature and frequency dependent electrical conductivity tensor, $\overleftrightarrow{\sigma}(\Omega, T)$, in terms of the current-current correlation function, $\overleftrightarrow{\Pi}_{ret}(\Omega)$. At nonzero temperatures, we can use the Matsubara formalism to write

$$\overleftrightarrow{\sigma}(\Omega, T) = \frac{\mathrm{Im}\, \overleftrightarrow{\Pi}_{ret}(\Omega)}{\Omega} \qquad \overleftrightarrow{\Pi}_{ret}(\Omega) = \overleftrightarrow{\Pi}(i\Omega \to \Omega + i\delta) \tag{1.11}$$

$$\overleftrightarrow{\Pi}(i\Omega) = -\int_0^\beta d\tau\, e^{i\Omega\tau} \left\langle \mathrm{T}_\tau \mathbf{j}^\dagger(\tau) \mathbf{j}(0) \right\rangle \tag{1.12}$$

where T_τ is a time-ordering operator and $\beta = 1/k_B T$. The simplest way to calculate the current-current correlation function is to approximate it by evaluating the bare-bubble diagram shown in Fig. 1-2(a). Here the electron Green's functions depicted via

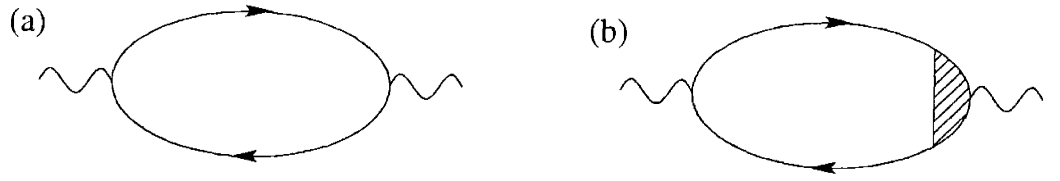

Figure 1-2: (a) Bare polarization bubble. (b) Polarization bubble with dressed vertex.

the upper and lower lines of the bubble are meant to include the contribution of the self-energy due to impurity scattering. However, diagrams depicting impurity scattering contributions that connect the upper and lower Green's functions, the so-called vertex corrections, have been neglected. Within this bare-bubble approximation, the DC conductivity obtained via the Kubo formula is

$$\sigma_{BB} = \frac{ne^2\tau}{m} \tag{1.13}$$

which is of the Drude form but depends on the relaxation rate, $1/\tau$, instead of the transport scattering rate, $1/\tau_{tr}$. The problem is that the bare-bubble approximation violates conservation laws and thereby misses the physical distinction between forward and back scattering. In order to capture this physics, we must include the vertex corrections that were neglected above. Doing so, we evaluate the dressed diagram depicted in the Fig. 1-2(b) and obtain

$$\sigma_{VC} = \frac{ne^2\tau_{tr}}{m} \tag{1.14}$$

which has the correct Drude form. By evaluating vertex corrections to the same order that we evaluate the self-energy, we satisfy conservation laws and recover the important physics encoded by the factor of $(1 - \cos\theta)$ in Eq. (1.9). This effect will be highlighted when we consider an analogous calculation for nodal quasiparticles in the body of this thesis.

At the low temperatures that we have considered above (where impurity scattering is the dominant scattering mechanism), the physics of thermal transport in a metal is entirely analogous to that of electrical transport. Electrons carry both the charge and the heat. Thus, both the electrical current and the heat current are proportional to the Fermi velocity. Hence, as long as neither charge nor energy is exchanged via the scattering (as is the case for elastic impurity scattering), the thermal conductivity is related to the electrical conductivity via the "law" of Wiedemann and Franz

$$\frac{\kappa}{\sigma T} = \frac{\pi^2}{3}\frac{k_B^2}{e^2}. \tag{1.15}$$

By contrast, we shall see that the situation is somewhat different for nodal quasiparticles in a d-wave superconductor.

1.5 Overview

In this thesis, we attempt to provide theoretical interpretations for the results of several low temperature electrical and thermal transport experiments performed on the cuprate superconductors. We do so by considering the scattering of nodal quasiparticles from impurities, line defects, and magnetic vortices and calculating the resulting transport coefficients.

In Chapter 2, we consider quasiparticle transport in the very low temperature limit for which the impurity scattering rate is the dominant energy scale. Due to the node structure of the gap in a d-wave superconductor, the presence of impurities generates additional quasiparticle excitations at low energy. Since these impurity-induced quasiparticles are both generated and scattered by impurities, prior calculations indicate a universal limit ($\Omega \to 0, T \to 0$) where the transport coefficients obtain scattering-independent values, depending only on the velocity anisotropy ratio, v_f/v_2. We improve upon prior results, including the contributions of vertex corrections in our calculations of universal limit electrical, thermal, and spin conductivity. We find that while vertex corrections (and Fermi-liquid corrections) modify the electrical conductivity, the thermal and spin conductivity maintain their universal values, independent of impurity scattering. This conclusion has enabled experimentalists to obtain the anisotropy ratio, v_f/v_2, from low temperature thermal conductivity measurements in the cuprates. (The contents of this chapter result from a collaboration with P. A. Lee and are adapted from a previously published paper [A. C. Durst and P. A. Lee, Phys. Rev. B **62**, 1270 (2000)].)

In Chapter 3, we focus on the microwave electrical conductivity and consider temperatures larger than the scattering rate. Recent microwave conductivity measurements of detwinned, high-purity, slightly overdoped $YBa_2Cu_3O_{6.993}$ crystals reveal a linear temperature dependence and a near-Drude lineshape for temperatures between 1 and 20 K and frequencies ranging from 1 to 75 GHz. Prior theoretical work has shown that simple models of scattering by point defects (impurities) in d-wave superconductors are inconsistent with these results. It has therefore been suggested that scattering by extended defects such as twin boundary remnants, left over from the detwinning process, may also be important. We calculate the self-energy and microwave conductivity in the self-consistent Born approximation (including vertex corrections) for a d-wave superconductor in the presence of scattering from extended linear defects. We find that in the experimentally relevant limit ($\Omega, 1/\tau \ll T \ll \Delta_0$), the resulting microwave conductivity has a linear temperature dependence and a near-Drude frequency dependence that agrees well with experiment. (The contents of this chapter result from a collaboration with P. A. Lee and are adapted from a previously published paper [A. C. Durst and P. A. Lee, Phys. Rev. B **65**, 094501 (2002)].)

In Chapter 4, we turn on a perpendicular magnetic field and consider thermal transport in the mixed state within the weak-field regime. We express the thermal conductivity, κ_{xx}, and the thermal Hall conductivity, κ_{xy}, in terms of the cross section for quasiparticle scattering from a single vortex. Solving for the cross section (neglecting the Berry phase contribution and the anisotropy of the gap nodes), we obtain $\kappa_{xx}(H,T)$ and $\kappa_{xy}(H,T)$ in surprisingly good agreement with the qualitative

features of the experimental results for $YBa_2Cu_3O_{6.99}$. In particular, we show that the simple, yet previously unexpected, weak-field behavior, $\kappa_{xy}(H,T) \sim T\sqrt{H}$, is that of thermally-excited nodal quasiparticles, scattering primarily from impurities, with a small skew component provided by vortex scattering. (The contents of this chapter result from a collaboration with P. A. Lee and A. Vishwanath and are, in part, adapted from a paper that has been submitted for publication [A. C. Durst, A. Vishwanath, and P. A. Lee, cond-mat/0206094].)

Chapter 2

Impurity-Induced Quasiparticle Transport and the Universal Limit

But no perfection is so absolute,
That some impurity doth not pollute.

William Shakespeare

2.1 Introduction

The characteristic feature of a d-wave superconductor is the existence of four nodal points where the order parameter vanishes. Since low energy excitations are concentrated about these nodes, low temperature behavior is dominated by the details of the node structure and, in particular, the ratio of the Fermi velocity to the gap velocity (slope), v_f/v_2. Prior theoretical work has shown that this velocity ratio is prominent in expressions for low temperature transport coefficients [16, 17, 18, 19, 20, 21, 22] as well as the temperature dependence of the superfluid density [12, 23, 24]. However, discrepancies between values of v_f/v_2 obtained from measurements of microwave electrical conductivity [25], thermal conductivity [26, 27], and superfluid density [28], as well as direct measurements of gap structure via ARPES [29] indicate that the existing theoretical predictions must be corrected through a more detailed analysis. To this end, we calculate herein electrical, thermal, and spin conductivity including the contributions of vertex corrections.

It has been shown [30] that for a superconductor with $d_{x^2-y^2}$ pairing symmetry, the presence of impurities enhances the density of quasiparticle states at low energy (although the ultra-low energy regime remains the subject of some debate [31, 32]). This results in a unique situation where an increase in impurity density increases the density of quasiparticles while reducing the quasiparticle lifetime. As a result of the cancellation of these opposing effects, "bare bubble" conductivity calculations (neglecting the corrections we shall consider) indicate a universal limit ($\Omega \to 0, T \to 0$) where the transport coefficients attain constant values, independent of scattering [16]. However, we shall see that these results are modified by corrections to the bare vertex. Vertex corrections account for the fact that forward scattering does not interfere with

the progress of a carrier to the same extent as back scattering. Hence, if the scattering potential varies in k-space such that the potential for forward scattering differs from that for back scattering, the bare bubble transport coefficients may be modified. The purpose of what follows is to improve upon the bare bubble results by including such corrections.

In Sec. 2.2, we define the parameters of our phenomenological d-wave model, introduce the Green's function, and calculate the density of states. In Appendix A (Sec. 2.7), neglecting vertex corrections, we derive a generalized bare bubble polarization function which can be applied to the calculation of either electrical, thermal, or spin conductivity. By treating the general case, we avoid repeating the same basic calculation three times. In Appendix B (Sec. 2.8), we calculate another generalized polarization function, now including the contributions of vertex corrections. The significance of vertex corrections in the universal limit is determined via a numerical calculation presented in Appendix C (Sec. 2.9). In Secs. 2.3, 2.4, and 2.5, we make use of the results in the appendices to calculate electrical, thermal, and spin conductivity in the universal limit ($\Omega \to 0$, $T \to 0$). Each of these sections begins with a derivation of the appropriate current density operator. These calculations reveal an extra gap velocity term in the thermal and spin currents due to the momentum dependence of the d-wave gap and therefore indicate a correction to the standard thermal conductivity formula [33, 34] derived assuming an s-wave gap. Given each current operator, we present the bare bubble result and then note modifications due to vertex corrections. We find that contrary to the scattering-independent result obtained from the bare bubble calculation, the universal limit electrical conductivity attains a vertex correction, which depends explicitly on the nature of the impurity scattering. However, the thermal conductivity and spin conductivity are unaffected by vertex corrections (for small impurity density) and therefore retain their simple, universal values. Conclusions are discussed in Sec. 2.6 where we provide physical descriptions of the mathematical corrections calculated herein.

2.2 d-Wave Model, Green's Function, and Density of States

To study the low temperature transport properties of a d-wave superconductor, we employ a phenomenological model [16, 12] with the Brillouin zone of a two-dimensional square lattice (of lattice constant a), an electron dispersion (via tight binding parametrization)

$$\epsilon_k = -2t_f(\cos k_x a + \cos k_y a) - \mu, \tag{2.1}$$

and an order parameter of $d_{x^2-y^2}$ symmetry

$$\Delta_k = \frac{\Delta_0}{2}(\cos k_x a - \cos k_y a) \tag{2.2}$$

which crosses through zero at each of four nodal points on the Fermi surface, ($k_x = \pm k_y$). The key feature of such a model is that in the vicinity of each of the gap nodes, ϵ_k varies linearly across the Fermi surface and Δ_k varies linearly along the Fermi surface. Defining local momentum variables at each of the nodes with $\hat{\mathbf{k}}_1$ perpendicular to the Fermi surface and $\hat{\mathbf{k}}_2$ parallel to the Fermi surface, we can designate at each node both a Fermi velocity

$$\mathbf{v}_f \equiv \frac{\partial \epsilon_k}{\partial \mathbf{k}} = v_f \hat{\mathbf{k}}_1 \qquad v_f = 2\sqrt{2}\, t_f a \tag{2.3}$$

and a gap velocity

$$\mathbf{v}_2 \equiv \frac{\partial \Delta_k}{\partial \mathbf{k}} = v_2 \hat{\mathbf{k}}_2 \qquad v_2 = \frac{1}{\sqrt{2}} \Delta_0 a. \tag{2.4}$$

(Note that all velocities in our model are taken to be "renormalized" velocities accounting for both band structure and many-body effects within the context of Fermi-liquid theory.) Utilizing these definitions, it becomes clear that the quasiparticle excitation spectrum in the vicinity of each of the gap nodes takes the form of an anisotropic Dirac cone

$$E_k = \sqrt{\epsilon_k^2 + \Delta_k^2} = \sqrt{v_f^2 k_1^2 + v_2^2 k_2^2} \tag{2.5}$$

where the degree of anisotropy is measured by the ratio of the two velocities. This ratio v_f/v_2 appears prominently in the low temperature transport coefficients and is a measurable quantity which provides a convenient means of comparing theory to experiment.

The low temperature physics of such a model is driven by the fact that at the four nodes, there is no gap to quasiparticle excitations. Hence, quasiparticles are generated only in the vicinity of the gap nodes. This is very useful mathematically since it means that a momentum integral over the Brillouin zone can usually be replaced by a sum over nodes and an integral over the small region of k-space surrounding each node. Furthermore, due to the form of the excitation spectrum, Eq. (2.5), it is convenient to scale out the anisotropy of the Dirac cone, and change to polar coordinates in a new scaled momentum $\mathbf{p} = (p, \theta)$. Hence we will frequently make the substitution

$$\sum_k \to \sum_{j=1}^{4} \int \frac{dk_1 dk_2}{(2\pi)^2} \to \sum_{j=1}^{4} \int_0^{p_0} \frac{p\, dp}{2\pi v_f v_2} \int_0^{2\pi} \frac{d\theta}{2\pi} \tag{2.6}$$

where $p_1 = v_f k_1 = p\cos\theta$, $p_2 = v_2 k_2 = p\sin\theta$, $p = \sqrt{p_1^2 + p_2^2} = E_k$, and $p_0 = \sqrt{\pi v_f v_2}/a \sim \mathcal{O}(\Delta_0)$ is a large scaled momentum cutoff defined such that the area of the new integration region is the same as that of the original Brillouin zone. Note that if quasiparticles are only generated at the nodes and the rest of the Brillouin zone makes no contribution, then we should be safe in extending this limit to infinity. However, it is sometimes necessary to retain p_0 through the intermediate stages of a calculation (usually as part of a ratio within a logarithm) maintaining throughout that all other energies are much smaller than this cutoff value.

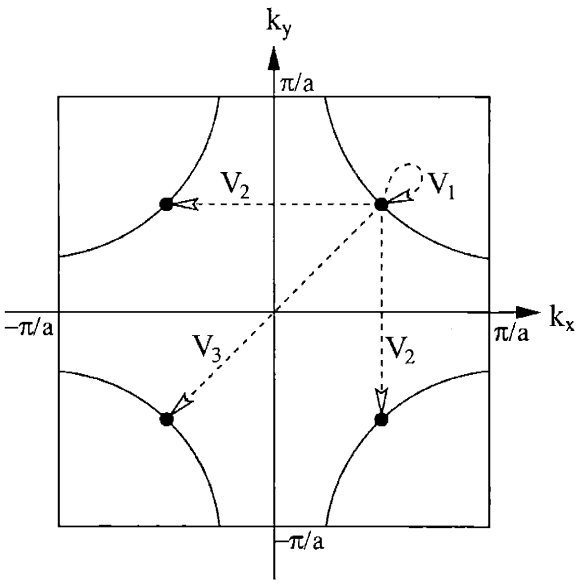

Figure 2-1: Impurity scattering within d-wave model. V_1, V_2, and V_3 are the potentials for intra-node, adjacent-node, and opposite-node scattering.

The fact that quasiparticles are concentrated in the vicinity of the gap nodes is also very useful when considering impurity scattering. Since the initial and final momenta of a scattering event must always be approximately equal to the k-space location of one of the four nodes, a general scattering potential, $V_{kk'}$, need only be evaluated in three possible cases: intra-node scattering ($\mathbf{k}$ and $\mathbf{k}'$ at the same node), adjacent-node scattering ($\mathbf{k}$ and $\mathbf{k}'$ at adjacent nodes), and opposite-node scattering ($\mathbf{k}$ and $\mathbf{k}'$ at opposite nodes). These are depicted graphically in Fig. 2-1 and denoted respectively as V_1, V_2, and V_3. Hence, an arbitrary potential (varying slowly over the area of a node) is effectively reduced to a set of three parameters. This simplification proves quite helpful.

Since the transport calculations in the sections that follow consist of the evaluation of Feynman diagrams via field-theoretic techniques, it is important to establish the types of Green's functions that will be utilized. For any superconductor, the existence of a condensate of ground state pairs means that the annihilation of an electron must be treated on the same footing as the creation of its mate, an electron with opposite momentum and spin. Hence we use the Nambu formalism [7] in which the field operators are two-component spinors of the form

$$\Psi_k = \begin{pmatrix} c_{k\uparrow} \\ c^\dagger_{-k\downarrow} \end{pmatrix} \qquad \Psi^\dagger_k = \left(c^\dagger_{k\uparrow}, c_{-k\downarrow}\right) \tag{2.7}$$

and the resulting Green's functions are 2×2 matrices in *Nambu space*. Since we are concerned with finite temperature calculations, all diagrams will be evaluated using the Matsubara finite temperature formalism [13]. Hence, the bare Matsubara Green's

function expressed in Nambu formalism takes the form

$$\tilde{\mathcal{G}}_0(\mathbf{k}, i\omega) = \frac{1}{(i\omega)^2 - E_k^2} \begin{pmatrix} i\omega + \epsilon_k & \Delta_k \\ \Delta_k & i\omega - \epsilon_k \end{pmatrix} \tag{2.8}$$

where the tilde denotes a Nambu space matrix and $i\omega = i(2n+1)\pi/\beta$ is a fermionic Matsubara frequency. In the presence of impurities, the bare Green's function is dressed via scattering from the impurities and obtains a Matsubara self-energy, $\tilde{\Sigma}(i\omega)$. Assuming that all but the scalar component of the self-energy can be neglected or absorbed into ϵ_k or Δ_k, Dyson's equation yields that the dressed Matsubara Green's function is given by

$$\tilde{\mathcal{G}}(\mathbf{k}, i\omega) = \frac{1}{(i\omega - \Sigma(i\omega))^2 - E_k^2} \begin{pmatrix} i\omega - \Sigma(i\omega) + \epsilon_k & \Delta_k \\ \Delta_k & i\omega - \Sigma(i\omega) - \epsilon_k \end{pmatrix}. \tag{2.9}$$

(Note that while this assumption has been explicitly justified in both the Born and unitary scattering limits, the omitted self-energy components may contribute for intermediate-strength scattering [35, 36]. For simplicity, we neglect such contributions in this investigation.) From the Matsubara functions, corresponding retarded functions are obtained by analytically continuing $i\omega \to \omega + i\delta$ such that

$$\tilde{G}_{ret}(\mathbf{k}, \omega) = \tilde{\mathcal{G}}(\mathbf{k}, i\omega \to \omega + i\delta) \tag{2.10}$$

and the impurity scattering rate is defined as

$$\Gamma(\omega) = -\mathrm{Im}\, \Sigma_{ret}(\omega) \tag{2.11}$$

where $\Sigma_{ret}(\omega) = \Sigma(i\omega \to \omega + i\delta)$.

With the Green's function in hand, it is a simple and illustrative step to calculate the density of states. In terms of the retarded Green's function, the density of states is given by

$$N(\omega) = -\frac{1}{2\pi} \sum_k \mathrm{Tr} \left[\mathrm{Im}\, \tilde{G}_{ret}(\mathbf{k}, \omega) \right]. \tag{2.12}$$

Plugging in the Green's function, Eq. (2.9), replacing the sum by a scaled integral about each node via Eq. (2.6), neglecting the real part of the self-energy, and performing the integration we find that

$$\begin{aligned} N(\omega) &= \frac{2}{\pi^2 v_f v_2} \Gamma(\omega) \left[\ln \frac{p_0}{\Gamma(\omega)} - \ln \sqrt{1 + \frac{\omega^2}{\Gamma(\omega)^2}} \right] \\ &+ \frac{|\omega|}{\pi v_f v_2} \left[\frac{1}{2} - \frac{1}{\pi} \arctan \left(\frac{\Gamma(\omega)^2 - \omega^2}{2|\omega|\Gamma(\omega)} \right) \right]. \end{aligned} \tag{2.13}$$

Note that in the absence of impurities ($\Gamma(\omega) = 0$),

$$N(\omega)\Big|_{\Gamma(\omega)=0} = \frac{|\omega|}{\pi v_f v_2} \tag{2.14}$$

while in the presence of impurities, this simple analysis yields a nonzero density of quasiparticle states down to zero energy [30],

$$N(0) = \frac{2}{\pi^2 v_f v_2} \Gamma_0 \ln \frac{p_0}{\Gamma_0} \tag{2.15}$$

where $\Gamma_0 \equiv \Gamma(\omega \to 0)$. These *impurity-induced* quasiparticles are responsible for the intriguing low temperature transport properties that we shall consider in the sections that follow.

2.3 Microwave Electrical Conductivity

Electrical conductivity can be calculated by means of the Kubo formula [13]

$$\sigma(\Omega, T) = -\frac{\mathrm{Im}\, \Pi_{ret}(\Omega)}{\Omega} \tag{2.16}$$

where $\Pi_{ret}(\Omega) = \Pi(i\Omega \to \Omega + i\delta)$ and $\Pi(i\Omega)$ is the current-current correlation function (or polarization function) in the Matsubara finite temperature formalism:

$$\overleftrightarrow{\Pi}(i\Omega) = -\int_0^\beta d\tau\, e^{i\Omega\tau} \langle T_\tau \mathbf{j}^\dagger(\tau)\mathbf{j}(0)\rangle. \tag{2.17}$$

Thus, our first step is to derive an expression for the electrical current operator. Then by evaluating its correlation function, we obtain the electrical conductivity.

2.3.1 Electrical Current

For a system of interacting electrons, the Hamiltonian is given by

$$H = \int d\mathbf{x} \psi_\alpha^\dagger(\mathbf{x}) \left(\frac{-\nabla^2}{2m^*}\right) \psi_\alpha(\mathbf{x}) + \frac{1}{2} \int d\mathbf{x} d\mathbf{y} \psi_\alpha^\dagger(\mathbf{x}) \psi_\beta^\dagger(\mathbf{y}) V(\mathbf{x}-\mathbf{y}) \psi_\beta(\mathbf{y}) \psi_\alpha(\mathbf{x}) \tag{2.18}$$

where $\psi_\alpha(\mathbf{x})$ annihilates an electron of spin α at position $\mathbf{x}$ and $V(\mathbf{x}-\mathbf{y})$ is the electron-electron interaction potential. In the presence of a vector potential $\mathbf{A}(\mathbf{x})$, the Hamiltonian must be invariant under a local gauge transformation. While the second term is gauge invariant as written, the first must be modified by making the standard replacement $-i\nabla \to -i\nabla + e\mathbf{A}$. Thus, the Hamiltonian becomes a functional of the vector potential and takes the form

$$H[\mathbf{A}(\mathbf{x})] = \int d\mathbf{x} \psi_\alpha^\dagger(\mathbf{x}) \left(\frac{(-i\nabla + e\mathbf{A})^2}{2m^*}\right) \psi_\alpha(\mathbf{x})$$

$$+ \quad \frac{1}{2}\int dx dy \psi^\dagger_\alpha(\mathbf{x})\psi^\dagger_\beta(\mathbf{y})V(\mathbf{x}-\mathbf{y})\psi_\beta(\mathbf{y})\psi_\alpha(\mathbf{x}). \tag{2.19}$$

Note that only the kinetic term couples to the vector potential. Taking the functional derivative with respect to $\mathbf{A}(\mathbf{x})$ we obtain an expression for the electrical current:

$$\mathbf{j}^e(\mathbf{x}) = -\mathrm{Re}\frac{\delta H}{\delta \mathbf{A}(\mathbf{x})} = \frac{-e}{2im^*}\left(\psi^\dagger_\alpha \nabla\psi_\alpha - \nabla\psi^\dagger_\alpha\psi_\alpha\right). \tag{2.20}$$

Then taking the space-time Fourier transform yields

$$\mathbf{j}^e(\mathbf{q},\Omega) = -\frac{e}{m^*}\sum_{k,\omega}\left(\mathbf{k}+\frac{\mathbf{q}}{2}\right)c^\dagger_{k\alpha}c_{k+q\alpha} \tag{2.21}$$

and in the limit that $\mathbf{q}\to 0$ we obtain

$$\mathbf{j}^e(0,\Omega) = -e\sum_{k,\omega}\mathbf{v}_f\Psi^\dagger_k\tilde{\mathbb{1}}\Psi_{k+q} \tag{2.22}$$

where $\mathbf{v}_f \equiv \partial\epsilon_k/\partial\mathbf{k} = \mathbf{k}/m^*$ and we have expressed the final result in terms of 2×2 Nambu matrix notation. Note that in all cases, momentum indices on field operators denote both momentum and frequency. Although this result is well known, we have derived it here in order to provide a basis for comparison with the thermal current and spin current to be derived later.

2.3.2 Bare Bubble (Electrical)

Given the current, we proceed to calculate the corresponding current-current correlation function. The correlation function for the electrical current can be expressed diagrammatically as a fermionic bubble with fully dressed propagators and a fully dressed vertex in which each vertex contributes a coupling parameter e, a velocity $\mathbf{v}_f$, and a 2×2 Nambu unit matrix $\tilde{\mathbb{1}}$. Assuming that the impurity scattering potential is isotropic in k-space, the corrections to the bare vertex vanish. Thus, in this approximation, the conductivity can be obtained from the calculation of a bubble with dressed propagators (i.e. Green's functions with self-energy included) but bare vertices (no interaction between the two propagators). Such a diagram will be referred to as a *bare bubble.*

The calculation of the bare bubble polarization function is of the same basic form for the electrical, thermal, and spin conductivities. Thus, to avoid repeating the same derivation several times, a generalized polarization function $\Pi^{g\ell\alpha}_{rct}(\Omega)$ (applicable to all three cases) which depends on a coupling parameter g, a velocity $\mathbf{v}_\ell$, and a Nambu matrix $\tilde{\tau}_\alpha$ has been calculated in Sec. 2.7. Applying the general result, Eq. (2.111), to the case of interest ($g=e$, $\mathbf{v}_\ell = \mathbf{v}_f$, $\tilde{\tau}_\alpha = \tilde{\mathbb{1}}$) we find that

$$\sigma(\Omega,T) = \frac{e^2}{\pi^2}\frac{v_f}{v_2}\int\frac{d^2p}{2\pi}\int_{-\infty}^{\infty}d\omega\frac{n_F(\omega)-n_F(\omega+\Omega)}{\Omega}\mathrm{Tr}\left[\tilde{G}''_{ret}(\mathbf{p},\omega)\tilde{G}''_{ret}(\mathbf{p},\omega+\Omega)\right] \tag{2.23}$$

where

$$\tilde{G}_{ret}(\mathbf{p},\omega) = \frac{1}{(\omega - \Sigma_{ret}(\omega))^2 - p^2} \begin{pmatrix} \omega - \Sigma_{ret}(\omega) + p_1 & p_2 \\ p_2 & \omega - \Sigma_{ret}(\omega) - p_1 \end{pmatrix}. \quad (2.24)$$

In the universal limit ($\Omega \to 0$, $T \to 0$),

$$\frac{n_F(\omega) - n_F(\omega + \Omega)}{\Omega} \to -\frac{\partial n_F}{\partial \omega} \to \delta(\omega). \quad (2.25)$$

Hence, evaluating the rest of the integrand for $\omega \to 0$, noting that $\Sigma_{ret}(0) = -i\Gamma_0$, and integrating over momentum, we obtain the universal limit bare bubble electrical conductivity:

$$\sigma_0 = \frac{e^2}{\pi^2}\frac{v_f}{v_2}. \quad (2.26)$$

This is the universal conductivity obtained in Ref. [16]. Finite temperature corrections can be obtained via a Sommerfeld expansion (for $T \ll \Gamma(\omega)$) and have been calculated by Hirschfeld *et al.* [18] and Graf *et al.* [20].

2.3.3 Vertex Corrections (Electrical)

The bare bubble conductivity derived above was calculated in the approximation that vertex corrections could be safely neglected. It turns out (as we shall see later) that this approximation is justified if the impurity scattering potential is isotropic in k-space ($V_{kk'} = V = \text{const}$). However, for a general scattering potential, corrections to the bare vertex can make a significant contribution and must be included in the calculation. To this end, we shall consider the contribution of the *ladder corrections* to the bare vertex (see Fig. 2-4 of Sec. 2.8). Once again, since the electrical calculation is of the same form as that for the thermal and spin conductivity, a generalized polarization function including vertex corrections (which can be applied to all three cases) has been calculated in Sec. 2.8. For the electrical conductivity, the polarization function consists of a single bubble (with a dressed vertex) where each vertex contributes a coupling parameter e, a velocity $\mathbf{v}_f$, and a Nambu matrix $\tilde{\mathbb{1}}$. Plugging these parameters into the generalized polarization function, Eq. (2.160), and using the electrical Kubo formula, Eq. (2.16), we find that

$$\sigma(\Omega,T) = \frac{e^2}{2\pi^2}\frac{v_f}{v_2}\int_{-\infty}^{\infty} d\omega\, \frac{n_F(\omega) - n_F(\omega+\Omega)}{\Omega} \mathrm{Re}\left[J_2^{(0)}(\omega,\Omega) - J_1^{(0)}(\omega,\Omega)\right] \quad (2.27)$$

where J_1^{α} and J_2^{α} are defined in Sec. 2.8. In the universal limit ($\Omega \to 0$, $T \to 0$), we can make use of Eq. (2.25) to find that

$$\sigma_0 = \frac{e^2}{2\pi^2}\frac{v_f}{v_2}\mathrm{Re}\left[\frac{I_2^{(0)}}{1 - \gamma_{A2}^{(0)} I_2^{(0)}\left(1 + \frac{\gamma_{B2}^{(0)}}{\gamma_{A2}^{(0)}}\frac{\gamma_{B2}^{(0)} I_2^{(1)}}{1 - \gamma_{A2}^{(0)} I_2^{(1)}}\right)} - \frac{I_1^{(0)}}{1 - \gamma_{A1}^{(0)} I_1^{(0)}\left(1 + \frac{\gamma_{B1}^{(0)}}{\gamma_{A1}^{(0)}}\frac{\gamma_{B1}^{(0)} I_1^{(1)}}{1 - \gamma_{A1}^{(0)} I_1^{(1)}}\right)}\right] \quad (2.28)$$

where all functions are evaluated for $\Omega, \omega \to 0$. In these limits, the constituent functions defined in Sec. 2.8 take the form:

$$F'(0) = \frac{F(i\Gamma_0)}{4\pi v_f v_2} = i\frac{\Gamma_0}{2\pi v_f v_2}\ln\frac{p_0}{\Gamma_0} = i\frac{\pi}{4}N(0) \tag{2.29}$$

$$T_n^a(0) = \left(\frac{\underline{V}}{1+(\frac{\pi}{4}N(0))^2\underline{V}^2}\right)_{n1} \equiv A_n \tag{2.30}$$

$$T_n^b(0) = i\left(\frac{-\frac{\pi}{4}N(0)\underline{V}^2}{1+(\frac{\pi}{4}N(0))^2\underline{V}^2}\right)_{n1} \equiv iB_n \tag{2.31}$$

$$\begin{aligned}
\gamma_{A1}^{(0)} &= \frac{n_i}{4\pi v_f v_2}\left(A_n^2 - B_n^2\right)\left[|_{n=1} - |_{n=3}\right] \\
\gamma_{A2}^{(0)} &= \frac{n_i}{4\pi v_f v_2}\left(A_n^2 + B_n^2\right)\left[|_{n=1} - |_{n=3}\right] \\
\gamma_{B1}^{(0)} &= i\frac{n_i}{2\pi v_f v_2}A_n B_n\left[|_{n=1} - |_{n=3}\right] \\
\gamma_{B2}^{(0)} &= 0
\end{aligned} \tag{2.32}$$

$$I_1^{(0)}(0,0) = \left.\frac{dF(z)}{dz}\right|_{i\Gamma_0} = 2\ln\frac{p_0}{\Gamma_0} - 2 \tag{2.33}$$

$$I_2^{(0)}(0,0) = \frac{\mathrm{Im}\,F(i\Gamma_0)}{\Gamma_0} = 2\ln\frac{p_0}{\Gamma_0} \tag{2.34}$$

$$I_1^{(1)}(0,0) = \frac{1}{2}\left(\left.\frac{dF(z)}{dz}\right|_{i\Gamma_0} - \frac{F(i\Gamma_0)}{i\Gamma_0}\right) = -1 \tag{2.35}$$

$$I_2^{(1)}(0,0) = \lim_{\omega\to 0}\frac{\mathrm{Im}\left[(\omega - i\Gamma_0)F(\omega + i\Gamma_0)\right]}{2\Gamma_0\omega} = 1 \tag{2.36}$$

Thus, including vertex corrections, the universal limit electrical conductivity takes the form

$$\sigma_0 = \frac{e^2}{\pi^2}\frac{v_f}{v_2}\beta_{vc} \tag{2.37}$$

$$\beta_{vc} = \frac{1 + 2\left(\gamma_{A2}^{(0)} - \gamma_{A1}^{(0)} + \frac{\gamma_{B1}^{(0)\,2}}{1-\gamma_{A1}^{(0)}}\right)\ln\frac{p_0}{\Gamma_0}\left(\ln\frac{p_0}{\Gamma_0} - 1\right)}{\left(1 - 2\gamma_{A2}^{(0)}\ln\frac{p_0}{\Gamma_0}\right)\left(1 - 2\left(\gamma_{A1}^{(0)} - \frac{\gamma_{B1}^{(0)\,2}}{1-\gamma_{A1}^{(0)}}\right)\left(\ln\frac{p_0}{\Gamma_0} - 1\right)\right)} \tag{2.38}$$

where β_{vc} is the scattering dependent vertex correction to the universal bare bubble result. Note that since the γ's all depend on the difference between the intra-node T-matrix (n=1) and the opposite-node T-matrix (n=3), $\beta_{vc} \to 1$ if the two scattering potentials are the same. Hence for an isotropic scattering potential, the bare bubble result, Eq. (2.26), is recovered. However, in general we presume that the scattering potential will fall off for large $\mathbf{k}$ and the potential for intra-node scattering will be

larger than that for opposite-node scattering. If so, the γ's will be nonzero and the universal limit conductivity will deviate from its bare bubble value. This correction to the conductivity due to differences between intra-node (forward) scattering and opposite-node (back) scattering is the node-discrete equivalent of the famous $(1 - \cos\theta)$ factor obtained from vertex corrections in the conductivity calculation for a simple metal. As in the metallic case, the phenomenon at work is the fact that forward and back scattering can have different effects on the progress of a charge carrier. As a result, anisotropy in the scattering potential can renormalize the conductivity.

In general, the evaluation of β_{vc} requires a numerical calculation since Γ_0 must be obtained self-consistently as a function of impurity density and scattering potential. Such calculations (presented in Sec. 2.9) indicate that for anisotropic scattering, the electrical vertex correction can be significant even to zeroth order in the impurity density.

For the case of Born scattering, β_{vc} reduces to a more simple and illustrative form. In the Born limit (small V),

$$T_n^a(0) = V_{n1} \qquad T_n^b(0) = 0 \tag{2.39}$$

$$\gamma_{A1}^{(0)} = \gamma_{A2}^{(0)} = \frac{n_i}{4\pi v_f v_2}(V_1^2 - V_3^2) \qquad \gamma_{B1}^{(0)} = 0 \tag{2.40}$$

and the zero-frequency scattering rate takes the form

$$\Gamma_0 = p_0 \exp\left(-\frac{2\pi v_f v_2}{n_i(V_1^2 + 2V_2^2 + V_3^2)}\right) = \frac{\pi}{4} n_i (V_1^2 + 2V_2^2 + V_3^2) N(0) \tag{2.41}$$

where (as defined in Sec. 2.2) V_1, V_2, and V_3 correspond respectively to intra-node, adjacent-node, and opposite-node scattering. Noting that $\ln \frac{p_0}{\Gamma_0} \sim \frac{1}{n_i} \gg 1$ and defining

$$\Gamma_1 \equiv 2\gamma_{A1}^{(0)} \Gamma_0 \ln \frac{p_0}{\Gamma_0} = \frac{\pi}{4} n_i (V_1^2 - V_3^2) N(0) \tag{2.42}$$

and a transport scattering rate

$$\Gamma_{tr} \equiv \Gamma_0 - \Gamma_1 = \frac{\pi}{4} n_i (2V_2^2 + 2V_3^2) N(0) \tag{2.43}$$

the vertex correction factor, Eq. (2.38), reduces to

$$\beta_{vc} = \left(\frac{\Gamma_0}{\Gamma_{tr}}\right)^2 = \left(\frac{V_1^2 + 2V_2^2 + V_3^2}{2V_2^2 + 2V_3^2}\right)^2. \tag{2.44}$$

Note that the vertex correction depends on the scattering potential but is independent of the density of impurities. In this simple limit it is clear that if intra-node scattering is stronger than opposite-node scattering (as we expect), Γ_0 will exceed Γ_{tr} and the universal limit electrical conductivity will be enhanced beyond the bare bubble result.

2.3.4 Superfluid Density

As a check on the accuracy of our conductivity calculations, it is useful to make a brief digression and use our results to calculate an experimentally distinct quantity, the superfluid density (in the clean limit), $\rho^s(T)$. By definition (see Ref. [12]),

$$\rho^s(T) \equiv \rho^s(T=0) - \rho^n(T) \tag{2.45}$$

where $\rho^n(T)$ is the normal fluid density. Hence, to obtain the temperature dependence of the superfluid density, it suffices to calculate the normal fluid density. While the conductivity is related to the imaginary part of the polarization function, the normal fluid density is proportional to the real part via

$$\frac{\rho^n(T)}{m} = -\frac{\mathrm{Re}\,\Pi_{ret}(\Omega=0)}{e^2}. \tag{2.46}$$

Obtaining Π_{ret} from the generalized result, Eq. (2.159) in Sec. 2.8, setting $\Omega = 0$, taking the no impurities limit ($\Gamma(\omega) \to 0$), and plugging into Eq. (2.46) we find that

$$\frac{\rho^n(T)}{m} = \frac{1}{\pi^2}\frac{v_f}{v_2}\int_{-\infty}^{\infty} d\omega\; n_F(\omega)\;\mathrm{Im}\left[I_1^{(0)}(\omega,0)\right] \tag{2.47}$$

where

$$\mathrm{Im}\left[I_1^{(0)}(\omega,0)\right] = \pi\mathrm{sgn}(\omega)\left[\theta(\omega+p_0)-\theta(\omega-p_0)\right] + \pi p_0\left[\delta(\omega+p_0)-\delta(\omega-p_0)\right]. \tag{2.48}$$

Performing the frequency integration yields that the superfluid density is given by

$$\frac{\rho^s(T)}{m} = \frac{\rho^s(0)}{m} - \frac{2\ln 2}{\pi}\frac{v_f}{v_2}k_B T \tag{2.49}$$

which is precisely the result obtained in Ref. [12] through an entirely different procedure.

2.3.5 Fermi-liquid Corrections

We note, however, that the superfluid density calculated in the preceding section (and in Ref. [12]) is not quite correct. As pointed out by Millis *et al.* [23], we have neglected to include the effect of interactions between the electrons that underlie the superconducting state. Treating the superconducting state as a superfluid Fermi-liquid [37, 38, 39], we refer to such interactions as Fermi-liquid interactions. (Note that while the normal state of the cuprates is not a Fermi-liquid, the superconducting state has well defined quasiparticle excitations and is therefore appropriately described via Fermi-liquid theory. This is the point of view taken in Refs. [12] and [23].) In the presence of Fermi-liquid interactions, electrons (really Landau quasiparticles) excited by a perturbation cannot simply respond as if they were free. Rather, any electron current induced by the perturbation is accompanied by a drag current re-

sulting from the Fermi-liquid interactions with all the other perturbed electrons [40]. In the superconducting state, this means that the (Bogoliubov) quasiparticle current is renormalized due to the drag of other perturbed quasiparticles as well as the condensate itself (providing it is also perturbed by the perturbation). Since the quasiparticle density is small at low temperatures, this effect is only significant if there is a supercurrent that can contribute to the drag.

Now consider the case of an electrical perturbation, that is, an applied electric or magnetic field that induces an electrical current. Since the condensate will respond to such a perturbation (via a supercurrent), Fermi-liquid interactions will cause a perturbed quasiparticle to drag the condensate along with it. The electrical current is therefore renormalized such that

$$\mathrm{j}^e \to \mathrm{j}^e \alpha_{fl} \tag{2.50}$$

where α_{fl} is a phenomenological constant. (Note that for a circular Fermi surface, $\alpha_{fl} = 1 + F_1^s/2$ where F_1^s is the $\ell = 1$ spin-symmetric Landau parameter.) Since the normal fluid density is given by the real part of the electrical current-current correlation function via Eq. (2.46), it acquires two factors of α_{fl}. Thus, including the effect of Fermi-liquid interactions, the superfluid density should be expressed as

$$\frac{\rho^s(T)}{m} = \frac{\rho^s(0)}{m} - \frac{2\ln 2}{\pi}\frac{v_f}{v_2}\alpha_{fl}^2 k_B T \tag{2.51}$$

which is the result that was obtained by Millis *et al.* [23].

Since the universal-limit electrical conductivity is given by the imaginary part of the same electrical current-current correlation function, it should also be renormalized by two factors of α_{fl}. Modifying Eq. (2.37) to reflect this renormalization, our expression becomes

$$\sigma_0 = \frac{e^2}{\pi^2}\frac{v_f}{v_2}\beta_{vc}\alpha_{fl}^2. \tag{2.52}$$

Note that since a thermal gradient or a Zeeman field will not induce a supercurrent, the heat current and the spin current are not significantly affected by Fermi-liquid interactions. Thus, in contrast to the electrical case, the thermal conductivity and the spin conductivity do not acquire a Fermi-liquid renormalization.

2.4 Thermal Conductivity

Analogous to the case of electrical conductivity, thermal conductivity can be calculated by means of a thermal Kubo formula [13]:

$$\frac{\kappa(\Omega, T)}{T} = -\frac{1}{T^2}\frac{\mathrm{Im}\,\Pi^\kappa_{ret}(\Omega)}{\Omega} \tag{2.53}$$

where $\Pi^\kappa_{ret}(\Omega) = \Pi^\kappa(i\Omega \to \Omega + i\delta)$ and $\Pi^\kappa(i\Omega)$ is the finite temperature current-current correlation function (or polarization function). In this case, the appropriate

current for the correlation function is the thermal current derived below.

2.4.1 Thermal Current

To derive an expression for the heat current in an anisotropic superconductor, we can follow the s-wave derivation of Ambegaokar and Griffin [33] and generalize to the case of an anisotropic gap. As in Eq. (2.18), the Hamiltonian takes the form

$$H = \int d\mathbf{x}\psi_\alpha^\dagger(\mathbf{x})\left(\frac{-\nabla^2}{2m^*}\right)\psi_\alpha(\mathbf{x}) + \frac{1}{2}\int d\mathbf{x}d\mathbf{y}\psi_\alpha^\dagger(\mathbf{x})\psi_\beta^\dagger(\mathbf{y})V(\mathbf{x}-\mathbf{y})\psi_\beta(\mathbf{y})\psi_\alpha(\mathbf{x}). \quad (2.54)$$

Given the Hamiltonian, it is straightforward to obtain the equations of motion for the field operators

$$i\dot{\psi}_\alpha = [\psi_\alpha, H] = \left(\frac{-\nabla^2}{2m^*} + \int d\mathbf{r}V(\mathbf{x}-\mathbf{r})\psi_\gamma^\dagger(\mathbf{r})\psi_\gamma(\mathbf{r})\right)\psi_\alpha \quad (2.55)$$

and to define a Hamiltonian density

$$h(\mathbf{x}) = \frac{1}{2m^*}\nabla\psi_\alpha^\dagger(\mathbf{x})\cdot\nabla\psi_\alpha(\mathbf{x}) + \frac{1}{2}\int d\mathbf{y}V(\mathbf{x}-\mathbf{y})\psi_\alpha^\dagger(\mathbf{x})\psi_\beta^\dagger(\mathbf{y})\psi_\beta(\mathbf{y})\psi_\alpha(\mathbf{x}). \quad (2.56)$$

If all energies are measured with respect to the chemical potential, this Hamiltonian density is the heat density. Hence, the operator $\mathbf{j}^Q(\mathbf{x})$ that satisfies the continuity equation

$$\dot{h}(\mathbf{x}) + \nabla\cdot\mathbf{j}^Q(\mathbf{x}) = 0 \quad (2.57)$$

can be interpreted as the heat current. Taking the time derivative of Eq. (2.56) and using the equations of motion, Eq. (2.55), we find that

$$\begin{aligned}\dot{h} &= \nabla\cdot(\dot{\psi}_{x\alpha}^\dagger\nabla\psi_{x\alpha} + \nabla\psi_{x\alpha}^\dagger\dot{\psi}_{x\alpha}) - \frac{1}{2}\int d\mathbf{y}V(\mathbf{y}-\mathbf{x}) \\ &\times \left[(\dot{\psi}_{x\alpha}^\dagger\psi_{y\beta}^\dagger\psi_{y\beta}\psi_{x\alpha} + \psi_{x\alpha}^\dagger\psi_{y\beta}^\dagger\psi_{y\beta}\dot{\psi}_{x\alpha}) - (\psi_{x\alpha}^\dagger\dot{\psi}_{y\beta}^\dagger\psi_{y\beta}\psi_{x\alpha} + \psi_{x\alpha}^\dagger\psi_{y\beta}^\dagger\dot{\psi}_{y\beta}\psi_{x\alpha})\right]\end{aligned} \quad (2.58)$$

where the compact notation $\psi_{x\alpha} \equiv \psi_\alpha(\mathbf{x})$ has been used for the sake of brevity. Defining $\mathbf{j}^Q = \mathbf{j}_1^Q + \mathbf{j}_2^Q$ we can use Eq. (2.57) to write

$$\mathbf{j}_1^Q(\mathbf{x}) = -\frac{1}{2m^*}\left(\dot{\psi}_{x\alpha}^\dagger\nabla\psi_{x\alpha} + \nabla\psi_{x\alpha}^\dagger\dot{\psi}_{x\alpha}\right) \quad (2.59)$$

and

$$\begin{aligned}\nabla\cdot\mathbf{j}_2^Q(\mathbf{x}) &= \frac{1}{2}\int d\mathbf{y}V(\mathbf{y}-\mathbf{x}) \\ &\times \left[(\dot{\psi}_{x\alpha}^\dagger\psi_{y\beta}^\dagger\psi_{y\beta}\psi_{x\alpha} + \psi_{x\alpha}^\dagger\psi_{y\beta}^\dagger\psi_{y\beta}\dot{\psi}_{x\alpha}) - (\psi_{x\alpha}^\dagger\dot{\psi}_{y\beta}^\dagger\psi_{y\beta}\psi_{x\alpha} + \psi_{x\alpha}^\dagger\psi_{y\beta}^\dagger\dot{\psi}_{y\beta}\psi_{x\alpha})\right].\end{aligned} \quad (2.60)$$

Taking the space-time Fourier transform of Eq. (2.59) in the limit that $\mathbf{q} \to 0$ we obtain

$$\mathbf{j}_1^Q(0,\Omega) = \sum_{k,\omega} \left(\omega + \frac{\Omega}{2}\right) \mathbf{v}_f c_{k\alpha}^\dagger c_{k+q\alpha} = \sum_{k,\omega} \left(\omega + \frac{\Omega}{2}\right) \mathbf{v}_f \Psi_k^\dagger \tilde{\tau}_3 \Psi_{k+q} \tag{2.61}$$

where $\mathbf{v}_f \equiv \partial\epsilon_k/\partial\mathbf{k} = \mathbf{k}/m^*$, $c_{k\alpha}$ is the space-time Fourier transform of $\psi_\alpha(\mathbf{x})$, and the second equality is written in terms of the 2×2 Nambu matrix notation introduced in Sec. 2.2. Please note that in our compact notation, momentum indices on field operators always represent both momentum and frequency (i. e. $\Psi_k \equiv \Psi(\mathbf{k},\omega)$ and $\Psi_{k+q} \equiv \Psi(\mathbf{k}+\mathbf{q},\omega+\Omega)$).

Similarly, taking the space-time Fourier transform of Eq. (2.60) generates four terms such that

$$i\mathbf{q}\cdot\mathbf{j}_2^Q(\mathbf{q},\Omega) = X_1 + X_2 - Y_1 - Y_2. \tag{2.62}$$

The first such term, X_1 , is given by

$$X_1 = \sum_{k's,\omega's} \omega_1 V_{k_5} c_{k_1\alpha}^\dagger c_{k_2\beta}^\dagger c_{k_3\beta} c_{k_4\alpha}\, \delta_{k_4-k_1-k_5-q}\delta_{k_3-k_2+k_5}\delta_{\omega_1+\omega_2-\omega_3-\omega_4+\Omega}. \tag{2.63}$$

Taking the mean field approximation, retaining only the terms for which the average values are over $(\mathbf{k}\uparrow, -\mathbf{k}\downarrow)$ pairs, and using the fact that $\langle c_{k\uparrow}^\dagger c_{-k\downarrow}^\dagger\rangle$ is an even function of ω , this becomes

$$X_1 = -i\sum_{k,\omega}(\omega-\Omega)\Delta_k^\dagger c_{k-q\uparrow}^\dagger c_{-k\downarrow}^\dagger \tag{2.64}$$

where

$$\Delta_k \equiv -\sum_{k',\omega'} V_{k-k'} \left\langle c_{k\uparrow}^\dagger c_{-k\downarrow}^\dagger \right\rangle. \tag{2.65}$$

Repeating this procedure for X_2 , Y_1 , and Y_2 and taking Δ_k to be real we find that

$$\mathbf{q}\cdot\mathbf{j}_2^Q(\mathbf{q},\Omega) = -\sum_{k,\omega}(\Delta_{k+q}-\Delta_k)\left[\omega c_{k\uparrow}^\dagger c_{-(k+q)\downarrow}^\dagger + (\omega+\Omega)c_{-k\downarrow}c_{k+q\uparrow}\right]. \tag{2.66}$$

In the limit as $\mathbf{q}\to 0$

$$\Delta_{k+q} - \Delta_k \approx \mathbf{q}\cdot\frac{\partial\Delta_k}{\partial\mathbf{k}} \equiv \mathbf{q}\cdot\mathbf{v}_2. \tag{2.67}$$

Thus, casting Eq. (2.66) in terms of the Nambu matrix formalism we find that

$$\mathbf{j}_2^Q(0,\Omega) = -\sum_{k,\omega}\left[\left(\omega+\frac{\Omega}{2}\right)\mathbf{v}_2\Psi_k^\dagger\tilde{\tau}_1\Psi_{k+q} + \frac{\Omega}{2i}\mathbf{v}_2\Psi_k^\dagger\tilde{\tau}_2\Psi_{k+q}\right]. \tag{2.68}$$

In the limit of small Ω, the second term can be neglected compared to the first. Thus, combining Eq. (2.68) with Eq. (2.61) we obtain the following expression for the heat current in an anisotropic superconductor:

$$\mathbf{j}^Q(0,\Omega) = \sum_{k,\omega}\left(\omega+\frac{\Omega}{2}\right)\left[\mathbf{v}_f\Psi_k^\dagger\tilde{\tau}_3\Psi_{k+q} - \mathbf{v}_2\Psi_k^\dagger\tilde{\tau}_1\Psi_{k+q}\right]. \tag{2.69}$$

Note that for an s-wave superconductor, the gap is independent of $\mathbf{k}$ and $\mathbf{v}_2 = 0$. Thus, the second term in the heat current vanishes and Eq. (2.69) reduces to the result derived by Ambegaokar *et al.* [33, 34]. However, for a d-wave superconductor, the gap is anisotropic and $\mathbf{v}_2 \neq 0$. Hence, although the gap term may be small, neither term can be formally neglected.

2.4.2 Bare Bubble (Thermal)

Unlike the electrical current, the thermal current has two terms: a "Fermi" term proportional to $\mathbf{v}_f$ and $\tilde{\tau}_3$ and a "gap" term proportional to $\mathbf{v}_2$ and $\tilde{\tau}_1$. Therefore, when we evaluate the current-current correlation function, we expect four bubbles rather than just one: Fermi-Fermi, Fermi-gap, gap-Fermi, and gap-gap. However, since the Fermi velocity $\mathbf{v}_f$ and the gap velocity $\mathbf{v}_2$ are orthogonal at each of the gap nodes, the two cross terms cancel. Hence, the thermal conductivity has two terms: a Fermi term with velocity $\mathbf{v}_f$ and Nambu matrix $\tilde{\tau}_3$ on each vertex and a gap term with velocity $\mathbf{v}_2$ and Nambu matrix $\tilde{\tau}_1$ on each vertex. For both terms the coupling parameter is $(\omega + \Omega/2)$.

Neglecting vertex corrections, each term can be obtained from the bare bubble generalized polarization function derived in Sec. 2.7. Plugging the appropriate parameters into the general result, Eq. (2.111), we find that

$$\frac{\kappa(\Omega,T)}{T} = \frac{1}{\pi^2 v_f v_2}\int\frac{d^2p}{2\pi}\int_{-\infty}^{\infty}\frac{d\omega}{\Omega}\frac{n_F(\omega)-n_F(\omega+\Omega)}{\Omega}\left(\frac{\omega+\frac{\Omega}{2}}{T}\right)^2$$
$$\times\left[v_f^2\mathrm{Tr}\left[\tilde{G}''_{ret}(\mathbf{p},\omega)\tilde{\tau}_3\tilde{G}''_{ret}(\mathbf{p},\omega+\Omega)\tilde{\tau}_3\right]+v_2^2\mathrm{Tr}\left[\tilde{G}''_{ret}(\mathbf{p},\omega)\tilde{\tau}_1\tilde{G}''_{ret}(\mathbf{p},\omega+\Omega)\tilde{\tau}_1\right]\right] \tag{2.70}$$

In the universal limit ($\Omega \to 0$, $T \to 0$),

$$\frac{n_F(\omega)-n_F(\omega+\Omega)}{\Omega} \to -\frac{\partial n_F}{\partial\omega} \tag{2.71}$$

which for low T is very sharply peaked at $\omega = 0$. Thus, evaluating the rest of the integrand for $\omega \to 0$, noting that $\Sigma_{ret}(0) = -i\Gamma_0$, performing the frequency integral via

$$\int_{-\infty}^{\infty}\omega^2\left(-\frac{\partial n_F}{\partial\omega}\right)d\omega = \frac{\pi^2}{3}k_B^2T^2 \tag{2.72}$$

and integrating over momentum, we obtain the bare bubble thermal conductivity in the universal limit:

$$\frac{\kappa_0}{T} = \left(\frac{\pi^2}{3}k_B^2\right)\frac{1}{\pi^2}\frac{v_f^2+v_2^2}{v_f v_2}. \tag{2.73}$$

Neglecting the v_2^2 term in the numerator, this result and its finite temperature corrections, were originally calculated by Graf *et al.* [20]. The gap term was first obtained by Senthil *et al.* [21] via a physical argument of Wiedemann-Franz correspondence

with their expression for spin conductivity. It arises here as a direct result of the additional gap term found in our calculation of the thermal current for a d-wave superconductor.

2.4.3 Vertex Corrections (Thermal)

The bare bubble result derived in the previous section can be improved upon by including the contribution of the *ladder corrections* to the bare vertex (see Fig. 2-4 of Sec. 2.8). A generalized polarization function including such vertex corrections has been derived in Sec. 2.8. By plugging the appropriate parameters into this general formula, Eq. (2.160), both terms of the thermal conductivity (the Fermi term with parameters $\mathbf{v}_f$, $\tilde{\tau}_3$, and $\omega+\Omega/2$ and the gap term with parameters $\mathbf{v}_2$, $\tilde{\tau}_1$, and $\omega+\Omega/2$) can be obtained. Hence we find that

$$\begin{aligned}\frac{\kappa(\Omega,T)}{T} &= \frac{1}{2\pi^2 v_f v_2}\int_{-\infty}^{\infty} d\omega\, \frac{n_F(\omega)-n_F(\omega+\Omega)}{\Omega}\left(\frac{\omega+\frac{\Omega}{2}}{T}\right)^2 \\ &\times \left[v_f^2 \mathrm{Re}\left[J_2^{(3)}(\omega,\Omega)-J_1^{(3)}(\omega,\Omega)\right]+v_2^2\mathrm{Re}\left[J_2^{(1)}(\omega,\Omega)-J_1^{(1)}(\omega,\Omega)\right]\right]\end{aligned} \tag{2.74}$$

where J_1^α and J_2^α are defined in Sec. 2.8. In the universal limit ($\Omega \to 0$, $T \to 0$), the Fermi function factor is sharply peaked at $\omega = 0$. Thus, evaluating the J-functions for $\Omega, \omega \to 0$, performing the frequency integral via Eq. (2.72), and noting that

$$\begin{aligned} J_2^{(3)}(0,0) &= -J_1^{(1)}(0,0) \\ J_1^{(3)}(0,0) &= -J_2^{(1)}(0,0) \end{aligned} \tag{2.75}$$

we find that the universal limit thermal conductivity takes the form

$$\frac{\kappa_0}{T} = \left(\frac{\pi^2}{3}k_B^2\right)\frac{1}{\pi^2}\frac{v_f^2+v_2^2}{v_f v_2}\beta_{vc}^T \tag{2.76}$$

$$\beta_{vc}^T = \frac{\frac{1}{2}}{1-\gamma_{A2}^{(0)}} + \frac{\frac{1}{2}}{1+\gamma_{A1}^{(0)}\left(1+\frac{\gamma_{B1}^{(0)}}{\gamma_{A1}^{(0)}}\frac{\gamma_{B1}^{(0)}\left(2\ln\frac{p_0}{\Gamma_0}-2\right)}{1-\gamma_{A1}^{(0)}\left(2\ln\frac{p_0}{\Gamma_0}-2\right)}\right)} \tag{2.77}$$

where β_{vc}^T is the thermal vertex correction factor and the γ's are defined in Eq. (2.32). As for the electrical case, the thermal vertex correction must generally be evaluated numerically. The results of such numerical calculations (presented in Sec. 2.9) can be summarized as follows: (1) For all scattering strengths (from Born to unitary) the thermal vertex correction is negligible compared to the electrical vertex correction. (2) In the small impurity density limit, $\beta_{vc}^T - 1$ vanishes approximately as $[\ln(p_0/\Gamma_0)]^{-1}$. Thus, to zeroth order in the density of impurities, vertex corrections do not contribute.

Hence,

$$\beta_{vc}^{T} \approx 1 \tag{2.78}$$

and the universal limit thermal conductivity takes its bare bubble form

$$\frac{\kappa_0}{T} = \left(\frac{\pi^2}{3}k_B^2\right)\frac{1}{\pi^2}\frac{v_f^2 + v_2^2}{v_f v_2}. \tag{2.79}$$

This is in stark contrast to the case of electrical conductivity where we found a significant vertex correction even to zeroth order in the impurity density.

2.5 Spin Conductivity

For the spin conductivity case, the Kubo formula takes the form

$$\sigma^s(\Omega, T) = -\frac{\mathrm{Im}\,\Pi_{ret}^s(\Omega)}{\Omega} \tag{2.80}$$

where $\Pi_{ret}^s(\Omega) = \Pi^s(i\Omega \to \Omega + i\delta)$ and $\Pi^s(i\Omega)$ is the finite temperature current-current correlation function (or polarization function). Here the current that enters the correlation function is the spin current derived below.

2.5.1 Spin Current

To find an expression for the spin current operator in an anisotropic superconductor, we can write down the Hamiltonian and spin density operators and use the spin continuity equation to obtain the current. For spin, the continuity equation is

$$\dot{\rho}^s(\mathbf{x}) = -\nabla \cdot \mathbf{j}^s(\mathbf{x}) \tag{2.81}$$

where ρ^s is the spin density and $\mathbf{j}^s$ is the spin current density. The spin density equation of motion takes the standard form

$$\dot{\rho}^s(\mathbf{x}) = -i\left[\rho^s(\mathbf{x}), H\right]. \tag{2.82}$$

Thus, combining the two equations and using a Fourier representation for both the spin density and the spin current we find that

$$\mathbf{q} \cdot \mathbf{j}_q^s = \left[\rho_q^s, H\right]. \tag{2.83}$$

The Fourier transform of the spin density operator is given by

$$\rho_q^s = \sum_{k,\omega,\alpha} S_\alpha c_{k\alpha}^\dagger c_{k+q\alpha} = s\sum_{k,\omega}\left(c_{k\uparrow}^\dagger c_{k+q\uparrow} - c_{-k\downarrow}^\dagger c_{-k+q\downarrow}\right) \tag{2.84}$$

where $S_\alpha = \pm\frac{1}{2}$ and $s \equiv \frac{1}{2}$. In the mean field approximation, the Hamiltonian for a superconductor is expressed as

$$H = \sum_{k,\omega} \left[\epsilon_k \left(c^\dagger_{k\uparrow} c_{k\uparrow} + c^\dagger_{-k\downarrow} c_{-k\downarrow} \right) - \Delta_k \left(c^\dagger_{k\uparrow} c^\dagger_{-k\downarrow} + c_{-k\downarrow} c_{k\uparrow} \right) \right]. \tag{2.85}$$

Thus, evaluating the commutator of Eq. (2.84) and Eq. (2.85) using fermionic anti-commutation relations we obtain

$$\begin{aligned} \mathbf{q} \cdot \mathbf{j}^s_q &= s \sum_{k,\omega} \left[(\epsilon_{k+q} - \epsilon_k) \left(c^\dagger_{k\uparrow} c_{k+q\uparrow} - c_{-k\downarrow} c^\dagger_{-(k+q)\downarrow} \right) \right. \\ &- \left. (\Delta_{k+q} - \Delta_k) \left(c^\dagger_{k\uparrow} c^\dagger_{-(k+q)\downarrow} + c_{-k\downarrow} c_{k+q\uparrow} \right) \right]. \end{aligned} \tag{2.86}$$

In the limit as $q \to 0$

$$\epsilon_{k+q} - \epsilon_k \approx \mathbf{q} \cdot \frac{\partial \epsilon_k}{\partial \mathbf{k}} \equiv \mathbf{q} \cdot \mathbf{v}_f \tag{2.87}$$

$$\Delta_{k+q} - \Delta_k \approx \mathbf{q} \cdot \frac{\partial \Delta_k}{\partial \mathbf{k}} \equiv \mathbf{q} \cdot \mathbf{v}_2 \tag{2.88}$$

Hence, expressing the creation and annihilation operators in terms of 2×2 Nambu matrix notation we find that

$$\mathbf{j}^s(0, \Omega) = s \sum_{k,\omega} \left[\mathbf{v}_f \Psi^\dagger_k \tilde{\tau}_3 \Psi_{k+q} - \mathbf{v}_2 \Psi^\dagger_k \tilde{\tau}_1 \Psi_{k+q} \right]. \tag{2.89}$$

Note that the spin current takes precisely the same form as the thermal current, Eq. (2.69), with an appropriate change of coupling parameter.

2.5.2 Bare Bubble (Spin)

As in the thermal conductivity case, the spin current has both a "Fermi" term and a "gap" term. Hence, evaluating the current-current correlation function and noting (as before) that the cross-terms cancel, we find that the spin conductivity consists of two bubbles: a Fermi term with $\mathbf{v}_f$ and $\tilde{\tau}_3$ on each vertex and a gap term with $\mathbf{v}_2$ and $\tilde{\tau}_1$ on each vertex. These are precisely the bubbles that we evaluated for the thermal case except that here the coupling constant is the spin ($s = 1/2$) rather than the frequency.

Neglecting vertex corrections, each of the two bubbles can be evaluated by plugging the appropriate set of parameters into the bare bubble generalized polarization function, Eq. (2.111), derived in Sec. 2.7. Doing so we find that

$$\begin{aligned} \sigma^s(\Omega, T) = \frac{s^2}{\pi^2 v_f v_2} \int \frac{d^2p}{2\pi} \int_{-\infty}^{\infty} d\omega \frac{n_F(\omega) - n_F(\omega + \Omega)}{\Omega} \\ \times \left[v_f^2 \mathrm{Tr} \left[\tilde{G}''_{ret}(\mathbf{p}, \omega) \tilde{\tau}_3 \tilde{G}''_{ret}(\mathbf{p}, \omega + \Omega) \tilde{\tau}_3 \right] + v_2^2 \mathrm{Tr} \left[\tilde{G}''_{ret}(\mathbf{p}, \omega) \tilde{\tau}_1 \tilde{G}''_{ret}(\mathbf{p}, \omega + \Omega) \tilde{\tau}_1 \right] \right]. \end{aligned} \tag{2.90}$$

In the universal limit ($\Omega \to 0$, $T \to 0$),

$$\frac{n_F(\omega) - n_F(\omega + \Omega)}{\Omega} \to -\frac{\partial n_F}{\partial \omega} \to \delta(\omega). \tag{2.91}$$

Thus, evaluating the rest of the integrand in the $\omega \to 0$ limit, noting that $\Sigma_{ret}(0) = -i\Gamma_0$, and integrating over momentum, we obtain the universal limit bare bubble spin conductivity:

$$\sigma_0^s = \frac{s^2}{\pi^2} \frac{v_f^2 + v_2^2}{v_f v_2}. \tag{2.92}$$

This agrees (aside from a disputed factor of 2) with the result obtained by Senthil *et al.* [21].

2.5.3 Vertex Corrections (Spin)

As in the electrical and thermal cases discussed previously, the bare bubble result derived above can be improved upon by including the contribution of the ladder corrections to the bare vertex. By plugging the appropriate parameters into the generalized polarization function (including vertex corrections) derived in Sec. 2.8, both the Fermi term and the gap term of the spin conductivity can be obtained. Doing so we find that

$$\begin{aligned} \sigma^s(\Omega, T) &= \frac{s^2}{2\pi^2 v_f v_2} \int_{-\infty}^{\infty} d\omega \, \frac{n_F(\omega) - n_F(\omega + \Omega)}{\Omega} \\ &\times \left[v_f^2 \mathrm{Re}\left[J_2^{(3)}(\omega, \Omega) - J_1^{(3)}(\omega, \Omega) \right] + v_2^2 \mathrm{Re}\left[J_2^{(1)}(\omega, \Omega) - J_1^{(1)}(\omega, \Omega) \right] \right] \end{aligned} \tag{2.93}$$

where J_1^α and J_2^α are defined in Sec. 2.8. In the universal limit ($\Omega \to 0$, $T \to 0$), we can make use of Eq. (2.91) to evaluate the frequency integral and find that

$$\sigma_0^s = \frac{s^2}{\pi^2} \frac{v_f^2 + v_2^2}{v_f v_2} \beta_{vc}^s \tag{2.94}$$

where the spin vertex correction factor, β_{vc}^s, is identical to the thermal vertex correction factor, β_{vc}^T, defined in Eq. (2.77). Thus, mirroring the analysis described in Sec. 2.4.3, we note that for small impurity density, $\beta_{vc}^s \approx 1$ and the universal limit spin conductivity takes its bare bubble form

$$\sigma_0^s = \frac{s^2}{\pi^2} \frac{v_f^2 + v_2^2}{v_f v_2}. \tag{2.95}$$

As in the thermal case and in contrast to the electrical case, vertex corrections do not contribute (to zeroth order in the impurity density).

2.6 Conclusions

In the presence of impurities, the gap symmetry of a d-wave superconductor yields the generation of impurity-induced quasiparticles at the gap nodes. The transport properties of the resulting system are quite unique since such quasiparticles are both generated and scattered by impurities. In the $\Omega \to 0$, $T \to 0$ limit, bare bubble calculations indicate that transport coefficients are "universal", independent of the impurity density or scattering rate. However, once the contributions of vertex corrections (as well as Fermi-liquid corrections) are included, we find that (putting in the $\hbar$'s) the electrical, thermal, and spin conductivities in this universal limit take the form

$$\sigma_0 = \frac{e^2}{\hbar\pi^2}\frac{v_f}{v_2}\beta_{vc}\alpha_{fl}^2 \tag{2.96}$$

$$\frac{\kappa_0}{T} = \frac{\left(\frac{\pi^2}{3}k_B^2\right)}{\hbar\pi^2}\left(\frac{v_f}{v_2}+\frac{v_2}{v_f}\right) \tag{2.97}$$

$$\sigma_0^s = \frac{s^2}{\hbar\pi^2}\left(\frac{v_f}{v_2}+\frac{v_2}{v_f}\right) \tag{2.98}$$

where β_{vc} is the scattering dependent vertex correction defined in Eq. (2.38) and α_{fl} is the electrical current renormalization factor induced by Fermi-liquid interactions. Note that these are the 2D conductivities of a single CuO_2 plane. To obtain 3D conductivities, they must be multiplied by the number of CuO_2 planes per unit length stacked along the c-axis.

The "law" of Wiedemann and Franz suggests that the electrical and thermal transport coefficients should be related such that $\frac{\kappa}{\sigma T} = \frac{\pi^2}{3}\frac{k_B^2}{e^2}$. However, while the expressions above support the analogous relationship for spin and heat, $\frac{\kappa}{\sigma^s T} = \frac{\pi^2}{3}\frac{k_B^2}{s^2}$, they indicate three sources of charge-heat Wiedemann-Franz violation: current operator definition corrections, vertex corrections, and Fermi-liquid corrections. First of all, since the electrical current has only a Fermi term while the thermal and spin currents include both a Fermi term and a gap term, σ_0 is proportional to the ratio v_f/v_2 while κ_0 and σ_0^s involve an extra v_2/v_f term. These extra terms arise when the thermal and spin current operators are corrected to account for the anisotropy of the order parameter. However, since $v_f/v_2 \sim 14$ for YBCO [27], this type of violation is of more qualitative than quantitative importance. Secondly, unless impurity scattering is completely isotropic in k-space, the electrical conductivity contains a scattering dependent vertex correction, β_{vc}, which cannot be neglected even to zeroth order in impurity density. However, analogous corrections to the thermal and spin conductivities vanish in the small impurity density limit. Thus we expect a scattering dependent enhancement of σ_0 that is absent in κ_0 and σ_0^s. Finally, due to Fermi-liquid interactions between the quasiparticle current and the supercurrent, the electrical conductivity obtains a Fermi-liquid correction factor, α_{fl}^2. Corresponding corrections to the thermal and spin conductivities are negligible since, unlike electric fields, thermal gradients and Zeeman fields do not induce a supercurrent. (See

Sec. 2.3.5 and Ref. [23] for more details.)

The physical origin of the first two corrections lies with the velocity dependence of the current operators. Although somewhat obscured in the Nambu formalism, when our current operators, Eqs. (2.22), (2.69), and (2.89), are rewritten in the quasiparticle basis, it is clear that the electrical current is proportional to the Fermi velocity, $\mathbf{v}_f = \partial\epsilon_k/\partial\mathbf{k}$, while the thermal and spin currents are proportional to the group velocity, $\mathbf{v}_G = \partial E_k/\partial\mathbf{k}$. This difference arises because quasiparticles carry definite energy and spin but do not carry definite charge. Since energy and spin are well defined in the quasiparticle basis, thermal and spin currents are proportional to the group velocity, the derivative of the quasiparticle dispersion. By contrast, the electron and hole parts of each quasiparticle have opposite charge and opposite velocity. Therefore each part carries the same electrical current, proportional to the normal state Fermi velocity. This point was emphasized in Ref. [12]. For a d-wave superconductor where both ϵ_k and Δ_k are momentum-dependent, the group velocity will have both a $\mathbf{v}_f$ component and a $\mathbf{v}_2$ component while the Fermi velocity can only have a $\mathbf{v}_f$ component (see Fig. 2-2). This is the source of the extra gap terms in the thermal and spin conductivities. (Similar conclusions were drawn by Moreno and Coleman [41].)

The role of vertex corrections can be understood by considering the graphical depictions of the Fermi velocity and group velocity presented in Fig. 2-2. Throughout the area of a node, the magnitude and direction of the Fermi velocity is approximately constant. Thus, the electrical current can relax much more effectively via scattering from node to node than it can via scattering within a single node. It is therefore necessary to distinguish, mathematically, between the effects of intra-node scattering and inter-node scattering. This is accomplished through the inclusion of vertex corrections. In contrast, the group velocity varies significantly over the area of a node. Therefore, the thermal and spin currents can relax through either intra-node scattering or scattering between nodes. As a result, the different types of scattering play nearly the same role and need not be distinguished. Hence, vertex corrections do not contribute to the thermal and spin conductivity.

The velocity ratio, v_f/v_2, is a fundamental material parameter which measures the anisotropy of the quasiparticle excitation spectrum. Therefore, an important objective in measuring quantities such as the superfluid density and the universal-limit transport coefficients, which all depend on v_f/v_2, is to obtain the value of this ratio. However, due to vertex corrections and/or Fermi-liquid corrections, the electrical conductivity and superfluid density depend on parameters (such as the scattering potential and/or interaction energy) with values that are not well known. However the thermal conductivity and the spin conductivity involve neither vertex corrections nor Fermi-liquid corrections. Since the spin conductivity has yet to be measured experimentally, κ_0 is the only experimentally-accessable transport coefficient that is truly "universal". It is therefore the quantity from which the value of v_f/v_2 can be most directly obtained. On the other hand, the temperature-dependent part of the superfluid density, Eq. (2.51), is proportional to $\alpha_{fl}^2 v_f/v_2$. Hence, these two measurements can be combined to determine the Fermi-liquid factor, α_{fl}.

In fact, while this paper was in preparation, Chiao *et al.* [42] applied these con-

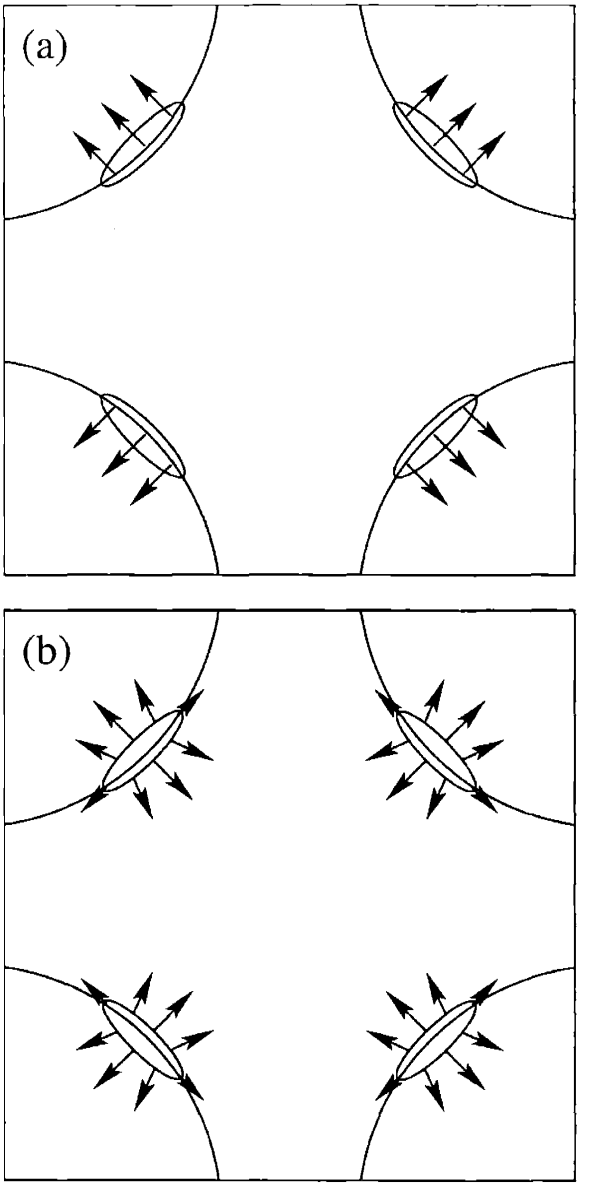

Figure 2-2: Schematic depictions of the (a) electrical current and (b) thermal/spin current in the vicinity of the four gap nodes. Electrical current is proportional to the Fermi velocity, $\mathbf{v}_f = \partial\epsilon_k/\partial\mathbf{k}$, whereas thermal/spin current is proportional to the group velocity, $\mathbf{v}_G = \partial E_k/\partial\mathbf{k}$. The ellipses drawn at each node denote (at a very exaggerated scale) the regions of k-space within which impurity-induced quasiparticles are generated in the universal limit. (Note that in the small impurity density regime with which we are concerned ($\Gamma_0 \ll \Delta_0$), these nodal regions are point-like on the scale of the Brillouin zone.)

clusions to the results of a series of recent experiments performed on optimally-doped $Bi_2Sr_2CaCu_2O_8$ (BSCCO). By analyzing the residual linear term in their very low temperature thermal conductivity measurements in terms of Eq. (2.97), they obtained a value for the anisotropy ratio, $v_f/v_2 = 19$. This is roughly the same value obtained from the ARPES measurements of Mesot *et al.* [29]. Going further, by combining this result with the temperature-dependence of the superfluid density measured by Waldram and co-workers [43] and making use of Eq. (2.51), they extracted a value for the Fermi-liquid correction, $\alpha_{fl}^2 = 0.43$. These results provide an experimental verification of our analysis.

2.7 Appendix A: Bare Bubble Calculation

In the absence of vertex corrections, our calculations of electrical, thermal, and spin conductivity all require the evaluation of *bare bubble* diagrams depicting various types of polarization functions. The details of these different calculations are all quite similar. They differ only in the coupling parameter, velocity, and Pauli matrix contributed by each bare vertex. Rather than repeating the same basic calculation several times, it is convenient to calculate a generalized polarization function here which can be referred to for each of the specific cases of interest. This generalized function $\overleftrightarrow{\Pi}^{g\ell\alpha}$, will depend on a coupling parameter g, a velocity $\mathbf{v}_\ell$, and a Nambu space Pauli matrix $\tilde{\tau}_\alpha$ where

$$\begin{aligned} g &= \{e, s(=1/2), \omega + \Omega/2\} \\ \mathbf{v}_\ell &= \{\mathbf{v}_f, \mathbf{v}_2\} \\ \tilde{\tau}_\alpha &= \{\tilde{\tau}_0(=\tilde{\mathbb{1}}), \tilde{\tau}_1, \tilde{\tau}_2, \tilde{\tau}_3\}. \end{aligned}$$

Evaluating the diagram in Fig. 2-3 we find that

$$\overleftrightarrow{\Pi}^{g\ell\alpha}(i\Omega) = \frac{1}{\beta}\sum_{k,i\omega} g^2 \mathbf{v}_\ell \mathbf{v}_\ell \mathrm{Tr}\Big[\tilde{\mathcal{G}}(\mathbf{k}, i\omega)\tilde{\tau}_\alpha \tilde{\mathcal{G}}(\mathbf{k}, i\omega + i\Omega)\tilde{\tau}_\alpha\Big] \tag{2.99}$$

where $\tilde{\mathcal{G}}(\mathbf{k}, i\omega)$ is the 2×2 Nambu matrix form of the Matsubara Green's function. For a d-wave superconductor at temperatures much less than the gap maximum, quasiparticles are generated primarily at the four gap nodes [16, 12]. Thus, linearizing the quasiparticle spectrum about the nodes and defining a coordinate system (k_1, k_2) at each node with $\hat{\mathbf{k}}_1$ ($\hat{\mathbf{k}}_2$) perpendicular (parallel) to the Fermi surface, we can replace our momentum sum by an integral over the k-space area surrounding each node. If

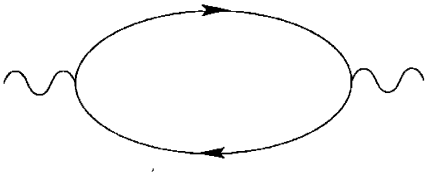

Figure 2-3: Bare polarization bubble.

we further define a scaled momentum (p_1, p_2) we can let

$$\sum_k \to \sum_{j=1}^{4} \int \frac{d^2k}{(2\pi)^2} \to \sum_{j=1}^{4} \int \frac{d^2p}{(2\pi)^2 v_f v_2} \tag{2.100}$$

where $p_1 \equiv v_f k_1 = \varepsilon_{\mathbf{k}}$ and $p_2 \equiv v_2 k_2 = \Delta_{\mathbf{k}}$. Since $\mathbf{v}_f = v_f \hat{\mathbf{k}}_1$ and $\mathbf{v}_2 = v_2 \hat{\mathbf{k}}_2$ at each of the four nodes, the sum over nodes yields

$$\sum_{j=1}^{4} \mathbf{v}_\ell^{(j)} \mathbf{v}_\ell^{(j)} = 2v_\ell^2 \overleftrightarrow{\mathbb{1}}. \tag{2.101}$$

This, in turn, allows the definition of a scalar polarization function via

$$\overleftrightarrow{\Pi}^{g\ell\alpha}(i\Omega) \equiv \Pi^{g\ell\alpha}(i\Omega) \overleftrightarrow{\mathbb{1}}. \tag{2.102}$$

Defining a spectral representation for $\tilde{\mathcal{G}}$, we can write

$$\tilde{\mathcal{G}}(\mathbf{p}, i\omega) = \int_{-\infty}^{\infty} \frac{\tilde{A}(\mathbf{p}, \omega_1)}{i\omega - \omega_1} d\omega_1 \tag{2.103}$$

where

$$\tilde{A}(\mathbf{p}, \omega) = -\frac{1}{\pi} \tilde{G}''_{ret}(\mathbf{p}, \omega) \tag{2.104}$$

and $\tilde{G}''_{ret}$ is the imaginary part of the retarded Green's function. Plugging back into Eq. (2.99) we obtain

$$\Pi^{g\ell\alpha}(i\Omega) = \frac{2v_\ell^2}{v_f v_2} \int \frac{d^2p}{(2\pi)^2} \int d\omega_1 \int d\omega_2 \mathrm{Tr}\left[\tilde{A}(\mathbf{p}, \omega_1)\tilde{\tau}_\alpha \tilde{A}(\mathbf{p}, \omega_2)\tilde{\tau}_\alpha\right] S \tag{2.105}$$

where

$$S = \frac{1}{\beta} \sum_{i\omega} g^2 \frac{1}{i\omega - \omega_1} \frac{1}{i\omega + i\Omega - \omega_2}. \tag{2.106}$$

Evaluating the Matsubara sum in the standard way [13] we pick up a contribution from each of the poles of the summand. Since the intermediate results differ depending on the frequency-dependence of the coupling parameter, it is best to handle the frequency-independent coupling and frequency-dependent coupling cases separately.

For $g = \{e, s\}$ (frequency-independent coupling), the sum is straightforward. Adding the contribution of the two poles and then continuing $i\Omega \to \Omega + i\delta$ we obtain the retarded function

$$S_{ret} = S(i\Omega \to \Omega + i\delta) = g^2 \frac{n_F(\omega_1) - n_F(\omega_2)}{\omega_1 - \omega_2 + \Omega + i\delta} \tag{2.107}$$

where

$$n_F(\omega) = \frac{1}{e^{\beta\omega} + 1} \tag{2.108}$$

is the Fermi function.

For $g = \omega + \Omega/2$ (frequency-dependent coupling), we proceed in the same way but there are a few technicalities that must be clarified. First of all, it should be understood that within the Matsubara sum we really mean $g \to i\omega + i\Omega/2$. Only after the sum has been evaluated and all frequencies have been continued to the real axis should the stated form of the coupling parameter be taken literally. Secondly, note that with this frequency dependent g, the summand has two extra powers of frequency. As a result, the sum appears to be divergent. However, as discussed by Ambegaokar and Griffin [33], this apparent divergence results from an improper treatment of time-derivatives within the time-ordered correlation function and should be ignored. Doing so, we proceed just as before. Adding the contribution of the two summand poles and continuing the external frequency to the real axis we find that

$$S_{ret} = \frac{(\omega_1 + \frac{\Omega}{2})^2 n_F(\omega_1) - (\omega_2 - \frac{\Omega}{2})^2 n_F(\omega_2)}{\omega_1 - \omega_2 + \Omega + i\delta}. \tag{2.109}$$

Plugging Eqs. (2.107) and (2.109) back into Eq. (2.105), writing the spectral function in terms of the retarded Green's function via Eq. (2.104), and using the identity

$$\frac{1}{x + i\delta} = \mathrm{P}\frac{1}{x} - i\pi\delta(x) \tag{2.110}$$

to take the imaginary part, we find that

$$\begin{aligned} \mathrm{Im}\,\Pi^{g\ell\alpha}_{ret}(\Omega) &= \frac{1}{\pi^2}\frac{v_\ell^2}{v_f v_2}\int\frac{d^2p}{2\pi}\int_{-\infty}^{\infty} d\omega\, g^2\left(n_F(\omega+\Omega) - n_F(\omega)\right) \\ &\times \mathrm{Tr}\Big[\tilde{G}''_{ret}(\mathbf{p},\omega)\tilde{\tau}_\alpha\tilde{G}''_{ret}(\mathbf{p},\omega+\Omega)\tilde{\tau}_\alpha\Big] \end{aligned} \tag{2.111}$$

for all three coupling parameters $g = \{e, s, \omega + \Omega/2\}$. Neglecting vertex corrections, this is the imaginary part of the generalized retarded polarization function. The real part can be obtained via Kramers-Kronig analysis. By specifying different input parameters, Eq. (2.111) can be used to obtain the electrical, thermal, and spin conductivity.

2.8 Appendix B: Vertex Corrections

Unless the scattering potential is completely isotropic, the bare bubble results of Sec. 2.7 can be improved upon by including the contributions of vertex corrections. In this section the *ladder corrections* depicted in Fig. 2-4 will be included. Once again, our object is to obtain an expression for a generalized polarization function, $\overleftrightarrow{\Pi}^{g\ell\alpha}$, in which each of the vertices contribute a coupling parameter g, a velocity $\mathbf{v}_\ell$, and a Nambu space Pauli matrix $\tilde{\tau}_\alpha$. Evaluating the diagram in Fig. 2-4(a) and noting that $\mathbf{v}_\ell \equiv v_\ell\hat{\mathbf{k}}_\ell$ we find that the generalized polarization function takes the form

$$\overleftrightarrow{\Pi}^{g\ell\alpha}(i\Omega) = \frac{1}{\beta}\sum_{i\omega}\sum_{k} g^2 v_\ell^2\hat{\mathbf{k}}_\ell\mathrm{Tr}\Big[\tilde{\mathcal{G}}(\mathbf{k},i\omega)\tilde{\tau}_\alpha\tilde{\mathcal{G}}(\mathbf{k},i\omega+i\Omega)\tilde{\tau}_\alpha\tilde{\mathbf{\Gamma}}^{\ell\alpha}(\mathbf{k},i\omega,i\Omega)\Big] \tag{2.112}$$

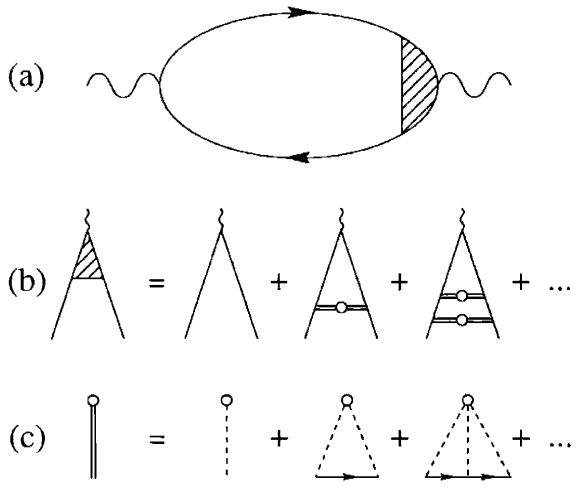

Figure 2-4: (a) Polarization bubble with dressed vertex. (b) Ladder series. (c) T-matrix series.

which is equivalent to the bare bubble result, Eq. (2.99), with the unit vector $\hat{\mathbf{k}}_\ell$ from the second bare vertex replaced by a more general vertex function $\tilde{\mathbf{\Gamma}}^{\ell\alpha}$. Evaluating the diagram series in Fig. 2-4(b) we obtain an equation which can be solved for the vertex function:

$$\tilde{\tau}_\alpha \tilde{\mathbf{\Gamma}}^{\ell\alpha}(\mathbf{k}) = \hat{\mathbf{k}}_\ell \tilde{\tau}_\alpha + n_i \sum_{k''} \tilde{T}_{kk''}(i\omega + i\Omega)\tilde{\mathcal{G}}(\mathbf{k}'', i\omega + i\Omega)\tilde{\tau}_\alpha \tilde{\mathbf{\Gamma}}^{\ell\alpha}(\mathbf{k}'')\tilde{\mathcal{G}}(\mathbf{k}'', i\omega)\tilde{T}_{k''k}(i\omega) \tag{2.113}$$

where n_i is the impurity density and $\tilde{T}_{kk'}(i\omega)$ is the impurity scattering T-matrix defined by the diagram series in Fig. 2-4(c). Multiplying from the left by $\tilde{\tau}_\alpha$ we can define

$$\tilde{\Gamma}^{\ell\alpha}(\mathbf{k}, i\omega, i\Omega) = \hat{\mathbf{k}}_\ell \left[\tilde{\mathbb{1}} + \tilde{\Lambda}^\alpha(i\omega, i\Omega)\right] \tag{2.114}$$

where

$$\hat{\mathbf{k}}_\ell \tilde{\Lambda}^\alpha = n_i \sum_{k''} \tilde{\tau}_\alpha \tilde{T}_{kk''}(i\omega + i\Omega)\tilde{\mathcal{G}}(\mathbf{k}'', i\omega + i\Omega)\tilde{\tau}_\alpha \tilde{\mathbf{\Gamma}}^{\ell\alpha}(\mathbf{k}'')\tilde{\mathcal{G}}(\mathbf{k}'', i\omega)\tilde{T}_{k''k}(i\omega). \tag{2.115}$$

Acting on both sides of Eq. (2.114), using Eq. (2.115) to replace the left hand side by $\hat{\mathbf{k}}'_\ell \tilde{\Lambda}^\alpha$, and noting that by the symmetry of the scattering potential

$$\sum_k \hat{\mathbf{k}}_\ell \to \hat{\mathbf{k}}'_\ell \sum_k (\hat{\mathbf{k}}' \cdot \hat{\mathbf{k}}) \tag{2.116}$$

we find that

$$\tilde{\Lambda}^\alpha = n_i \sum_k (\hat{\mathbf{k}}' \cdot \hat{\mathbf{k}})\tilde{\tau}_\alpha \tilde{T}_{k'k}(i\omega + i\Omega)\tilde{\mathcal{G}}(\mathbf{k}, i\omega + i\Omega)\tilde{\tau}_\alpha \left[\tilde{\mathbb{1}} + \tilde{\Lambda}^\alpha\right] \tilde{\mathcal{G}}(\mathbf{k}, i\omega)\tilde{T}_{kk'}(i\omega) \tag{2.117}$$

where $\mathbf{k}'$ is the final momentum of a scattering event.

An expression for the T-matrix in terms of the scattering potential $V_{kk'}$ and the Matsubara self-energy $\Sigma(i\omega)$ (itself a function of the scattering potential) can be

obtained by evaluating the diagram series in Fig. 2-4(c).

$$\tilde{T}_{kk'}(i\omega) = \tilde{\tau}_3 V_{kk'} + \sum_{k_1} \tilde{\tau}_3 \tilde{\mathcal{G}}(\mathbf{k_1}, i\omega) \tilde{\tau}_3 V_{kk_1} V_{k_1 k'} + \cdots \tag{2.118}$$

As discussed in Sec. 2.7, at temperatures low compared to the gap maximum, quasiparticles are only generated in the small regions of k-space surrounding each of the four gap nodes. Hence we can let

$$\sum_k \rightarrow \sum_{j=1}^{4} \int \frac{d^2p}{(2\pi)^2 v_f v_2} \tag{2.119}$$

and note that the initial and final momenta of a scattering event must always be approximately equal to the k-space location of one of the four nodes. Thus if j and j' are node indices (1 to 4), the scattering potential takes the form

$$V_{kk'} \rightarrow V_{jj'} \rightarrow (\underline{V})_{jj'} \tag{2.120}$$

where $\underline{V}$ is a 4×4 matrix in node space. Due to the symmetry of the nodes, $\underline{V}$ consists of only three independent parameters: V_1 for intra-node scattering, V_2 for adjacent-node scattering, and V_3 for opposite-node scattering (see Fig. 2-1 in Sec. 2.2).

$$\underline{V} = \begin{pmatrix} V_1 & V_2 & V_3 & V_2 \\ V_2 & V_1 & V_2 & V_3 \\ V_3 & V_2 & V_1 & V_2 \\ V_2 & V_3 & V_2 & V_1 \end{pmatrix} \tag{2.121}$$

Hence Eq. (2.118) becomes

$$\tilde{T}_{jj'}(i\omega) = \tilde{\tau}_3 (\underline{V})_{jj'} + \tilde{\tau}_3 \left(\int \frac{d^2p}{(2\pi)^2 v_f v_2} \tilde{\mathcal{G}}(\mathbf{p}, i\omega) \right) \tilde{\tau}_3 (\underline{V}^2)_{jj'} + \cdots \tag{2.122}$$

Performing the node integration we see that the integral of the Green's function about a node is a scalar in Nambu space (proportional to $\tilde{1\!\!1}$). Since $\tilde{\tau}_3$ raised to an even power is equal to $\tilde{1\!\!1}$, the T-matrix splits into a $\tilde{\tau}_3$ component and a $\tilde{1\!\!1}$ component. Summing the resulting geometric series we find that

$$\begin{aligned} \tilde{T}_{jj'} &= T^a_{jj'} \tilde{\tau}_3 + T^b_{jj'} \tilde{1\!\!1} \\ T^a_{jj'} &= \left(\frac{\underline{V}}{1 - F'(i\omega)^2 \underline{V}^2} \right)_{jj'} \\ T^b_{jj'} &= \left(\frac{-F'(i\omega) \underline{V}^2}{1 - F'(i\omega)^2 \underline{V}^2} \right)_{jj'} \end{aligned} \tag{2.123}$$

where

$$F'(i\omega) = \frac{F(i\omega - \Sigma(i\omega))}{4\pi v_f v_2} \tag{2.124}$$

$$F(x) \equiv x \ln\left(1 - \frac{p_0^2}{x^2}\right) \tag{2.125}$$

and p_0 is the large scaled momentum cutoff defined in Sec. 2.2.

Taking the Nambu space trace of Eq. (2.117), cyclically permuting within the trace, and replacing the momentum sum with a scaled integral about the nodes via Eq. (2.119) yields

$$\begin{aligned} \mathrm{Tr}\,\tilde{\Lambda}^\alpha &= \mathrm{Tr}\Big[n_i \int \frac{d^2p}{(2\pi)^2 v_f v_2} \tilde{\mathcal{G}}(\mathbf{p}, i\omega) \\ &\times \sum_{j=1}^{4} \left(\hat{\mathbf{k}}^{j'} \cdot \hat{\mathbf{k}}^{j}\right) \tilde{T}_{jj'}(i\omega)\tilde{\tau}_\alpha \tilde{T}_{j'j}(i\omega + i\Omega)\tilde{\mathcal{G}}(\mathbf{p}, i\omega + i\Omega)\tilde{\tau}_\alpha \left(\tilde{\mathbb{1}} + \tilde{\Lambda}^\alpha\right)\Big]. \end{aligned} \tag{2.126}$$

Defining node j' to be node 1 we can write for $j = 1, 2, 3, 4$

$$\begin{aligned} \mathbf{k}^j &= \left\{(\pm\frac{\pi}{2}, \pm\frac{\pi}{2})\right\} \\ \hat{\mathbf{k}}^{j'} \cdot \hat{\mathbf{k}}^{j} &= \{1, 0, -1, 0\} \\ \tilde{T}_{jj'} = \tilde{T}_{j'j} &\equiv \left\{\tilde{T}_1, \tilde{T}_2, \tilde{T}_3, \tilde{T}_2\right\} \end{aligned}$$

and therefore

$$\begin{aligned} &\sum_{j=1}^{4} \left(\hat{\mathbf{k}}^{j'} \cdot \hat{\mathbf{k}}^{j}\right) \tilde{T}_{jj'}(i\omega)\tilde{\tau}_\alpha \tilde{T}_{j'j}(i\omega + i\Omega) \\ &= \tilde{T}_n(i\omega)\tilde{\tau}_\alpha \tilde{T}_n(i\omega + i\Omega)[|_{n=1} - |_{n=3}] \\ &= \frac{4\pi v_f v_2}{n_i}\left(\gamma_A^\alpha(i\omega, i\Omega) + \gamma_B^\alpha(i\omega, i\Omega)\tilde{\tau}_3\right)\tilde{\tau}_\alpha \end{aligned} \tag{2.127}$$

where

$$\gamma_A^\alpha \equiv \frac{n_i}{4\pi v_f v_2}\left(\eta_\alpha T_n^a(i\omega)T_n^a(i\omega + i\Omega) + T_n^b(i\omega)T_n^b(i\omega + i\Omega)\right)[|_{n=1} - |_{n=3}] \tag{2.128}$$

$$\gamma_B^\alpha \equiv \frac{n_i}{4\pi v_f v_2}\left(\eta_\alpha T_n^b(i\omega)T_n^a(i\omega + i\Omega) + T_n^a(i\omega)T_n^b(i\omega + i\Omega)\right)[|_{n=1} - |_{n=3}] \tag{2.129}$$

and we define

$$\eta_\alpha \equiv \begin{cases} +1 & \text{for } \alpha = 0, 3 \\ -1 & \text{for } \alpha = 1, 2 \end{cases}. \tag{2.130}$$

Plugging Eq. (2.127) into Eq. (2.126) and defining

$$\tilde{I}^\alpha(i\omega, i\Omega) = \int \frac{d^2p}{\pi} \tilde{\mathcal{G}}(\mathbf{p}, i\omega)\tilde{\tau}_\alpha \tilde{\mathcal{G}}(\mathbf{p}, i\omega + i\Omega)\tilde{\tau}_\alpha \tag{2.131}$$

and

$$\tilde{I}_3^\alpha(i\omega, i\Omega) = \int \frac{d^2p}{\pi} \tilde{\mathcal{G}}(\mathbf{p}, i\omega)\tilde{\tau}_3\tilde{\tau}_\alpha\tilde{\mathcal{G}}(\mathbf{p}, i\omega + i\Omega)\tilde{\tau}_\alpha \tag{2.132}$$

we find that

$$\mathrm{Tr}\,\tilde{\Lambda}^\alpha = \mathrm{Tr}\left[\gamma_A^\alpha \tilde{I}^\alpha(\tilde{\mathbb{1}} + \tilde{\Lambda}^\alpha)\right] + \mathrm{Tr}\left[\gamma_B^\alpha \tilde{I}_3^\alpha(\tilde{\mathbb{1}} + \tilde{\Lambda}^\alpha)\right]. \tag{2.133}$$

Similarly, multiplying Eq. (2.117) by $\tilde{\tau}_3$ and repeating our steps we find that

$$\mathrm{Tr}\left[\tilde{\tau}_3\tilde{\Lambda}^\alpha\right] = \mathrm{Tr}\left[\gamma_B^\alpha \tilde{I}^\alpha(\tilde{\mathbb{1}} + \tilde{\Lambda}^\alpha)\right] + \mathrm{Tr}\left[\gamma_A^\alpha \tilde{I}_3^\alpha(\tilde{\mathbb{1}} + \tilde{\Lambda}^\alpha)\right]. \tag{2.134}$$

At this point it is useful to carry out the momentum integrals in Eqs. (2.131) and (2.132) to obtain an explicit form for $\tilde{I}^\alpha$ and $\tilde{I}_3^\alpha$. Recalling the form of the Matsubara Green's function from Sec. 2.2, noting that $p_1 = \varepsilon_k$ and $p_2 = \Delta_k$, and defining

$$\begin{aligned} f_1 &\equiv i\omega - \Sigma(i\omega) \\ f_2 &\equiv i\omega + i\Omega - \Sigma(i\omega + i\Omega) \end{aligned} \tag{2.135}$$

we can write

$$\tilde{\mathcal{G}}(\mathbf{p}, i\omega) = \frac{f_1\tilde{\mathbb{1}} + p_1\tilde{\tau}_3 + p_2\tilde{\tau}_1}{f_1^2 - p^2}. \tag{2.136}$$

Further, using the definition of η_α from Eq. (2.130) and similarly defining

$$\eta'_\alpha \equiv \begin{cases} +1 & \text{for } \alpha = 0, 1 \\ -1 & \text{for } \alpha = 2, 3 \end{cases} \tag{2.137}$$

we find that

$$\tilde{\tau}_\alpha\tilde{\mathcal{G}}(\mathbf{p}, i\omega + i\Omega)\tilde{\tau}_\alpha = \frac{f_2\tilde{\mathbb{1}} + \eta_\alpha p_1\tilde{\tau}_3 + \eta'_\alpha p_2\tilde{\tau}_1}{f_2^2 - p^2}. \tag{2.138}$$

Thus, plugging Eqs. (2.136) and (2.138) into Eq. (2.131), noting that $p_1 = p\cos\theta$ and $p_2 = p\sin\theta$, and performing the angular integral we find that

$$\tilde{I}^\alpha = I^\alpha\tilde{\mathbb{1}} = \tilde{\mathbb{1}} \int_0^{p_0} 2p \frac{f_1 f_2 + a_\alpha p^2}{(f_1^2 - p^2)(f_2^2 - p^2)} dp \tag{2.139}$$

where

$$a_\alpha \equiv \frac{\eta_\alpha + \eta'_\alpha}{2} = \begin{cases} +1 & \text{for } \alpha = 0 \\ 0 & \text{for } \alpha = 1, 3 \\ -1 & \text{for } \alpha = 2 \end{cases}. \tag{2.140}$$

Factoring the integrand and performing the p-integral yields

$$I^\alpha(i\omega, i\Omega) = \frac{(f_1 + a_\alpha f_2)F(f_2) - (f_2 + a_\alpha f_1)F(f_1)}{f_2^2 - f_1^2} \tag{2.141}$$

where $F(x)$ is defined via Eq. (2.125). Similarly, acting on Eq. (2.132) yields that

$$\tilde{I}_3^\alpha = \tilde{\tau}_3 \int_0^{p_0} 2p \frac{f_1 f_2 + a'_\alpha p^2}{(f_1^2 - p^2)(f_2^2 - p^2)} dp \tag{2.142}$$

where

$$a'_\alpha \equiv \frac{\eta_\alpha - \eta'_\alpha}{2} = \begin{cases} +1 & \text{for } \alpha = 3 \\ 0 & \text{for } \alpha = 0, 2 \\ -1 & \text{for } \alpha = 1 \end{cases} . \tag{2.143}$$

It is easy to see that $a'_\alpha = a_{\alpha+1}$ (where the index addition is defined modulo 4). Hence

$$\begin{aligned} \tilde{I}^\alpha(i\omega, i\Omega) &= I^\alpha \tilde{\mathbb{1}} \\ \tilde{I}_3^\alpha(i\omega, i\Omega) &= I^{\alpha+1} \tilde{\tau}_3 \end{aligned} \tag{2.144}$$

where I^α is given by Eq. (2.141).

Now that $\tilde{I}^\alpha$ and $\tilde{I}_3^\alpha$ have been evaluated, Eqs. (2.133) and (2.134) become a set of coupled equations for $\mathrm{Tr}\,\tilde{\Lambda}^\alpha$ and $\mathrm{Tr}\,[\tilde{\tau}_3 \tilde{\Lambda}^\alpha]$:

$$\begin{aligned} \mathrm{Tr}\,\tilde{\Lambda}^\alpha &= \gamma_A^\alpha I^\alpha (2 + \mathrm{Tr}\,\tilde{\Lambda}^\alpha) + \gamma_B^\alpha I^{\alpha+1} \mathrm{Tr}[\tilde{\tau}_3 \tilde{\Lambda}^\alpha] \\ \mathrm{Tr}[\tilde{\tau}_3 \tilde{\Lambda}^\alpha] &= \gamma_B^\alpha I^\alpha (2 + \mathrm{Tr}\,\tilde{\Lambda}^\alpha) + \gamma_A^\alpha I^{\alpha+1} \mathrm{Tr}[\tilde{\tau}_3 \tilde{\Lambda}^\alpha] \end{aligned} \tag{2.145}$$

Solving simultaneously yields

$$\mathrm{Tr}\left[\tilde{\mathbb{1}} + \tilde{\Lambda}^\alpha\right] = \frac{2}{1 - \gamma_A^\alpha I^\alpha \left(1 + \frac{\gamma_B^\alpha}{\gamma_A^\alpha} \frac{\gamma_B^\alpha I^{\alpha+1}}{1 - \gamma_A^\alpha I^{\alpha+1}}\right)}. \tag{2.146}$$

This is a very useful result since using Eqs. (2.114), (2.119), (2.131), and (2.144) with Eq. (2.112) yields that

$$\overleftrightarrow{\Pi}^{g\ell\alpha}(i\Omega) = \frac{1}{4\pi v_f v_2} \sum_{j=1}^{4} \mathbf{v}_\ell^{(j)} \mathbf{v}_\ell^{(j)} \frac{1}{\beta} \sum_{i\omega} g^2 I^\alpha \mathrm{Tr}\left[\tilde{\mathbb{1}} + \tilde{\Lambda}^\alpha\right]. \tag{2.147}$$

Thus, plugging Eq. (2.146) into Eq. (2.147) and making use of Eq. (2.101) from Sec. 2.7 we find that

$$\overleftrightarrow{\Pi}^{g\ell\alpha} = \Pi^{g\ell\alpha} \overleftrightarrow{\mathbb{1}} \tag{2.148}$$

where

$$\Pi^{g\ell\alpha}(i\Omega) = \frac{v_\ell^2}{\pi v_f v_2} \frac{1}{\beta} \sum_{i\omega} g^2 J^\alpha(i\omega, i\Omega) \tag{2.149}$$

$$J^\alpha \equiv \frac{I^\alpha}{1 - \gamma_A^\alpha I^\alpha \left(1 + \frac{\gamma_B^\alpha}{\gamma_A^\alpha} \frac{\gamma_B^\alpha I^{\alpha+1}}{1 - \gamma_A^\alpha I^{\alpha+1}}\right)} \tag{2.150}$$

and we note that I^α, $I^{\alpha+1}$, γ_A^α, and γ_B^α are all functions of $i\omega$ and $i\Omega$.

Provided the input self-energy is of a proper functional form, $J^\alpha(z, i\Omega)$ will be analytic throughout the complex plane except for two branch cuts at $\mathrm{Im}\, z = 0$ and

$\mathrm{Im}\, z = -\Omega$. Thus, evaluating the Matsubara sum [13] we pick up a contribution from each of the branch cuts of the summand. Consequently, it is useful to consider the form of $J^\alpha(z, i\Omega)$ above and below each of the branch cuts. Upon examination of the frequency dependence of this function via Eqs. (2.150) and (2.128-2.132) it is clear that the internal and external frequencies, $i\omega$ and $i\Omega$, enter only through functional couplets of the form

$$P(i\omega, i\Omega) = A(i\omega)B(i\omega + i\Omega). \tag{2.151}$$

Furthermore, due to the defined analytic structure of Matsubara Green's functions, the functions composing these couplets always have a Matsubara-like analytic structure and satisfy

$$\begin{aligned} A(i\omega \to \omega + i\delta) &= A_{ret}(\omega) \\ A(i\omega \to \omega - i\delta) &= A^*_{ret}(\omega). \end{aligned} \tag{2.152}$$

Consider the form of such a couplet above and below the branch cuts of our summand. Defining

$$\begin{aligned} P_1(\omega, i\Omega) &\equiv P(\omega + i\delta, i\Omega) \\ P_2(\omega, i\Omega) &\equiv P(\omega - i\delta, i\Omega) \\ P_3(\omega, i\Omega) &\equiv P(\omega - i\Omega + i\delta, i\Omega) \\ P_4(\omega, i\Omega) &\equiv P(\omega - i\Omega - i\delta, i\Omega) \end{aligned} \tag{2.153}$$

and continuing $i\Omega \to \Omega + i\delta$ we see that

$$\begin{aligned} P_3(\omega, \Omega) &= P_2(\omega - \Omega, \Omega) \\ P_4(\omega, \Omega) &= P_1^*(\omega - \Omega, \Omega). \end{aligned} \tag{2.154}$$

Since J^α is composed of such couplets, if we similarly define

$$\begin{aligned} J_1^\alpha(\omega, i\Omega) &\equiv J^\alpha(\omega + i\delta, i\Omega) \\ J_2^\alpha(\omega, i\Omega) &\equiv J^\alpha(\omega - i\delta, i\Omega) \\ J_3^\alpha(\omega, i\Omega) &\equiv J^\alpha(\omega - i\Omega + i\delta, i\Omega) \\ J_4^\alpha(\omega, i\Omega) &\equiv J^\alpha(\omega - i\Omega - i\delta, i\Omega) \end{aligned} \tag{2.155}$$

it follows that

$$\begin{aligned} J_3^\alpha(\omega, \Omega) &= J_2^\alpha(\omega - \Omega, \Omega) \\ J_4^\alpha(\omega, \Omega) &= J_1^{\alpha *}(\omega - \Omega, \Omega). \end{aligned} \tag{2.156}$$

These relations will be very helpful in what follows. Now we can proceed with the Matsubara sum. As in Sec. 2.7, it is best to treat the frequency-independent coupling and frequency-dependent coupling cases separately.

For $g = \{e, s\}$ (frequency-independent coupling), the sum is straightforward. Adding the contributions of the two branch cuts and using the definitions in Eq. (2.155)

yields

$$\Pi^{g\ell\alpha}(i\Omega) = i\frac{g^2}{2\pi^2}\frac{v_\ell^2}{v_f v_2}\int_{-\infty}^{\infty} d\omega\, n_F(\omega)\Big[J_1^\alpha(\omega, i\Omega) - J_2^\alpha(\omega, i\Omega) + J_3^\alpha(\omega, i\Omega) - J_4^\alpha(\omega, i\Omega)\Big] \tag{2.157}$$

where $n_F(\omega)$ is the Fermi function.

For $g = \omega + \Omega/2$ (frequency-dependent coupling), noting the technical issues discussed in the analogous stage of the bare bubble calculation (see Sec. 2.7), we can proceed as above. Adding the contributions of the two branch cuts and using Eq. (2.155) we find that

$$\begin{aligned}\Pi^{g\ell\alpha}(i\Omega) = i\frac{1}{2\pi^2}\frac{v_\ell^2}{v_f v_2}\int_{-\infty}^{\infty} d\omega\, n_F(\omega) \\ \times\Big[\Big(\omega + \frac{i\Omega}{2}\Big)^2 \left(J_1^\alpha(\omega, i\Omega) - J_2^\alpha(\omega, i\Omega)\right) + \Big(\omega - \frac{i\Omega}{2}\Big)^2 \left(J_3^\alpha(\omega, i\Omega) - J_4^\alpha(\omega, i\Omega)\right)\Big].\end{aligned} \tag{2.158}$$

In either case, continuing $i\Omega \to \Omega + i\delta$, making use of the relations in Eq. (2.156), and shifting $\omega \to \omega + \Omega$ in the last two terms, we obtain the retarded polarization function

$$\begin{aligned}\Pi_{ret}^{g\ell\alpha}(\Omega) = i\frac{1}{2\pi^2}\frac{v_\ell^2}{v_f v_2}\int_{-\infty}^{\infty} d\omega\, g^2 \\ \times\Big[n_F(\omega)(J_1^\alpha(\omega,\Omega) - J_2^\alpha(\omega,\Omega)) - \; n_F(\omega+\Omega)(J_1^{\alpha *}(\omega,\Omega) - J_2^\alpha(\omega,\Omega))\Big]\end{aligned} \tag{2.159}$$

which is valid for all three coupling parameters. Taking the imaginary part, noting that $\mathrm{Re}[z] = \mathrm{Re}[z^*]$, and expanding J_1^α and J_2^α yields

$$\begin{aligned}\mathrm{Im}\,\Pi_{ret}^{g\ell\alpha}(\Omega) = \frac{1}{2\pi^2}\frac{v_\ell^2}{v_f v_2}\int_{-\infty}^{\infty} d\omega\, g^2 \left(n_F(\omega+\Omega) - n_F(\omega)\right) \\ \times\mathrm{Re}\left[\frac{I_2^\alpha}{1 - \gamma_{A2}^\alpha I_2^\alpha\left(1 + \frac{\gamma_{B2}^\alpha}{\gamma_{A2}^\alpha}\frac{\gamma_{B2}^\alpha I_2^{\alpha+1}}{1-\gamma_{A2}^\alpha I_2^{\alpha+1}}\right)} - \frac{I_1^\alpha}{1 - \gamma_{A1}^\alpha I_1^\alpha\left(1 + \frac{\gamma_{B1}^\alpha}{\gamma_{A1}^\alpha}\frac{\gamma_{B1}^\alpha I_1^{\alpha+1}}{1-\gamma_{A1}^\alpha I_1^{\alpha+1}}\right)}\right]\end{aligned} \tag{2.160}$$

where

$$I_1^\alpha(\omega,\Omega) = \frac{(f_1 + a_\alpha f_2)F(f_2) - (f_2 + a_\alpha f_1)F(f_1)}{f_2^2 - f_1^2} \tag{2.161}$$

$$I_2^\alpha(\omega,\Omega) = \frac{(f_1^* + a_\alpha f_2)F(f_2) - (f_2 + a_\alpha f_1^*)F(f_1^*)}{f_2^2 - {f_1^*}^2} \tag{2.162}$$

$$\begin{aligned} f_1 &= \omega - \Sigma_{ret}(\omega) \\ f_2 &= \omega + \Omega - \Sigma_{ret}(\omega+\Omega). \end{aligned} \tag{2.163}$$

$$\gamma_{A1}^{\alpha} \equiv \frac{n_i}{4\pi v_f v_2}\left(\eta_\alpha T_n^a(\omega)T_n^a(\omega+\Omega) + T_n^b(\omega)T_n^b(\omega+\Omega)\right)[|_{n=1} - |_{n=3}] \tag{2.164}$$

$$\gamma_{A2}^{\alpha} \equiv \frac{n_i}{4\pi v_f v_2}\left(\eta_\alpha T_n^a(\omega)^* T_n^a(\omega+\Omega) + T_n^b(\omega)^* T_n^b(\omega+\Omega)\right)[|_{n=1} - |_{n=3}] \tag{2.165}$$

$$\gamma_{B1}^{\alpha} \equiv \frac{n_i}{4\pi v_f v_2}\left(\eta_\alpha T_n^b(\omega)T_n^a(\omega+\Omega) + T_n^a(\omega)T_n^b(\omega+\Omega)\right)[|_{n=1} - |_{n=3}] \tag{2.166}$$

$$\gamma_{B2}^{\alpha} \equiv \frac{n_i}{4\pi v_f v_2}\left(\eta_\alpha T_n^b(\omega)^* T_n^a(\omega+\Omega) + T_n^a(\omega)^* T_n^b(\omega+\Omega)\right)[|_{n=1} - |_{n=3}] \tag{2.167}$$

$$T_n^a(\omega) = \left(\frac{\underline{V}}{1 - F'(\omega)^2\underline{V}^2}\right)_{n1} \tag{2.168}$$

$$T_n^b(\omega) = \left(\frac{-F'(\omega)\underline{V}^2}{1 - F'(\omega)^2\underline{V}^2}\right)_{n1} \tag{2.169}$$

$$F'(\omega) = \frac{F(\omega - \Sigma_{ret}(\omega))}{4\pi v_f v_2} \tag{2.170}$$

and $F(x)$ is defined in Eq. (2.125). The above equations define the imaginary part of the generalized retarded polarization function including ladder corrections to the vertex. By specifying different input parameters we can use it to obtain the electrical, thermal, and spin conductivity.

2.9 Appendix C: Numerical Analysis of Universal Limit Vertex Corrections

In Secs. 2.3.3, 2.4.3, and 2.5.3, the vertex correction factors for the universal limit electrical and thermal/spin conductivities were found to be

$$\beta_{vc} = \frac{1 + 2\left(\gamma_{A2}^{(0)} - \gamma_{A1}^{(0)} + \frac{\gamma_{B1}^{(0)\,2}}{1-\gamma_{A1}^{(0)}}\right)\ln\frac{p_0}{\Gamma_0}\left(\ln\frac{p_0}{\Gamma_0} - 1\right)}{\left(1 - 2\gamma_{A2}^{(0)}\ln\frac{p_0}{\Gamma_0}\right)\left(1 - 2\left(\gamma_{A1}^{(0)} - \frac{\gamma_{B1}^{(0)\,2}}{1-\gamma_{A1}^{(0)}}\right)\left(\ln\frac{p_0}{\Gamma_0} - 1\right)\right)} \tag{2.171}$$

$$\beta_{vc}^{T,s} = \frac{\frac{1}{2}}{1 - \gamma_{A2}^{(0)}} + \frac{\frac{1}{2}}{1 + \gamma_{A1}^{(0)}\left(1 + \frac{\gamma_{B1}^{(0)}}{\gamma_{A1}^{(0)}}\frac{\gamma_{B1}^{(0)}\left(2\ln\frac{p_0}{\Gamma_0} - 2\right)}{1-\gamma_{A1}^{(0)}\left(2\ln\frac{p_0}{\Gamma_0} - 2\right)}\right)} \tag{2.172}$$

where the γ's and their constituent functions are given in Eqs. (2.29-2.32). Here we shall numerically compute both factors as a function of impurity density and scattering potential. To facilitate the computation, it is convenient to make all quantities dimensionless by expressing energies in units of p_0 and lengths in units of $2a$. This choice of units sets the frequently encountered constant, $4\pi v_f v_2$, equal to 1. For a particular set of input parameters, the computation is done in two steps. First, solve

self-consistently for the zero-frequency scattering rate, Γ_0, via

$$\Sigma_{ret}(\omega) = n_i T^b_{11}(\omega) \tag{2.173}$$

which (in the universal limit with our choice of units) reduces to

$$2n_i \ln \frac{1}{\Gamma_0} \left(\frac{\underline{V}^2}{1 + \left(2\Gamma_0 \ln \frac{1}{\Gamma_0}\right)^2 \underline{V}^2} \right)_{1,1} = 1. \tag{2.174}$$

Then given Γ_0, plug into Eqs. (2.171) and (2.172) to obtain the vertex corrections.

The result will depend on the set of four input parameters which determine the impurity density and scattering potential, $\{n_i, V_1, V_2, V_3\}$. In our units, $n_i = 4z$ where z is the substitutional fraction of impurities. Furthermore, it is convenient to parameterize the scattering potential via

$$V_1 = V_{scale} \tan\left(\frac{\pi}{2} d\right) \qquad R_2 = \frac{V_2}{V_1} \qquad R_3 = \frac{V_3}{V_1} \tag{2.175}$$

where V_{scale} is a dimensionless constant and d ranges from 0 to 1. Hence, the scattering anisotropy is given by R_2 and R_3 while the scattering strength is given by d. Note that while is tempting to think of $\frac{\pi}{2}d$ as some sort of scattering phase shift, to do so would be stretching an analogy beyond its realm of usefulness. The above is merely a helpful parameterization, the aim of which is to allow us to go smoothly from the Born limit to the unitary limit as d varies from 0 to 1. For our purposes, these limits are determined by the denominator in Eq. (2.174):

$$\left(2\Gamma_0 \ln \frac{1}{\Gamma_0}\right) V_1 \ll 1 \quad \rightarrow \quad \text{Born limit}$$
$$\left(2\Gamma_0 \ln \frac{1}{\Gamma_0}\right) V_1 \gg 1 \quad \rightarrow \quad \text{Unitary limit}$$

Thus, for a particular range of z, we shall set V_{scale} to a value that allows us to evenly sample the transition from one limit to the other. In the end, these manipulations yield a new set of four dimensionless input parameters, $\{z, d, R_2, R_3\}$.

The electrical and thermal/spin vertex corrections obtained for a typical set of input parameters, via the procedure described above, are plotted in Fig. 2-5. Here we have assumed that $V(\mathbf{k})$ falls off slowly with increasing $\mathbf{k}$ ($R_2 = 0.9$, $R_3 = 0.8$) and have plotted the vertex corrections versus impurity fraction ($z = 0.01\% \rightarrow 1\%$) for seven scattering strengths from Born ($d = 0.001$) to unitary ($d = 0.999$). Note that the electrical correction, $\beta_{vc} - 1$, can be quite significant while the thermal/spin correction, $\beta^{T,s}_{vc} - 1$, is much smaller and vanishes as $z \rightarrow 0$. The difference between the two cases is seen most clearly in Fig. 2-6 where, for $d = 0.001, 0.5, 0.999$, we have replotted the electrical and thermal/spin correction factors on the same scale. On the scale of $\beta_{vc} - 1$, it is difficult to distinguish $\beta^{T,s}_{vc} - 1$ from the x-axis. Thus, we see that for all scattering strengths, the thermal/spin vertex correction is negligible

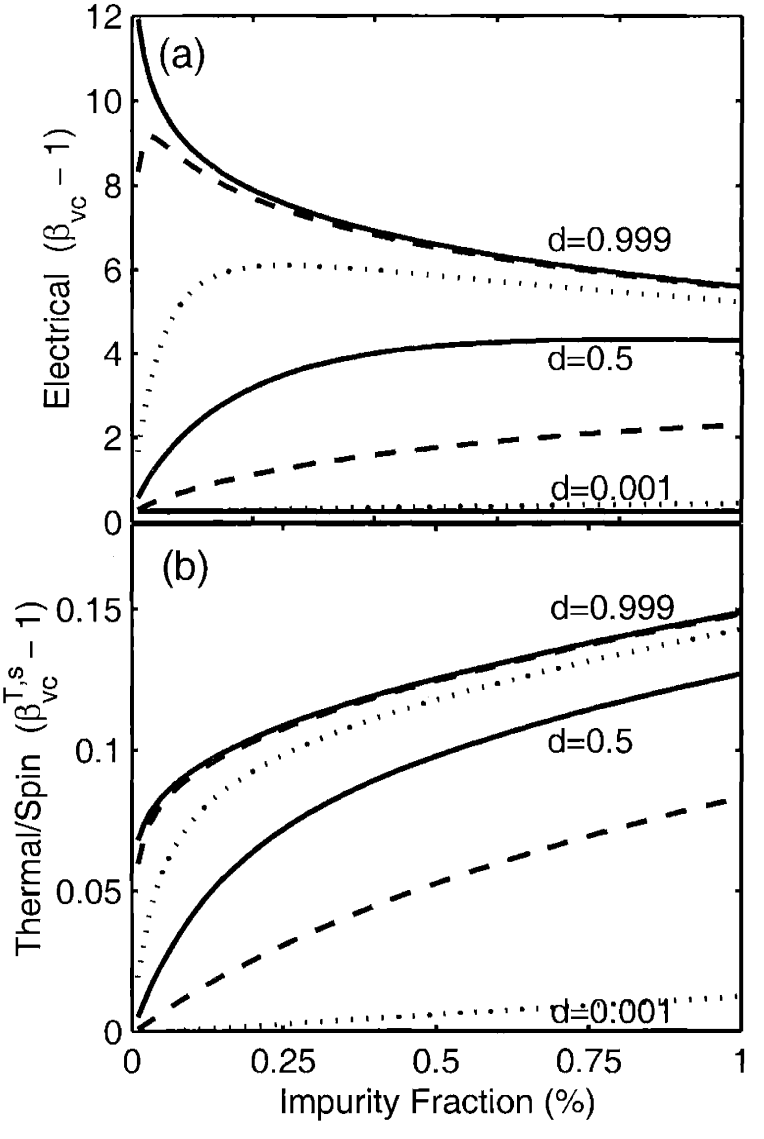

Figure 2-5: Numerically calculated (a) electrical and (b) thermal/spin vertex corrections plotted as a function of impurity fraction ($z = 0.01\% \rightarrow 1\%$) for scattering strengths parameterized via (from bottom to top) $d = \{0.001$ (Born), $0.1, 0.3, 0.5, 0.7, 0.9,\ 0.999$ (unitary)$\}$. In all cases we have set $V_{scale} = 20$ and assumed that $V(\mathbf{k})$ falls off slowly with $|\mathbf{k}|$ ($R_2 = 0.9$, $R_3 = 0.8$).

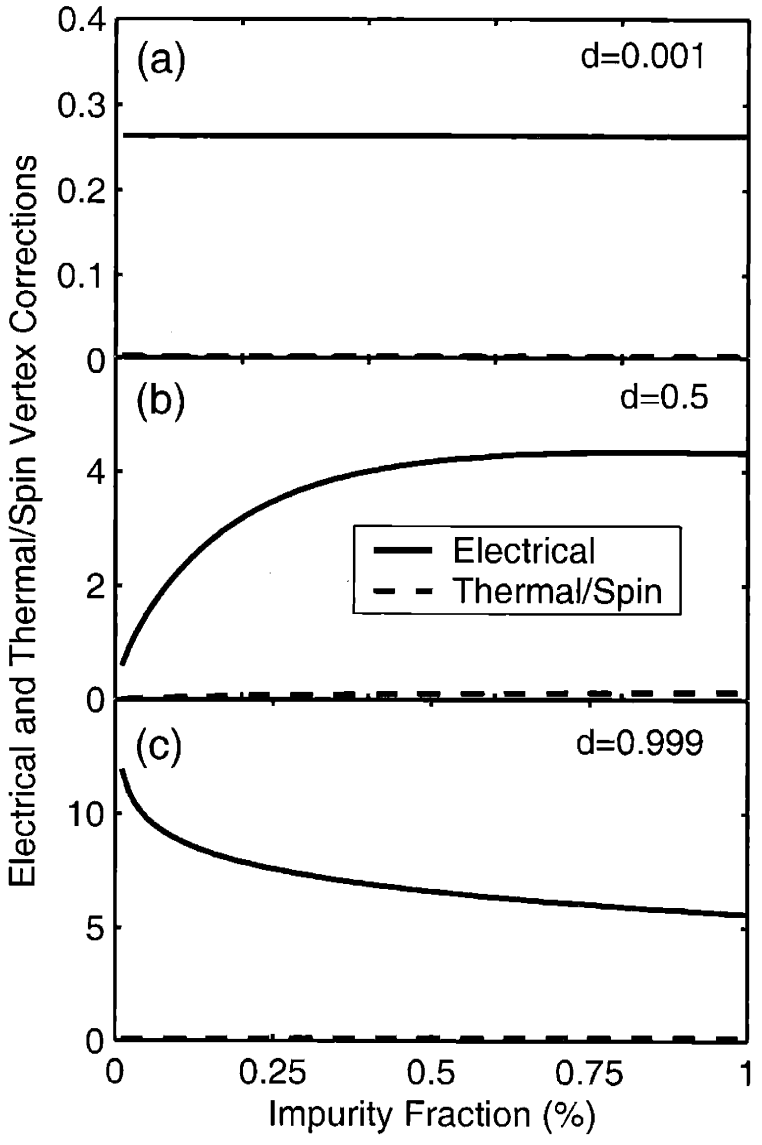

Figure 2-6: Direct comparison of electrical ($\beta_{vc}-1$) and thermal/spin ($\beta_{vc}^{T,s}-1$) vertex corrections for (a) $d = 0.001$, (b) $d = 0.5$, and (c) $d = 0.999$. Note that in all cases, the thermal/spin correction is negligible on the scale of of the electrical correction.

compared to the electrical vertex correction.

Additional insight is gained through consideration of the intermediate stages of the calculation which reveal that

$$\gamma_{A1}^{(0)}, \gamma_{A2}^{(0)}, \gamma_{B1}^{(0)} \lesssim \mathcal{O}\left(\frac{1}{\ln \frac{p_0}{\Gamma_0}}\right). \tag{2.176}$$

In the Born limit, $1/\ln(p_0/\Gamma_0) \sim z$, which can truly be neglected for the small impurity fractions of interest. In the unitary limit, $1/\ln(p_0/\Gamma_0) \sim 1/\ln(1/z)$, which vanishes much more slowly but is still small compared to terms of order unity. Thus, since we can treat the γ's as small quantities, the (mathematical) difference between the electrical and thermal/spin cases is due to the manner in which the γ's enter Eqs. (2.171) and (2.172). The γ's enter β_{vc} within order unity combinations of the form $\gamma \ln(p_0/\Gamma_0)$ (and for some parameter values even $\gamma \ln^2(p_0/\Gamma_0)$) which cannot be neglected. In contrast, the γ's enter $\beta_{vc}^{T,s}$ on their own (that is, in direct competition with terms of order unity) and can therefore be neglected for small z. Hence we say that electrical vertex corrections contribute even to zeroth order in the impurity density while thermal/spin vertex corrections do not.

Chapter 3

Microwave Conductivity due to Extended Linear Defect Scattering

And those bright Twins were side by side;
And there, by fresh hopes beautified ...

William Wordsworth

3.1 Introduction

Of the numerous phases of the high-T_c cuprate phase diagram, the low temperature superconducting phase appears to be the least mysterious. All indications point to an order parameter of $d_{x^2-y^2}$ symmetry and well defined quasiparticle excitations above the condensate [8, 10]. An excellent probe of the low energy excitations of this d-wave superconductor is the measurement of low temperature microwave conductivity. Experimentally, the real part of the microwave conductivity, $\sigma(\Omega, T)$, can be extracted from microwave measurements of complex surface impedance $Z_s(\Omega, T)$ [25, 28, 43, 44, 45]. Theoretically, at low temperatures, it is determined by calculating the linear response of a d-wave superconductor in the presence of scattering due to static disorder [17, 18, 46, 47, 35, 36, 48, 49]. (Low temperature is defined as low enough such that all inelastic scattering [50] is negligible.) The mystery is that, in this least mysterious of phases, the simplest theoretical models do not agree with experiment [51].

The microwave electrical conductivity of detwinned, high-purity, slightly over-doped $YBa_2Cu_3O_{6.993}$ was measured by Hosseini *et al.* [25]. Data was taken at five frequencies between 1 and 75 GHz for temperatures from 1 to 95 K. Below 20 K, in the regime dominated by elastic scattering, they find that the microwave conductivity has an approximately linear temperature dependence and a near-Drude frequency dependence. Fitting the data to a Drude form, they extract a spectral weight that is linear in temperature (in agreement with the measured superfluid density) and an effective scattering rate, $1/\tau$, that is approximately constant over the entire low temperature regime (1 to 20 K).

From the extracted value of the scattering rate ($5.6 \times 10^{10}\,\mathrm{s}^{-1}$) and the frequency and temperature range of the experiments, it can be seen that these measurements

correspond to the parameter regime $\Omega, 1/\tau \ll T \ll \Delta_0$ where Δ_0 is the gap maximum. For this parameter regime, the theoretical picture is as follows. A d-wave superconductor is characterized by an order parameter that vanishes linearly at each of four gap nodes. For $T \ll \Delta_0$, transport is dominated by low energy quasiparticle excitations generated in the vicinity of the nodes. For $1/\tau \ll T$, the quasiparticles are generated thermally, rather than by the presence of disorder [16]. (Hence, in what follows, we refer to this as the *thermal* regime.) The most straightforward model for such a system is one in which thermally generated nodal quasiparticles are scattered due to the presence of point defects such as impurities. Performing an impurity average and using a Kubo formula approach within the self-consistent t-matrix approximation, the self-energy and electrical conductivity have previously been calculated [17, 18, 46, 51].

Surprisingly, the predictions of such calculations do not agree with the experimental results. The trouble comes in attempting to reproduce the constant scattering rate extracted from experiment. For a d-wave superconductor in the thermal regime, the anisotropic Dirac excitation spectrum yields a quasiparticle density of states that is linear in energy. This strong energy dependence of the density of states is then directly reflected in the results of the impurity t-matrix calculations. Such calculations yield $1/\tau \sim T$ and $\sigma \sim$ const in the Born limit and $1/\tau \sim 1/T$ and $\sigma \sim T^2$ in the unitary limit. More generally, over the full range of scattering strengths, it has been shown that simple models [52] of point defect (impurity) scattering are inconsistent with experiment [51].

Despite this, we certainly expect the presence of impurities to make a significant contribution to the total scattering. However, the observed disagreement between theory and experiment suggests that an additional scattering mechanism may also be important. In what follows, we propose that this additional mechanism is scattering from extended linear defects. Our motivation for doing so is twofold. First of all, we note that scattering from a series of parallel lines differs from point defect scattering in an important way. While point defects scatter in all directions, line defects only scatter in the direction normal to their orientation. Hence, whereas point defect scattering samples the full quasiparticle density of states, line defect scattering restricts final states to those for which there is no change in the parallel component of momentum. Therefore, the line defect scattering rate need not inherit the strong energy dependence of the density of states and is thereby capable of exhibiting the less energy dependent form required to agree with experiment. Secondly, we note that upon growth, YBCO crystals are full of "lines", twin boundary lines. Although the twin boundaries are subsequently removed via a detwinning procedure, remnants of their structure may be left behind in the form of extended linear defects. Since lines are prevalent in this material and line defects tend to exhibit features of the measured behavior, it is logical that we should examine the contribution made by line defect scattering [53]. For simplicity, we consider herein a system where extended linear defects provide the sole scattering mechanism, leaving the analysis of a system with both line defects and point defects for future study.

In Sec. 3.2, we discuss twinning in YBCO and the nature of the detwinning process. In light of the observed twinning structure and guided by the notion that the

detwinning process leaves behind remnants in the form of line defects, we develop, in Sec. 3.3, a model for quasiparticle scattering from extended linear defects in a d-wave superconductor. In Secs. 3.4 and 3.5, we calculate the resulting self-energy and microwave conductivity. For parameter values within the thermal regime, we obtain analytical results which are compared to experiment in Sec. 3.6.1. Numerical results, including deviations from our analytical expressions and valid beyond the thermal regime, are presented in Sec. 3.6.2. Conclusions are discussed in Sec. 3.7 where we provide physical motivation for our calculated results and discuss the implications of our findings.

3.2 Twin Boundaries in YBCO

Twinning occurs naturally during the growth of oxygen deficient $YBa_2Cu_3O_{7-\delta}$ [54]. At full oxygenation ($\delta = 0$), the crystal structure is orthorhombic at room temperature with lattice parameters $a = 3.227$ Å and $b = 3.8872$ Å, the latter being the orientation parallel to the CuO chain layer [55]. For nonzero δ, oxygen vacancies are present in the CuO layer and the remaining oxygen can disorder onto sites perpendicular to the CuO chains, thereby reducing the orthorhombic distortion [56]. However, occupation of these off-chain sites is inhibited by repulsive interactions with oxygen located at on-chain sites. The formation of twin boundaries, which are abrupt boundaries between crystal domains with CuO chain orientations that differ by 90°, are the energetic compromise between decreasing the orthorhombicity and maintaining the CuO chain ordering.

The overdoped $YBa_2Cu_3O_{6.993}$ crystal studied by Hosseini *et al.* was prepared by annealing an as-grown crystal at 350°C for 50 days in flowing high purity oxygen [25]. Detwinning was accomplished by incrementally applying uniaxial stress in the $\widehat{ab}$ plane with the sample temperature fixed at 250°C in flowing high purity oxygen. Progress was monitored by viewing the sample through a microscope objective with a polarizer oriented at 45° with respect to the crystalline axes. Domains with differing CuO chain orientations were then visible and the elimination of twin boundaries could be verified. The complete detwinning of a 1 mm^2 crystal can typically be accomplished within one day.

An example of an as-grown twinned $YBa_2Cu_3O_{7-\delta}$ sample and a detwinned sample of $YBa_2Cu_3O_{6.993}$ are shown in Fig. 3-1. This picture was obtained by shining polarized white light onto the crystals at 45° with respect to the crystalline axes and then observing through a polarizer oriented parallel to the incident light. In the as-grown sample, the two different CuO chain orientations are visible as a difference in grayscale. The lines oriented at ±45° which separate these regions are the twin boundaries. Darkened areas denote regions of highly concentrated twin boundaries. In the detwinned sample, there is a single orientation for all the CuO chains. Here, the $\hat{a}$ axis is parallel to the horizontal since this is the direction along which the uniaxial stress was applied. Note the absence of any visible twin boundaries in the detwinned crystal.

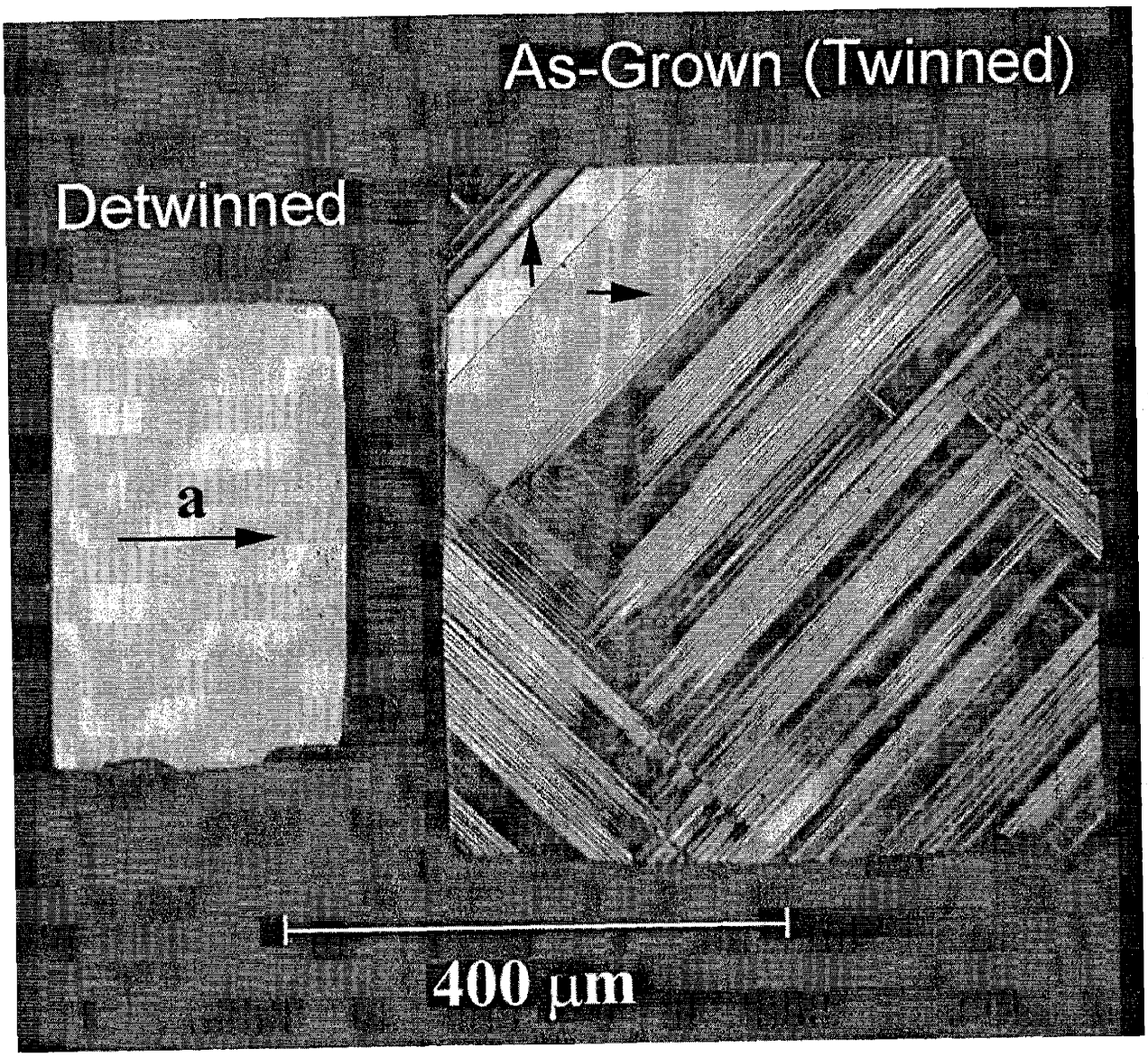

Figure 3-1: Photograph of as-grown (twinned) and detwinned single crystals of YBCO as viewed through an optical microscope under polarized light. In the as-grown sample, two different CuO chain orientations, visible as a difference in grayscale, are separated by twin boundaries oriented at $\pm 45^{\circ}$ to the horizontal. (Arrows highlight the two CuO chain orientations.) Darkened areas are regions of highly concentrated twin boundaries. In the detwinned sample, twin boundaries are no longer visible and the $\hat{a}$ axis is parallel to the horizontal throughout the crystal. (Photograph courtesy of R. Harris [54].)

3.3 Extended Linear Defect Scattering

Since line defect scattering has the appealing property that it does not sample the full quasiparticle density of states, we consider a model in which d-wave quasiparticles scatter from extended linear defects. In particular, we imagine that the line defects are arranged in a manner reflective of the twin boundary structure exhibited in YBCO prior to detwinning. That is, we consider domains of line defects within which the lines are parallel, oriented at either $+45°$ or $-45°$ to the crystal axes, and separated by distances on the order of microns. Our picture is that in the process of detwinning, neighboring twin boundaries are made to annihilate in order to eliminate regions in which the CuO chain orientation is disfavored by the applied uniaxial stress. Although this procedure is effective in removing the twin boundaries, it can leave behind defects along the lines at which the twin boundaries annihilate. While there may be multiple ways in which this can come to be, one example of a detwinning scenario through which line defects could be left behind is the following.

The twin boundaries in as-grown YBCO are $\pm 45°$ lines which separate regions with horizontal CuO chains from regions with vertical CuO chains. Geometry dictates that the distance between oxygen sites on opposite sides of such a line is smaller than the normal oxygen-oxygen separation in the bulk. As a result, it is energetically advantageous for oxygen vacancies, which must be present in the CuO layer of doped YBCO, to be concentrated along twin boundary lines. Upon detwinning, a uniaxial stress is applied to favor one CuO chain orientation and force neighboring twin boundaries to approach each other and annihilate. As the twin boundaries move, the vacancies move with them until neighboring boundaries annihilate, leaving behind lines of oxygen vacancies. The resulting potential, felt by quasiparticles in the CuO_2 plane, is that of a collection of extended linear defects arranged in a pattern that reflects the original twinning structure. Note that this is just one example of a process that could yield line defects. As we shall see, however, our results will suggest that something similar to this is going on.

Consider a single domain in which all line defects are aligned at $-45°$ to the horizontal axis. This situation is depicted schematically in Fig. 3-2. We denote the directions parallel and perpendicular to the defect lines as $\hat{\mathbf{r}}_{\|}$ and $\hat{\mathbf{r}}_{\perp}$ respectively. Now consider the effect of scattering off of such extended linear defects in 2d. Since all the lines are normal to the $r_{\perp}$ direction, they act as potential sources, $V(r_{\perp})$, that depend only on the $r_{\perp}$ coordinate. Fourier transforming, it is clear that such scattering events conserve the parallel component of momentum, $p_{\|}$, and are therefore one-dimensional in nature. Furthermore, since the distribution of line defects is random in the $r_{\perp}$ direction, this problem corresponds to an effective one-dimensional "impurity" problem (along $\hat{\mathbf{r}}_{\perp}$) in which $p_{\|}$ is conserved but not relevant to the scattering. Performing a 1d disorder average, properties of the resulting system can be calculated in terms of the 1d line defect density, n_T, and the 1d momentum-space line defect scattering potential, $V(p_{\perp} - k_{\perp})$.

Now consider the effect of this sort of one-dimensional scattering on the physics of a d-wave superconductor. We model a generic d-wave superconductor as a system with the Brillouin zone of a 2d square lattice and an order parameter of $d_{x^2-y^2}$ symmetry

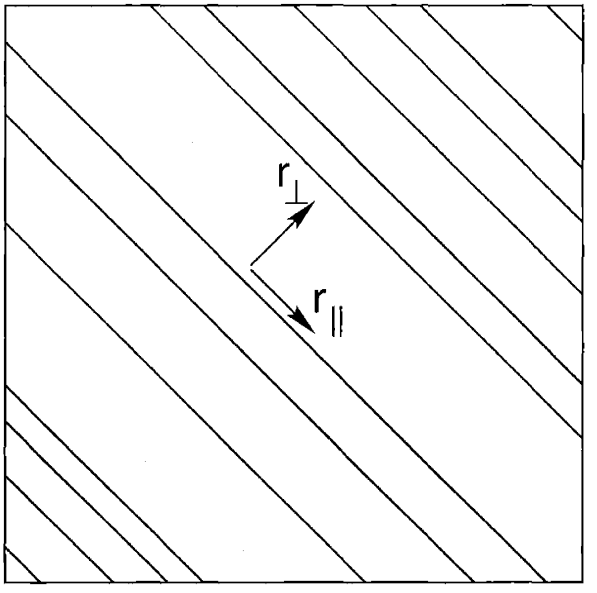

Figure 3-2: Schematic depiction of a single domain of extended linear defects. The line defects are aligned at $-45°$ to the horizontal and spaced randomly in the $\hat{\mathbf{r}}_\perp$ direction with a 1d density n_T.

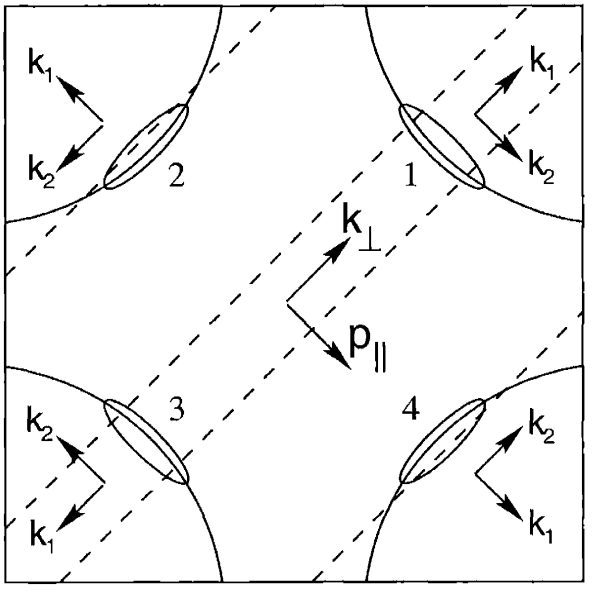

Figure 3-3: Schematic depiction of the Brillouin zone of a d-wave superconductor in the presence of line defect scattering. The elliptical regions, labeled 1 through 4, denote (at a very exaggerated scale) four pockets of thermally generated nodal quasiparticles. In addition to the global momentum directions, $\hat{\mathbf{p}}_{||}$ and $\hat{\mathbf{k}}_\perp$, defined parallel and perpendicular to the defect lines, we have also defined local momentum directions, $\hat{\mathbf{k}}_1$ and $\hat{\mathbf{k}}_2$, about each of the four nodes. The dashed lines denote scattering paths that conserve the parallel component of momentum.

that vanishes at each of four nodal points on the Fermi surface. In the vicinity of each of these nodal points, the electronic dispersion, ϵ_k, varies linearly across the Fermi surface and the order parameter, Δ_k, varies linearly along the Fermi surface. As a result, near each of the gap nodes, the Bogoliubov quasiparticle excitation spectrum takes the anisotropic Dirac form $E_k = \sqrt{\epsilon_k^2 + \Delta_k^2} = \sqrt{v_f^2 k_1^2 + v_2^2 k_2^2}$ where the degree of anisotropy is expressed by the ratio of the Fermi velocity, v_f, to the gap velocity (slope), v_2, and the momenta, k_1 and k_2, are defined locally at each node such that in all cases, $\epsilon_k = v_f k_1$ and $\Delta_k = v_2 k_2$. Hence, excitations are free at the nodal points and, at temperatures much less than the gap maximum, quasiparticles are thermally generated within small regions about the gap nodes. The situation is depicted in Fig. 3-3 where the elliptical regions (labeled 1 through 4) denote four pockets of thermally generated quasiparticles. In the case of point defect (impurity) scattering, quasiparticles could be scattered either within the nodal pocket from which they originated (intra-node) or from one node to another (inter-node) [57]. This is so because point defect scattering events do not conserve either component of momentum. However, due to the 1d nature of extended linear defect scattering, scattering events conserve the parallel component of momentum, $p_{||}$. Therefore, in the presence of line defect scattering, quasiparticles can only be scattered along lines parallel to the $k_\perp$ axis in momentum space. Four such (dashed) lines are shown in Fig. 3-3. From the figure it is clear that the condition of $p_{||}$ conservation means that we have two different kinds of nodes. For the odd nodes (1 and 3), quasiparticles can be scattered either intra-node ($1 \rightarrow 1$ or $3 \rightarrow 3$) or to their opposite-node ($1 \rightarrow 3$ or $3 \rightarrow 1$). Forbidden by $p_{||}$ conservation is the adjacent-node scattering (i.e. $1 \rightarrow 2$) that would be allowed for the point defect case. But for the even nodes (2 and 4), quasiparticles can only be scattered intra-node ($2 \rightarrow 2$ or $4 \rightarrow 4$). Here both adjacent-node and opposite-node scattering are forbidden by $p_{||}$ conservation. Due to the clear difference between odd nodes and even nodes in the presence of line defect scattering, it will be important in the calculations that follow to always treat the odd node and even node cases separately. Furthermore, we should note that the designation of odd or even to a particular node is a direct result of our choice to consider a domain in which the line defects are aligned at $-45°$ to the horizontal. To consider the other type of domain, where the line defects are aligned at $+45°$ to the horizontal, we need only swap odd for even in all designations. With this model of thermally excited pockets of quasiparticles scattered by parallel randomly-spaced defect lines in mind, we proceed to calculate the resulting self-energy and microwave conductivity.

3.4 Self-Energy Calculation

For a superconductor at finite temperature, our calculations will employ Matsubara Green's functions expressed in the 2×2 matrix Nambu formalism. The bare Green's function takes the form

$$\tilde{\mathcal{G}}_0(\mathbf{k}, i\omega) = \frac{1}{(i\omega)^2 - E_k^2} \begin{pmatrix} i\omega + \epsilon_k & \Delta_k \\ \Delta_k & i\omega - \epsilon_k \end{pmatrix} \tag{3.1}$$

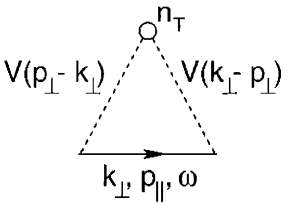

Figure 3-4: Self-energy within Born approximation.

where the tilde denotes a Nambu-space matrix and $i\omega = i(2n+1)\pi k_B T$ is a fermionic Matsubara frequency. In the presence of scattering, the Green's function is dressed via Dyson's equation

$$\tilde{\mathcal{G}}(\mathbf{k}, i\omega)^{-1} = \tilde{\mathcal{G}}_0(\mathbf{k}, i\omega)^{-1} - \tilde{\Sigma}(\mathbf{k}, i\omega) \tag{3.2}$$

where

$$\tilde{\Sigma}(\mathbf{k}, i\omega) = \tilde{\Sigma}(k_\perp, k_\parallel, i\omega) = \begin{pmatrix} \Sigma_{11} & \Sigma_{12} \\ \Sigma_{21} & \Sigma_{22} \end{pmatrix} \tag{3.3}$$

is the Matsubara self-energy.

In the Born approximation, this self-energy matrix can be calculated by evaluating the diagram in Fig. 3-4 to obtain

$$\tilde{\Sigma}(p_\perp, p_\parallel, i\omega) = n_T \sum_{k_\perp} |V(p_\perp - k_\perp)|^2 \, \tilde{\tau}_3 \tilde{\mathcal{G}}(k_\perp, p_\parallel, i\omega) \tilde{\tau}_3 \tag{3.4}$$

where $V(p_\perp - k_\perp)$ is the line defect scattering potential, n_T is the line defect density, and the $\tilde{\tau}_i$ are Pauli matrices in Nambu-space. Due to the 1d nature of the line defect scattering, $p_\parallel$ is conserved and we have integrated only over $k_\perp$. Since quasiparticles reside only in the vicinity of the four gap nodes, each momentum can be expressed by a node index, j, and a local momentum, (k_1, k_2), defined about node j. Furthermore, it is useful to scale out the anisotropy of the excitation spectrum by defining local scaled momenta, $k_1' \equiv v_f k_1$ and $k_2' \equiv v_2 k_2$, such that at each node $\epsilon_k = k_1'$, $\Delta_k = k_2'$, and $E_k = \sqrt{k_1'^2 + k_2'^2}$. For convenience, we drop the primes in all that follows and take all locally defined momenta to be scaled momenta. Making use of these locally defined variables, we can replace

$$\sum_{k_\perp} \to \sum_j{}' \int_{-\infty}^{\infty} \frac{dk}{2\pi v} \tag{3.5}$$

where the sum over node index j is restricted to include only nodes that are crossed by the $k_\perp$ integration path, k is the local scaled momentum component parallel to $k_\perp$ (k_1 or k_2), and v is the corresponding velocity (v_f or v_2). Similarly, we can replace the initial momentum, ($p_\perp$,$p_\parallel$), with an initial node index and an initial local scaled momentum, (p_1,p_2). As is clear from the dashed integration paths shown in Fig. 3-3, the details of these replacements depend on the type of node about which the quasiparticles reside prior to scattering. For quasiparticles initially near odd nodes (1

or 3), the node index sum yields both an intra-node scattering term and an opposite-node scattering term, in both of which k_1 is the local integration variable and p_2 is the local conserved variable. In contrast, for quasiparticles initially near even nodes (2 or 4), the node index sum yields only an intra-node scattering term, for which k_2 is the local integration variable and p_1 is the local conserved variable. It is therefore clear that once we change to local coordinates, we obtain from Eq. (3.4) two self-energy expressions, one for odd nodes and one for even nodes. For odd nodes:

$$\tilde{\Sigma}^o(p_2, i\omega) = \frac{n_T}{2v_f}\tilde{\tau}_3 \int \frac{dk_1}{\pi} \left[V_1^2 \tilde{\mathcal{G}}^o(k_1, p_2, i\omega) + V_3^2 \tilde{\mathcal{G}}^o(k_1, -p_2, i\omega)\right] \tilde{\tau}_3 \tag{3.6}$$

whereas for even nodes:

$$\tilde{\Sigma}^e(p_1, i\omega) = \frac{n_T}{2v_2}\tilde{\tau}_3 \int \frac{dk_2}{\pi} \left[V_1^2 \tilde{\mathcal{G}}^e(p_1, k_2, i\omega)\right] \tilde{\tau}_3 \tag{3.7}$$

where the superscripts 'o' and 'e' denote odd and even respectively. Here we have parameterized the scattering potential using the notation defined in Chapter 2 whereby V_1 defines the potential for an intra-node scattering event and V_3 defines the potential for an opposite-node scattering event. Note that for both odd nodes and even nodes, the self-energy is a function of frequency as well as the conserved component of the local scaled momentum, p_2 for the odd case and p_1 for the even case, but never the momentum component along $k_\perp$. This is a tremendous simplification since it means that the self-energy functions built into the right-hand side of Eqs. (3.6) and (3.7) will not be functions of the integration variables and can always be treated as constants with respect to the integrals. It is this fact that makes these equations tractable.

Since the bare Green's function, Eq. (3.1), has no $\tilde{\tau}_2$ component, it is clear from the form of Eqs. (3.2) and (3.4) that it is self-consistent for the self-energy matrix to lack a $\tilde{\tau}_2$ component as well. It is therefore convenient to write the odd-node and even-node self-energy matrices in the form

$$\tilde{\Sigma}^j = \Sigma^j \tilde{\mathbb{1}} + \Sigma_1^j \tilde{\tau}_3 + \Sigma_2^j \tilde{\tau}_1 \tag{3.8}$$

where $j = \{o, e\}$. It then follows from Eq. (3.2) that the corresponding dressed Green's functions can be expressed as

$$\tilde{\mathcal{G}}^j(q_1, q_2, i\omega) = \frac{(i\omega - \Sigma^j)\tilde{\mathbb{1}} + (q_1 + \Sigma_1^j)\tilde{\tau}_3 + (q_2 + \Sigma_2^j)\tilde{\tau}_1}{(i\omega - \Sigma^j)^2 - (q_1 + \Sigma_1^j)^2 - (q_2 + \Sigma_2^j)^2} \tag{3.9}$$

where (q_1, q_2) is the scaled momentum about a particular node and the self-energy components are functions of q_2 for odd nodes and q_1 for even nodes. This expression for the Green's functions in terms of the self-energies together with Eqs. (3.6) and (3.7), giving the self-energies in terms of the Green's functions, comprise matrix equations which can be solved self-consistently for the odd-node and even-node self-energies.

Let us consider the odd case first. Shifting the integration variable k_1 by Σ_1^o,

we see that the $\tilde{\tau}_3$ term integrates to zero and therefore $\Sigma_1^o = 0$. Then continuing $i\omega \to \omega + i\delta$ and making the ansatz (which will soon be shown valid) that Σ^o is an even function of p_2 while Σ_2^o is an odd function of p_2, we obtain

$$\Sigma^o = \int \frac{dk_1}{\pi} \frac{\alpha^o(\omega - \Sigma^o)}{(\omega - \Sigma^o)^2 - (p_2 + \Sigma_2^o)^2 - k_1^2} \tag{3.10}$$

$$\Sigma_2^o = \int \frac{dk_1}{\pi} \frac{-\alpha_1^o(p_2 + \Sigma_2^o)}{(\omega - \Sigma^o)^2 - (p_2 + \Sigma_2^o)^2 - k_1^2} \tag{3.11}$$

$$\alpha^o \equiv \frac{n_T(V_1^2 + V_3^2)}{2v_f} \qquad \alpha_1^o \equiv \frac{n_T(V_1^2 - V_3^2)}{2v_f} \tag{3.12}$$

where $\Sigma^o = \Sigma^o(p_2, \omega)$ and $\Sigma_2^o = \Sigma_2^o(p_2, \omega)$ are now retarded functions.

For even nodes, we follow an analogous procedure and obtain results of the same form. This time, shifting the integration variable k_2 by Σ_2^e, it is the $\tilde{\tau}_1$ term that integrates to zero such that $\Sigma_2^e = 0$. Continuing $i\omega \to \omega + i\delta$ to obtain retarded functions $\Sigma^e = \Sigma^e(p_1, \omega)$ and $\Sigma_1^e = \Sigma_1^e(p_1, \omega)$, we find

$$\Sigma^e = \int \frac{dk_2}{\pi} \frac{\alpha^e(\omega - \Sigma^e)}{(\omega - \Sigma^e)^2 - (p_1 + \Sigma_1^e)^2 - k_2^2} \tag{3.13}$$

$$\Sigma_1^e = \int \frac{dk_2}{\pi} \frac{\alpha_1^e(p_1 + \Sigma_1^e)}{(\omega - \Sigma^e)^2 - (p_1 + \Sigma_1^e)^2 - k_2^2} \tag{3.14}$$

$$\alpha^e \equiv \alpha_1^e \equiv \frac{n_T V_1^2}{2v_2} \tag{3.15}$$

where we have defined α_1^e in analogy with the odd node case.

In light of the similarities between the odd and even results, we can treat both cases on the same footing by defining for $j = \{\text{odd}, \text{even}\}$: $k = \{k_1, k_2\}$, $p = \{p_2, p_1\}$, $\Sigma = \{\Sigma^o, \Sigma^e\}$, $\Sigma_1 = \{\Sigma_2^o, \Sigma_1^e\}$, $\alpha = \{\alpha^o, \alpha^e\}$, $\alpha_1 = \{\alpha_1^o, \alpha_1^e\}$, and $\eta = \{-1, +1\}$. Hence, keeping in mind that our new variables have different meanings for odd and even nodes, we can write

$$\Sigma = \int \frac{dk}{\pi} \frac{\alpha(\omega - \Sigma)}{(\omega - \Sigma)^2 - (p + \Sigma_1)^2 - k^2} \tag{3.16}$$

$$\Sigma_1 = \int \frac{dk}{\pi} \frac{\eta\alpha_1(p + \Sigma_1)}{(\omega - \Sigma)^2 - (p + \Sigma_1)^2 - k^2} = \eta \frac{\alpha_1}{\alpha} \frac{p + \Sigma_1}{\omega - \Sigma} \Sigma \tag{3.17}$$

where the second equality in Eq. (3.17) was achieved by making use of Eq. (3.16). Solving Eq. (3.17) for Σ_1 in terms of Σ, plugging the result into Eq. (3.16), and evaluating the integral we find

$$\Sigma = \frac{-i\alpha}{\left[1 - \left(\frac{p}{\omega - \gamma\Sigma}\right)^2\right]^{1/2}} \qquad \Sigma_1 = \frac{(\gamma - 1)p}{\omega - \gamma\Sigma} \Sigma \tag{3.18}$$

where we have defined $\gamma \equiv 1 + \eta\alpha_1/\alpha$. This equation will be solved numerically in Sec. 3.6.2 to obtain an exact result for the self-energy.

Fortunately, in the experimentally relevant "thermal regime", $\Omega, 1/\tau \ll T \ll \Delta_0$, we can extract an approximate analytical result. As will be shown in the microwave conductivity calculation discussed in the following section, the energies of interest are $|\omega|$ on the order of T and what we have called α is on the order of $1/\tau$. Thus, in the thermal regime, we are justified in taking the limit $|\omega| \gg \alpha$ such that we can set $\omega - \gamma\Sigma \approx \omega$. As a result, defining real and imaginary parts via $\Sigma = \Lambda - i\Gamma$ and $\Sigma_1 = \Lambda_1 - i\Gamma_1$, we find the approximate expressions

$$\Gamma \approx \alpha \frac{\theta(|\omega| - |p|)}{\sqrt{1 - \left(\frac{p}{\omega}\right)^2}} \qquad \Lambda \approx -\alpha\,\mathrm{sgn}(\omega) \frac{\theta(|p| - |\omega|)}{\sqrt{\left(\frac{p}{\omega}\right)^2 - 1}} \tag{3.19}$$

$$\Gamma_1 \approx \eta\alpha_1 \frac{p}{\omega} \frac{\theta(|\omega| - |p|)}{\sqrt{1 - \left(\frac{p}{\omega}\right)^2}} \qquad \Lambda_1 \approx -\eta\alpha_1 \frac{p}{|\omega|} \frac{\theta(|p| - |\omega|)}{\sqrt{\left(\frac{p}{\omega}\right)^2 - 1}} \tag{3.20}$$

where the sharp cutoffs of the theta-functions are clearly artifacts of our approximation that are smoothed away in the exact solution. In the following section, we will make use of these thermal-regime self-energy functions to obtain an analytic expression for the microwave conductivity in the experimentally relevant parameter regime.

3.5 Microwave Conductivity Calculation

The electrical conductivity tensor can be calculated by means of the Kubo formula

$$\overleftrightarrow{\sigma}(\Omega, T) = -\frac{\mathrm{Im}\ \overleftrightarrow{\Pi}_{ret}(\Omega)}{\Omega} \tag{3.21}$$

where $\overleftrightarrow{\Pi}_{ret}(\Omega) = \overleftrightarrow{\Pi}(i\Omega \to \Omega + i\delta)$ and $\overleftrightarrow{\Pi}(i\Omega)$ is the Matsubara polarization function (or current-current correlation function). Evaluating the diagram in Fig. 3-5(a) we find

$$\overleftrightarrow{\Pi}(i\Omega) = \frac{1}{\beta} \sum_{i\omega} \sum_{\mathbf{p}} e^2 v_f^2 \hat{\mathbf{v}}_{fp} \mathrm{Tr}\left[\tilde{\mathcal{G}}(\mathbf{p}, i\omega)\tilde{\mathcal{G}}(\mathbf{p}, i\omega + i\Omega)\tilde{\mathbf{\Gamma}}(\mathbf{p}, i\omega, i\Omega)\right] \tag{3.22}$$

where $\hat{\mathbf{v}}_{fp}$ points in the direction of the Fermi velocity and $\tilde{\mathbf{\Gamma}}$ is the dressed vertex function. Including vertex corrections within the Born approximation, $\tilde{\mathbf{\Gamma}}$ is calculated by evaluating the ladder diagrams in Fig. 3-5(b). Doing so, we obtain

$$\begin{aligned} \tilde{\mathbf{\Gamma}}(p_\perp, p_\parallel, i\omega, i\Omega) &= \hat{\mathbf{v}}_{fp}\tilde{\mathbb{1}} + \sum_{k_\perp} n_T \left|V(p_\perp - k_\perp)\right|^2 \\ &\times \tilde{\tau}_3 \tilde{\mathcal{G}}(k_\perp, p_\parallel, i\omega + i\Omega)\tilde{\mathbf{\Gamma}}(k_\perp, p_\parallel, i\omega, i\Omega)\tilde{\mathcal{G}}(k_\perp, p_\parallel, i\omega)\tilde{\tau}_3 \end{aligned} \tag{3.23}$$

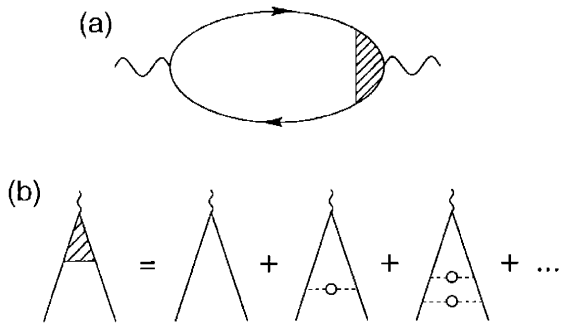

Figure 3-5: Polarization bubble and dressed vertex within Born approximation.

where n_T is the line defect density and $V(p_\perp - k_\perp)$ is the line defect scattering potential. Once again, due to the 1d nature of our scattering, the momentum component parallel to the defect lines, $p_\parallel$, is conserved and we only integrate over the perpendicular component, $k_\perp$. Replacing momentum integrals by sums over node index and integrals over local scaled momenta, the polarization tensor takes the form

$$\begin{aligned}\overleftrightarrow{\Pi}(i\Omega) &= e^2 v_f^2 \sum_{j=1}^{4} \hat{\mathbf{v}}_f^j \hat{\mathbf{v}}_f^j \frac{1}{\beta} \sum_{i\omega} \int \frac{d^2p}{(2\pi)^2 v_f v_2} \\ &\times \mathrm{Tr}\left[\tilde{\mathcal{G}}^j(\mathbf{p}, i\omega)\tilde{\mathcal{G}}^j(\mathbf{p}, i\omega + i\Omega)\left(\tilde{\mathbb{1}} + \tilde{\Lambda}^j(\mathbf{p}, i\omega, i\Omega)\right)\right] \end{aligned} \tag{3.24}$$

where we have defined a vertex correction function, $\tilde{\Lambda}^j$, such that

$$\tilde{\mathbf{\Gamma}}^j(\mathbf{p}, i\omega, i\Omega) = \hat{\mathbf{v}}_f^j \left(\tilde{\mathbb{1}} + \tilde{\Lambda}^j(\mathbf{p}, i\omega, i\Omega)\right). \tag{3.25}$$

Note that $\tilde{\Lambda}^j$ depends only on the conserved component of the scaled local momentum (i.e. $\tilde{\Lambda}^o = \tilde{\Lambda}^o(p_2, i\omega, i\Omega)$ while $\tilde{\Lambda}^e = \tilde{\Lambda}^e(p_1, i\omega, i\Omega)$). Since quasiparticles in odd nodes (1 or 3) can be scattered either intra-node or to the opposite-node while quasiparticles in even nodes (2 or 4) can only be scattered intra-node, we must treat the odd and even cases separately as we proceed to calculate the vertex correction.

For odd nodes, Eqs. (3.23) and (3.25) yield

$$\begin{aligned}\tilde{\Lambda}^o(p_2) &= \frac{n_T V_1^2}{2v_f} \int \frac{dk_1}{\pi} \tilde{\tau}_3 \tilde{\mathcal{G}}^o(k_1, p_2, i\omega + i\Omega)\left(\tilde{\mathbb{1}} + \tilde{\Lambda}^o(p_2)\right)\tilde{\mathcal{G}}^o(k_1, p_2, i\omega)\tilde{\tau}_3 \\ &- \frac{n_T V_3^2}{2v_f} \int \frac{dk_1}{\pi} \tilde{\tau}_3 \tilde{\mathcal{G}}^o(k_1, -p_2, i\omega + i\Omega)\left(\tilde{\mathbb{1}} + \tilde{\Lambda}^o(-p_2)\right)\tilde{\mathcal{G}}^o(k_1, -p_2, i\omega)\tilde{\tau}_3 \end{aligned} \tag{3.26}$$

where we have suppressed the frequency dependence of $\tilde{\Lambda}^o$ for simplicity. Taking the Nambu-space trace, noting that $\tilde{\tau}_3 \tilde{\mathcal{G}}^o(p_2)\tilde{\tau}_3 = \tilde{\mathcal{G}}^o(-p_2)$, and using the cyclic properties of the trace, we find

$$\mathrm{Tr}\left[\tilde{\Lambda}^o(p_2)\right] = \mathrm{Tr}\left[\frac{n_T}{2v_f}\tilde{I}^o(p_2)\left((V_1^2 - V_3^2)\tilde{\mathbb{1}} + V_1^2\tilde{\Lambda}^o(p_2) - V_3^2\tilde{\tau}_3\tilde{\Lambda}^o(-p_2)\tilde{\tau}_3\right)\right] \tag{3.27}$$

where we have defined

$$\begin{aligned}\tilde{I}^o(p_2) &\equiv \int \frac{dk_1}{\pi}\tilde{\mathcal{G}}^o(k_1,p_2,i\omega)\tilde{\mathcal{G}}^o(k_1,p_2,i\omega+i\Omega) \\ &\equiv I^o(p_2)\tilde{\mathbb{1}} + I_1^o(p_2)\tilde{\tau}_1\end{aligned} \tag{3.28}$$

with $I^o(p_2)$ an even function and $I_1^o(p_2)$ an odd function. Note that the fact that $\tilde{I}^o(p_2)$ can be written in this form is merely assumed at this point but will be demonstrated later. Manipulating further and making the additional assumption (which will soon be shown valid) that $\mathrm{Tr}[\tilde{\Lambda}^o(p_2)]$ is an even function and $\mathrm{Tr}[\tilde{\tau}_1\tilde{\Lambda}^o(p_2)]$ is an odd function, we can write

$$\mathrm{Tr}\left[\tilde{\Lambda}^o\right] = \alpha_1^o I^o\left(2+\mathrm{Tr}\left[\tilde{\Lambda}^o\right]\right) + \alpha_1^o I_1^o\,\mathrm{Tr}\left[\tilde{\tau}_1\tilde{\Lambda}^o\right] \tag{3.29}$$

where $\alpha_1^o = n_T(V_1^2 - V_3^2)/2v_f$, as defined in Eq. (3.12), and we have now suppressed the p_2 dependences. Going back to Eq. (3.26) but this time multiplying by $\tilde{\tau}_1$ before taking the trace, we can proceed along analogous lines to show that

$$\mathrm{Tr}\left[\tilde{\tau}_1\tilde{\Lambda}^o\right] = \alpha_1^o J^o\,\mathrm{Tr}\left[\tilde{\tau}_1\tilde{\Lambda}^o\right] + \alpha_1^o J_1^o\left(2+\mathrm{Tr}\left[\tilde{\Lambda}^o\right]\right) \tag{3.30}$$

where we have now defined

$$\begin{aligned}\tilde{J}^o(p_2) &\equiv -\int \frac{dk_1}{\pi}\tilde{\mathcal{G}}^o(k_1,p_2,i\omega)\tilde{\tau}_1\tilde{\mathcal{G}}^o(k_1,p_2,i\omega+i\Omega) \\ &\equiv J_1^o(p_2)\tilde{\mathbb{1}} + J^o(p_2)\tilde{\tau}_1\end{aligned} \tag{3.31}$$

with $J^o(p_2)$ an even function and $J_1^o(p_2)$ an odd function. Solving Eqs. (3.29) and (3.30) simultaneously, we find that

$$\mathrm{Tr}\left[\tilde{\Lambda}^o\right] = \frac{2\alpha_1^o\left(I^o + \frac{\alpha_1^o I_1^o J_1^o}{1-\alpha_1^o J^o}\right)}{1-\alpha_1^o\left(I^o + \frac{\alpha_1^o I_1^o J_1^o}{1-\alpha_1^o J^o}\right)} \tag{3.32}$$

and

$$\mathrm{Tr}\left[\tilde{\tau}_1\tilde{\Lambda}^o\right] = \frac{\frac{2\alpha_1^o J_1^o}{1-\alpha_1^o J^o}}{1-\alpha_1^o\left(I^o + \frac{\alpha_1^o I_1^o J_1^o}{1-\alpha_1^o J^o}\right)} \tag{3.33}$$

from which it is clear, given the defined parity of I^o, I_1^o, J^o, and J_1^o, that as a function of p_2, $\mathrm{Tr}[\tilde{\Lambda}^o]$ is odd and $\mathrm{Tr}[\tilde{\tau}_1\tilde{\Lambda}^o]$ is even, in agreement our prior assumptions. Finally, using Eqs. (3.28) and (3.29) and the fact that the Pauli matrices are traceless, we can write

$$\mathrm{Tr}\left[\tilde{\Lambda}^o(p_2)\right] = \alpha_1^o\,\mathrm{Tr}\left[\tilde{I}^o(p_2)\left(\tilde{\mathbb{1}}+\tilde{\Lambda}^o(p_2)\right)\right] \tag{3.34}$$

which will prove a useful expression in what follows.

For even nodes, the vertex correction function takes the form

$$\tilde{\Lambda}^e(p_1) = \frac{n_T V_1^2}{2v_2}\int \frac{dk_2}{\pi}\tilde{\tau}_3\tilde{\mathcal{G}}^e(p_1,k_2,i\omega+i\Omega)\left(\tilde{\mathbb{1}}+\tilde{\Lambda}^e(p_1)\right)\tilde{\mathcal{G}}^e(p_1,k_2,i\omega)\tilde{\tau}_3. \tag{3.35}$$

Note that this even-node expression is of the same form as the corresponding odd-node expression, Eq. (3.26), but is somewhat simpler since we need only consider intra-node scattering. Taking the trace and cyclically permuting within the trace, we find

$$\mathrm{Tr}\left[\tilde{\Lambda}^e(p_1)\right] = \alpha_1^e \,\mathrm{Tr}\left[\tilde{I}^e(p_1)\left(\tilde{\mathbb{1}} + \tilde{\Lambda}^e(p_1)\right)\right] \tag{3.36}$$

where $\alpha_1^e = n_T V_1^2/2v_f$, as defined in Eq. (3.15), and we have defined

$$\begin{aligned} \tilde{I}^e(p_1) &\equiv \int \frac{dk_2}{\pi} \tilde{\mathcal{G}}^e(p_1, k_2, i\omega)\tilde{\mathcal{G}}^e(p_1, k_2, i\omega + i\Omega) \\ &\equiv I^e(p_1)\tilde{\mathbb{1}} + I_1^e(p_1)\tilde{\tau}_3. \end{aligned} \tag{3.37}$$

Making use of the second equality in Eq. (3.37) and further defining

$$\begin{aligned} \tilde{J}^e(p_1) &\equiv \int \frac{dk_2}{\pi} \tilde{\mathcal{G}}^e(p_1, k_2, i\omega)\tilde{\tau}_3\tilde{\mathcal{G}}^e(p_1, k_2, i\omega + i\Omega) \\ &\equiv J_1^e(p_1)\tilde{\mathbb{1}} + J^e(p_1)\tilde{\tau}_3 \end{aligned} \tag{3.38}$$

we obtain two coupled equations for $\mathrm{Tr}[\tilde{\Lambda}^e]$ and $\mathrm{Tr}[\tilde{\tau}_3\tilde{\Lambda}^e]$,

$$\mathrm{Tr}\left[\tilde{\Lambda}^e\right] = \alpha_1^e I^e\left(2 + \mathrm{Tr}\left[\tilde{\Lambda}^e\right]\right) + \alpha_1^e I_1^e \,\mathrm{Tr}\left[\tilde{\tau}_3\tilde{\Lambda}^e\right] \tag{3.39}$$

$$\mathrm{Tr}\left[\tilde{\tau}_3\tilde{\Lambda}^e\right] = \alpha_1^e J^e \,\mathrm{Tr}\left[\tilde{\tau}_3\tilde{\Lambda}^e\right] + \alpha_1^e J_1^e\left(2 + \mathrm{Tr}\left[\tilde{\Lambda}^e\right]\right). \tag{3.40}$$

Solving simultaneously yields

$$\mathrm{Tr}\left[\tilde{\Lambda}^e\right] = \frac{2\alpha_1^e\left(I^e + \frac{\alpha_1^e I_1^e J_1^e}{1-\alpha_1^e J^e}\right)}{1 - \alpha_1^e\left(I^e + \frac{\alpha_1^e I_1^e J_1^e}{1-\alpha_1^e J^e}\right)} \tag{3.41}$$

which has precisely the same form as in the odd case.

Due to this similarity in form, we can unite the odd and even cases by using the superscript $j = \{o, e\}$ and defining a generalized integration variable $k = \{k_1, k_2\}$ and a generalized conserved variable $p = \{p_2, p_1\}$. Doing so, we can define

$$K^j(p, i\omega, i\Omega) \equiv \frac{1}{2\alpha_1^j}\mathrm{Tr}\left[\tilde{\Lambda}^j(p, i\omega, i\Omega)\right] = \frac{I^j + \frac{\alpha_1^j I_1^j J_1^j}{1-\alpha_1^j J^j}}{1 - \alpha_1^j\left(I^j + \frac{\alpha_1^j I_1^j J_1^j}{1-\alpha_1^j J^j}\right)} \tag{3.42}$$

and note via Eqs. (3.34) and (3.36) that

$$\mathrm{Tr}\left[\tilde{I}^j(p, i\omega, i\Omega)\left(\tilde{\mathbb{1}} + \tilde{\Lambda}^j(p, i\omega, i\Omega)\right)\right] = 2K^j(p, i\omega, i\Omega). \tag{3.43}$$

Then going back to our expression for the polarization tensor, Eq. (3.24), and noting that

$$\hat{\mathbf{v}}_f^1\hat{\mathbf{v}}_f^1 + \hat{\mathbf{v}}_f^3\hat{\mathbf{v}}_f^3 = \overset{\leftrightarrow}{\mathbb{1}} + \overset{\leftrightarrow}{\tau}_1$$

$$\hat{\mathbf{v}}_f^2\hat{\mathbf{v}}_f^2 + \hat{\mathbf{v}}_f^4\hat{\mathbf{v}}_f^4 \;=\; \overleftrightarrow{\mathbb{1}} - \overleftrightarrow{\tau}_1 \tag{3.44}$$

we can write the tensor as the sum of an odd-node term and an even-node term

$$\overleftrightarrow{\Pi}(i\Omega) = \Pi^o(i\Omega)\left[\overleftrightarrow{\mathbb{1}} + \overleftrightarrow{\tau}_1\right] + \Pi^e(i\Omega)\left[\overleftrightarrow{\mathbb{1}} - \overleftrightarrow{\tau}_1\right] \tag{3.45}$$

where, for $j = \{o, e\}$,

$$\begin{aligned}\Pi^j(i\Omega) &= \frac{e^2}{4\pi}\frac{v_f}{v_2}\int dp\,\frac{1}{\beta}\sum_{i\omega}\mathrm{Tr}\Big[\int\frac{dk}{\pi}\tilde{\mathcal{G}}^j(k,p,i\omega)\tilde{\mathcal{G}}^j(p,k,i\omega+i\Omega)\left(\tilde{\mathbb{1}} + \tilde{\Lambda}^j(p,i\omega,i\Omega)\right)\Big] \\ &= \frac{e^2}{2\pi}\frac{v_f}{v_2}\int dp\,\frac{1}{\beta}\sum_{i\omega}K^j(p,i\omega,i\Omega).\end{aligned} \tag{3.46}$$

At this point, we would like to evaluate the Matsubara sum of $K^j(p,i\omega,i\Omega)$, analytically continue the Matsubara frequencies, and obtain retarded functions. To do so we should note that the internal and external frequencies, $i\omega$ and $i\Omega$, enter $K^j(p,i\omega,i\Omega)$ only through functions of "Matsubara-couplets" of the form $A(i\omega)B(i\omega+i\Omega)$, where both A and B have the analytic structure of a Matsubara Green's function. A procedure for evaluating Matsubara sums of functions of this type was developed in Appendix B of Chapter 2 (Sec. 2.8). Applying this procedure to the case at hand, we find that the imaginary part of the retarded polarization function takes the form

$$\mathrm{Im}\,\Pi^j_{ret}(\Omega) = \frac{e^2}{2\pi}\frac{v_f}{v_2}\int dp\int\frac{d\omega}{2\pi}\left(n_F(\omega+\Omega) - n_F(\omega)\right)\mathrm{Re}\left[K^j_B(p,\omega,\Omega) - K^j_A(p,\omega,\Omega)\right] \tag{3.47}$$

where n_F is the Fermi function and

$$\begin{aligned}K^j_A(p,\omega,\Omega) &= \lim_{i\Omega\to\Omega+i\delta}K^j(p,\omega+i\delta,i\Omega) \\ K^j_B(p,\omega,\Omega) &= \lim_{i\Omega\to\Omega+i\delta}K^j(p,\omega-i\delta,i\Omega)\end{aligned} \tag{3.48}$$

are what we will refer to as the A-form and B-form of $K^j(p,i\omega,i\Omega)$. Plugging into the Kubo formula, Eq. (3.21), this yields the conductivity tensor

$$\overleftrightarrow{\sigma}(\Omega,T) = \sigma^o(\Omega,T)\left[\overleftrightarrow{\mathbb{1}} + \overleftrightarrow{\tau}_1\right] + \sigma^e(\Omega,T)\left[\overleftrightarrow{\mathbb{1}} - \overleftrightarrow{\tau}_1\right] \tag{3.49}$$

where

$$\begin{aligned}\sigma^j(\Omega,T) &= \frac{e^2}{4\pi^2}\frac{v_f}{v_2}\int_{-\infty}^{\infty}d\omega\left(\frac{n_F(\omega)-n_F(\omega+\Omega)}{\Omega}\right) \\ &\times \int_{-\infty}^{\infty}dp\;\mathrm{Re}\left[K^j_B(p,\omega,\Omega) - K^j_A(p,\omega,\Omega)\right].\end{aligned} \tag{3.50}$$

The next step is to express K^j_A and K^j_B in terms of the self-energy calculated in Sec. 3.4. To do so we must first evaluate our expressions for the Matsubara-

formalism functions, I^j, I_1^j, J^j, and J_1^j, and then analytically continue to obtain the corresponding A-forms and B-forms. Dressed via the self-energy functions, the Matsubara Green's functions, evaluated at frequencies $i\omega$ and $i\omega + i\Omega$, take the form

$$\tilde{\mathcal{G}}^o(k,p,i\omega) = \frac{f_1^o \tilde{\mathbb{1}} + k\tilde{\tau}_3 + g_1^o \tilde{\tau}_1}{{f_1^o}^2 - k^2 - {g_1^o}^2} \tag{3.51}$$

$$\tilde{\mathcal{G}}^o(k,p,i\omega + i\Omega) = \frac{f_2^o \tilde{\mathbb{1}} + k\tilde{\tau}_3 + g_2^o \tilde{\tau}_1}{{f_2^o}^2 - k^2 - {g_2^o}^2} \tag{3.52}$$

for odd nodes and

$$\tilde{\mathcal{G}}^e(p,k,i\omega) = \frac{f_1^e \tilde{\mathbb{1}} + g_1^e \tilde{\tau}_3 + k\tilde{\tau}_1}{{f_1^e}^2 - {g_1^e}^2 - k^2} \tag{3.53}$$

$$\tilde{\mathcal{G}}^e(p,k,i\omega + i\Omega) = \frac{f_2^e \tilde{\mathbb{1}} + g_2^e \tilde{\tau}_3 + k\tilde{\tau}_1}{{f_2^e}^2 - {g_2^e}^2 - k^2} \tag{3.54}$$

for even nodes, where we have defined

$$\begin{aligned} f_1^j &\equiv i\omega - \Sigma^j(p,i\omega) \\ f_2^j &\equiv i\omega + i\Omega - \Sigma^j(p,i\omega + i\Omega) \\ g_1^j &\equiv p + \Sigma_1^j(p,i\omega) \\ g_2^j &\equiv p + \Sigma_1^j(p,i\omega + i\Omega). \end{aligned} \tag{3.55}$$

Plugging the dressed Green's functions into Eqs. (3.28), (3.31), (3.37), and (3.38), we find that

$$\begin{aligned} I(p,i\omega,i\Omega) &= \int \frac{dk}{\pi} \frac{f_1 f_2 + g_1 g_2 + k^2}{(f_1^2 - g_1^2 - k^2)(f_2^2 - g_2^2 - k^2)} \\ I_1(p,i\omega,i\Omega) = \eta J_1(p,i\omega,i\Omega) &= \int \frac{dk}{\pi} \frac{f_1 g_2 + f_2 g_1}{(f_1^2 - g_1^2 - k^2)(f_2^2 - g_2^2 - k^2)} \\ J(p,i\omega,i\Omega) &= \eta \int \frac{dk}{\pi} \frac{f_1 f_2 + g_1 g_2 - k^2}{(f_1^2 - g_1^2 - k^2)(f_2^2 - g_2^2 - k^2)} \end{aligned} \tag{3.56}$$

where $\eta = \{-1, 1\}$ for $j = \{o, e\}$ and we have suppressed the node-index superscripts for simplicity. Expanding the integrands via partial fraction decomposition, noting that the resulting integrals are precisely of the form that appear in Eqs. (3.16) and (3.17), and using this to relate the integrals to our self-energy functions, the above can be evaluated. Then analytically continuing as prescribed in (3.48), we obtain both the A-form functions

$$I_A = \frac{1}{\alpha} \frac{(f_2 + f_1)(\Sigma - \Sigma_+) + \eta \frac{\alpha}{\alpha_1}(g_2 - g_1)(\Sigma_1 + \Sigma_{1+})}{(f_2^2 - f_1^2) - (g_2^2 - g_1^2)}$$

$$I_{1A} = \frac{1}{\alpha} \frac{(g_2\Sigma - g_1\Sigma_+) + \eta \frac{\alpha}{\alpha_1}(f_2\Sigma_1 - f_1\Sigma_{1+})}{(f_2^2 - f_1^2) - (g_2^2 - g_1^2)}$$

$$J_A = \frac{\eta}{\alpha}\frac{(f_2 - f_1)(\Sigma + \Sigma_+) + \eta\frac{\alpha}{\alpha_1}(g_2 + g_1)(\Sigma_1 - \Sigma_{1+})}{(f_2^2 - f_1^2) - (g_2^2 - g_1^2)} \tag{3.57}$$

and the B-form functions

$$I_B = \frac{1}{\alpha}\frac{(f_2 + f_1^*)(\Sigma^* - \Sigma_+) + \eta\frac{\alpha}{\alpha_1}(g_2 - g_1^*)(\Sigma_1^* + \Sigma_{1+})}{(f_2^2 - f_1^{*2}) - (g_2^2 - g_1^{*2})}$$

$$I_{1B} = \frac{1}{\alpha}\frac{(g_2\Sigma^* - g_1^*\Sigma_+) + \eta\frac{\alpha}{\alpha_1}(f_2\Sigma_1^* - f_1^*\Sigma_{1+})}{(f_2^2 - f_1^{*2}) - (g_2^2 - g_1^{*2})}$$

$$J_B = \frac{\eta}{\alpha}\frac{(f_2 - f_1^*)(\Sigma^* + \Sigma_+) + \eta\frac{\alpha}{\alpha_1}(g_2 + g_1^*)(\Sigma_1^* - \Sigma_{1+})}{(f_2^2 - f_1^{*2}) - (g_2^2 - g_1^{*2})} \tag{3.58}$$

where all self-energies are now retarded and $\Sigma \equiv \Sigma(p,\omega)$, $\Sigma_+ \equiv \Sigma(p,\omega+\Omega)$, $\Sigma_1 \equiv \Sigma_1(p,\omega)$, $\Sigma_{1+} \equiv \Sigma_1(p,\omega+\Omega)$, $f_1 = \omega - \Sigma$, $f_2 = \omega + \Omega - \Sigma_+$, $g_1 = p + \Sigma_1$, and $g_2 = p + \Sigma_{1+}$. Then, in terms of the A-form and B-form functions above,

$$K_{(A,B)} = \frac{I_{(A,B)} + \frac{\eta\alpha_1 I_{1(A,B)}^2}{1-\alpha_1 J_{(A,B)}}}{1 - \alpha_1\left(I_{(A,B)} + \frac{\eta\alpha_1 I_{1(A,B)}^2}{1-\alpha_1 J_{(A,B)}}\right)}. \tag{3.59}$$

Thus, given the self-energy functions, Σ and Σ_1, Eqs. (3.49), (3.50), (3.57), (3.58), and (3.59) constitute a well-defined prescription for calculating the conductivity tensor. In Sec. 3.6.2, these equations will be evaluated numerically, in conjunction with a numerical solution for the self-energy, in order to obtain an exact result for the conductivity.

However, in the thermal regime, $\Omega, 1/\tau \ll T \ll \Delta_0$, we are justified in taking the limit $\Omega, \alpha, \alpha_1 \ll |\omega|$, which simplifies our results significantly and allows for an analytical solution. Taking this limit and using the thermal regime self-energy calculated in Sec. 3.4, we find that the B-form results become

$$I_B \approx \frac{\omega}{p} I_{1B} \approx \eta\left(\frac{\omega}{p}\right)^2 J_B \approx \frac{\frac{1}{\alpha}}{1 + \eta\frac{\alpha_1}{\alpha}\left(\frac{p}{\omega}\right)^2 - i\frac{\Omega}{2\Gamma}} \tag{3.60}$$

where

$$\Gamma \approx \alpha\frac{\theta(|\omega| - |p|)}{\sqrt{1 - \left(\frac{p}{\omega}\right)^2}} \tag{3.61}$$

as expressed in Eq. (3.19). Remarkably, these functions conspire to give K_B the surprisingly simple form

$$K_B \approx \frac{2\tau_{tr}}{1 - i\Omega\tau_{tr}\frac{\alpha}{\Gamma}} \tag{3.62}$$

where we have suggestively defined an effective transport scattering rate

$$\frac{1}{2\tau_{tr}} \equiv \alpha - \alpha_1. \tag{3.63}$$

Calculating the A-form functions to the same order as in the the B-form case, we find that

$$I_A \approx I_{1A} \approx J_A \approx 0 \quad \Longrightarrow \quad K_A \approx 0. \tag{3.64}$$

Therefore, taking the real part of $K_B - K_A$ and integrating over scaled momentum we see that

$$\int_{-\infty}^{\infty} dp \, \mathrm{Re}\,[K_B - K_A] = 4f(\Omega\tau_{tr})\frac{\tau_{tr}}{1+(\Omega\tau_{tr})^2}|\omega| \tag{3.65}$$

where we have defined the function

$$f(x) \equiv \sqrt{1+\frac{1}{x^2}}\,\mathrm{arctanh}\left(\frac{1}{\sqrt{1+\frac{1}{x^2}}}\right) \tag{3.66}$$

which goes as $1-x^2/3$ for small argument and as $\ln(2x)$ for large argument. Plugging into Eq. (3.50), noting that

$$\int_{-\infty}^{\infty} d\omega \, |\omega| \left(-\frac{\partial n_F}{\partial \omega}\right) = 2\ln(2)k_B T, \tag{3.67}$$

and writing the node-index superscripts explicitly, yields the node-j microwave conductivity

$$\sigma^j(\Omega,T) = \frac{e^2}{\pi^2}\frac{v_f}{v_2}2\ln(2)f(\Omega\tau_{tr}^j)\frac{\tau_{tr}^j}{1+(\Omega\tau_{tr}^j)^2}k_B T. \tag{3.68}$$

It is important to note that for odd nodes

$$\frac{1}{2\tau_{tr}^o} = \frac{n_T(V_1^2+V_3^2)}{2v_f} - \frac{n_T(V_1^2-V_3^2)}{2v_f} = \frac{n_T V_3^2}{v_f} \tag{3.69}$$

while for even nodes

$$\frac{1}{2\tau_{tr}^e} = \frac{n_T V_1^2}{2v_2} - \frac{n_T V_1^2}{2v_2} = 0. \tag{3.70}$$

Hence, for nonzero frequencies

$$\frac{1}{2\tau_{tr}^e} = 0 \quad \Longrightarrow \quad \sigma^e(\Omega,T) = 0 \tag{3.71}$$

so the even nodes make no contribution to the microwave conductivity. From a physical point of view, these results are quite logical. Since electrical current is proportional to Fermi velocity, it is directed outward along the Brillouin zone diagonals at each node (see Refs. [12, 57]). Therefore, quasiparticles in the vicinity of odd nodes carry current normal to the defect lines which is degraded via line defect scattering. However, quasiparticles about even nodes carry current parallel to the defect lines which is unaffected by their presence. Since a nonzero microwave conductivity requires a nonzero scattering rate, only the odd nodes can contribute. Hence

$$\overleftrightarrow{\sigma}(\Omega,T) = \sigma^o(\Omega,T)\left[\overleftrightarrow{\mathbb{1}} + \overleftrightarrow{\tau}_1\right] \tag{3.72}$$

which clearly contains off-diagonal components and is therefore spatially anisotropic. This is the case because we have been considering only a single domain in which all defect lines are aligned at $-45°$ to the horizontal. Since such a system certainly has a preferred direction, an anisotropic conductivity makes sense. However, in reality, we expect a detwinned crystal to have both $-45°$ and $+45°$ aligned domains. As discussed in Sec. 3.3, our results can be adapted to the $+45°$ case by swapping all odd designations for even and vice versa. Doing so simply changes the sign of the $\overleftrightarrow{\tau}_1$ term in Eq. (3.72). Therefore, averaging over domains with $\pm 45°$ defect lines cancels the off-diagonal components and yields an isotropic conductivity tensor

$$\overleftrightarrow{\sigma}(\Omega, T) = \frac{e^2}{\pi^2}\frac{v_f}{v_2} 2\ln(2) f(\Omega\tau_{tr}^o)\frac{\tau_{tr}^o}{1+(\Omega\tau_{tr}^o)^2} k_B T \overleftrightarrow{\mathbb{1}}. \tag{3.73}$$

Hence, within the thermal regime, Born scattering from extended linear defects in a d-wave superconductor yields both a linear temperature dependence and a near-Drude frequency dependence.

3.6 Results

3.6.1 Analytical Results

Now let us compare our thermal regime expression for the microwave conductivity due to extended linear defect scattering, Eq. (3.73), with the measured microwave conductivity of detwinned $YBa_2Cu_3O_{6.993}$ obtained via experiment by Hosseini *et al.* [25]. A fit of our calculated result to the temperature-dependent part of the measured conductivity data is presented in Fig. 3-6. Note that the close agreement seen in the figure was achieved with only two free parameters: the effective transport lifetime, τ_{tr}, and an overall scale factor. The fit yields a lifetime of 2.93×10^{-11}s which corresponds to a mean free path on the order of microns (quite reasonable for the high-purity sample in question). Assuming an anisotropy ratio, $v_f/v_2 = 21$, as measured via sub-Kelvin thermal conductivity by Taillefer and co-workers [42, 58], we obtain a scale factor of 0.6 by which our expression must be multiplied to fit the data. This is in line with the expected Fermi-liquid correction factor [23, 29, 24, 57], $\alpha_{fl}^2 \sim 0.4 - 0.5$, that has been obtained from measurements of the superfluid density [42, 59, 28, 43]. Thus, our thermal regime expression yields a quantitative fit to the temperature-dependent part of the measured data.

However, there are several features of the Hosseini data that are not captured by Eq. (3.73). First of all, for each of the frequencies at which data was taken, a temperature-independent shift was observed in addition to the temperature-dependent part plotted in Fig. 3-6. Yet in our thermal regime expression, $\sigma(\Omega, T = 0)$ is zero. Furthermore, though predominantly linear with temperature, the measured data deviates slightly, but noticeably, from linearity. In fact, Hosseini *et al.* note a gradual evolution from a concave-down (sub-linear) deviation at low frequencies to a concave-up (super-linear) deviation at high frequencies. Our thermal regime expression is strictly linear with temperature.

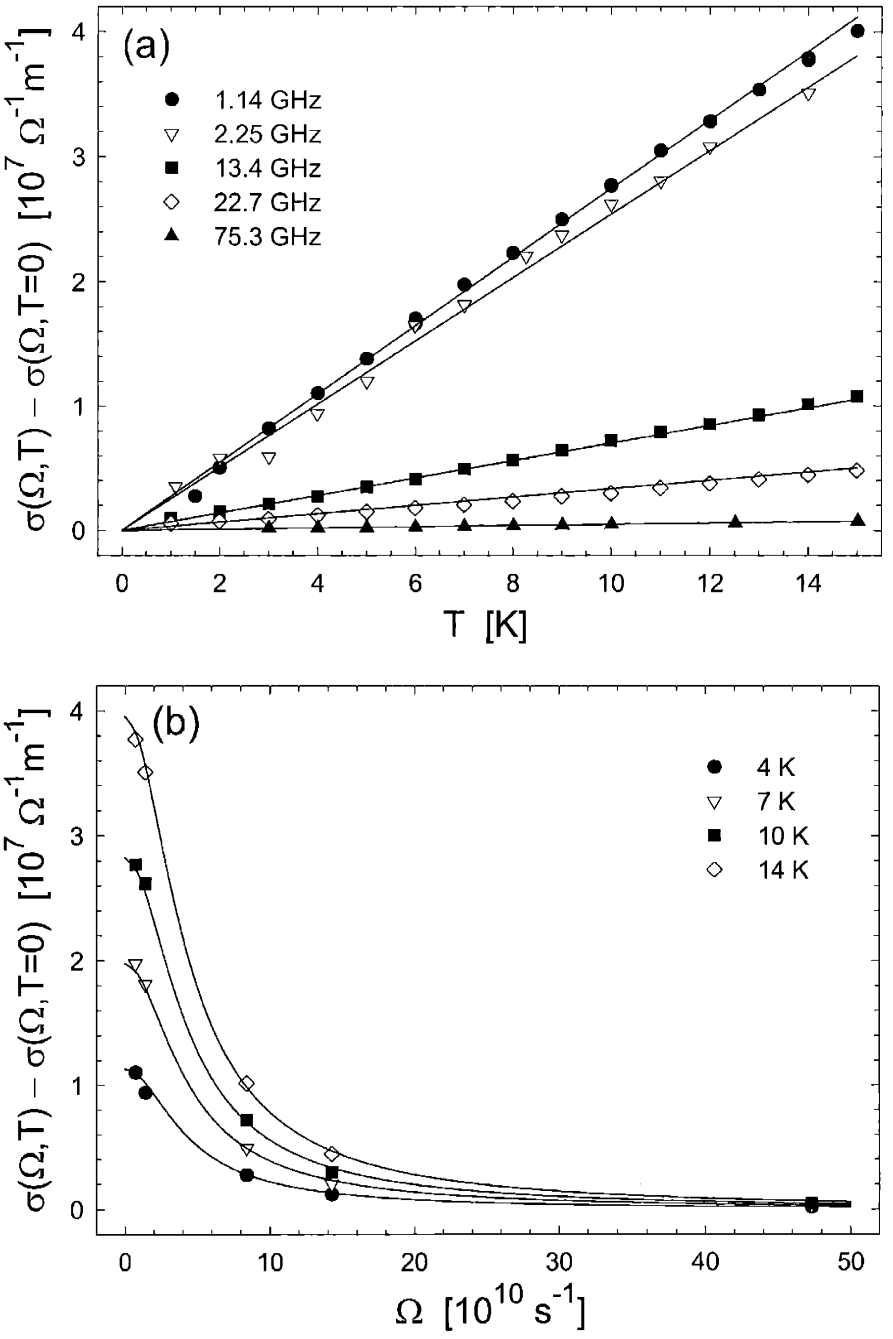

Figure 3-6: Fits to experiment of thermal-regime microwave conductivity plotted (a) versus temperature for each of five frequencies and (b) versus frequency for each of four temperatures. Points denote the temperature-dependent part of the microwave electrical conductivity measured in $YBa_2Cu_3O_{6.993}$ by Hosseini *et al.* [25]. Lines denote a two parameter fit of Eq. (3.73) obtained with transport lifetime, $\tau_{tr} = 2.93 \times 10^{-11}$s, and Fermi-liquid renormalization factor, $\alpha_{fl}^2 = 0.6$.

From the measured data (see Fig. 4 of Ref. [25]), it seems clear that the observed concave-down deviation at low frequencies results from the influence of inelastic scattering. For these low frequencies, the conductivity peak marking the onset of inelastic scattering appears just beyond the upper bound of our temperature range of interest. Quite naturally, the onset of inelastic scattering decreases the conductivity and yields a concave-down deviation from linearity. As we are concerned here with the nature of the low temperature elastic scattering mechanism, we do not expect to reproduce this feature. However, the observed high frequency (concave-up) deviations from linearity, as well as the temperature-independent shifts, do appear to be features of the elastic scattering which we seek to understand.

Since Eq. (3.73) is an approximate result, obtained by taking the limit $1/\tau, \Omega \ll T$ and thereby neglecting sub-dominant terms, it is possible that sub-dominant features (constant shift and deviation from linearity for high frequencies) were neglected when we assumed the thermal limit to obtain our analytical result. To see if these features emerge in a more exact solution, we present numerical results, valid beyond the thermal limit, in the following section.

3.6.2 Numerical Results

Recall from Sec. 3.4 that the self-energy in the presence of line defect scattering is determined by the self-consistent solution of Eq. (3.18) as a function of momentum and energy. While an analytic expression was obtained in the thermal limit, this equation must be solved numerically for more general parameter values. Doing so (via Newton's method) yields the self-energy functions, $\Sigma(p, \omega)$ and $\Sigma_1(p, \omega)$. Plugging these functions into Eqs. (3.49), (3.50), (3.57), (3.58), and (3.59) and numerically integrating over momentum and energy, we obtain the microwave conductivity for a particular temperature and frequency. Repeating this process for all temperatures and frequencies of interest yields an exact (numerical) result for the microwave conductivity.

Following this procedure, we computed the microwave conductivity as a function of temperature, from 0 to 15 K, for each of the five experimentally relevant frequencies. In all cases, we used values of the transport lifetime and Fermi-liquid correction factor obtained, in the previous section, from the fit of our thermal regime expression to experiment. The results for 1.14 GHz, 13.4 GHz, 22.7 GHz, and 75.3 GHz are plotted versus temperature in Fig. 3-7. In each plot, a straight line has been drawn between the first and last data points to highlight any deviation from linearity. These exact results confirm the conclusions of our thermal regime calculation, revealing a predominantly linear temperature-dependence and a near-Drude frequency dependence. In addition, at the high frequencies where our thermal regime approximations were least justified, we obtain, in qualitative agreement with experiment, concave-up deviations from linearity. Furthermore, these results do exhibit nonzero, albeit very small, offsets at zero temperature (most evident for 75.3 GHz). However, the computed offsets are far smaller than those observed experimentally. Perhaps the point defect scattering, which is certainly present but was ignored herein for simplicity, is required to reproduce this feature correctly. A more complete calculation must con-

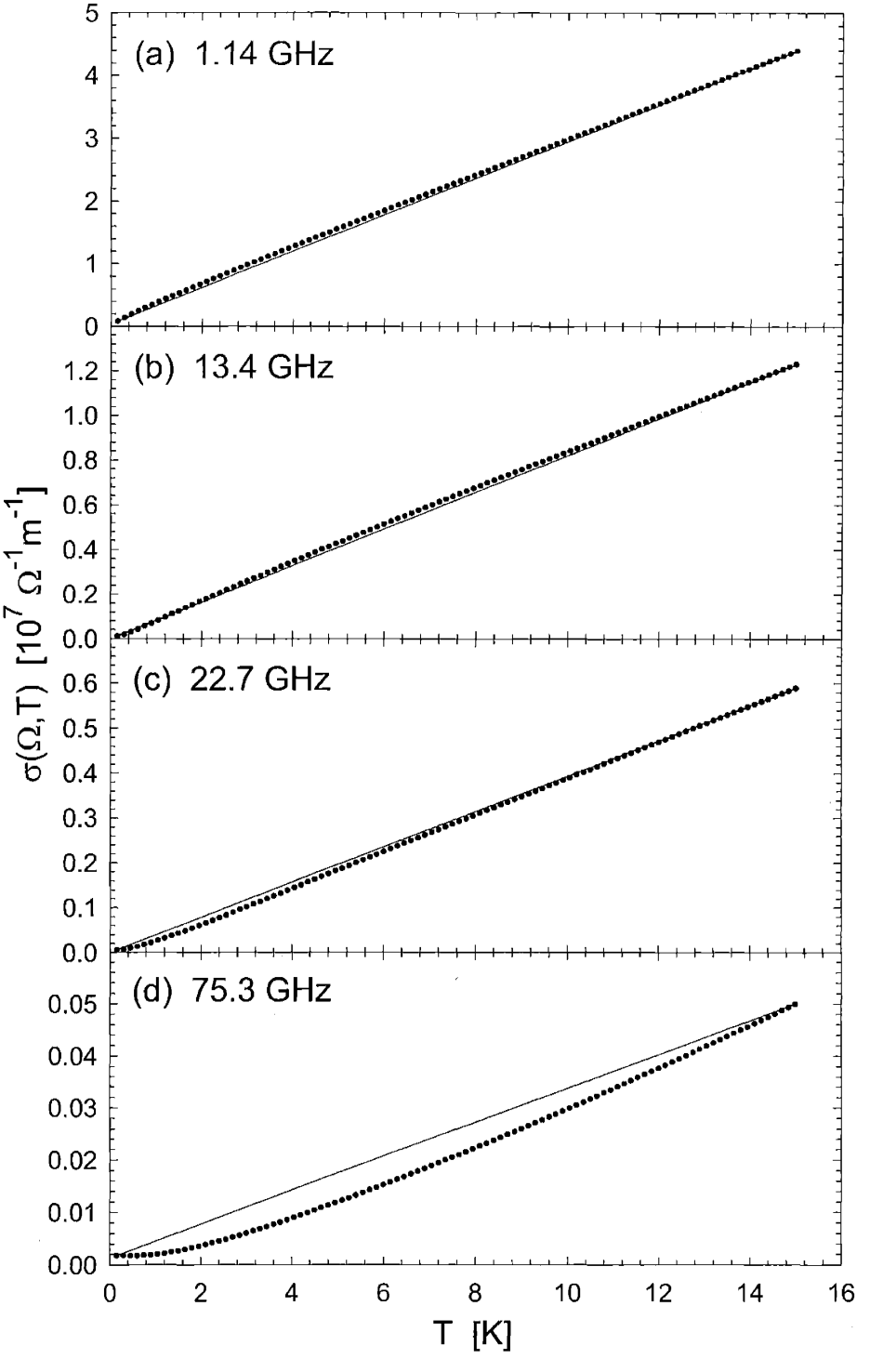

Figure 3-7: Results of numerical calculation of microwave conductivity plotted as a function of temperature for (a) 1.14 GHz, (b) 13.4 GHz, (c) 22.7 GHz, and (d) 75.3 GHz. Straight lines connecting the first and last data points have been included to highlight any deviation from linearity.

sider the effects of both extended linear defects and point defects in the same system. This is an important direction for future study.

3.7 Conclusions

The low temperature behavior of the microwave electrical conductivity measured in $YBa_2Cu_3O_{6.993}$ by Hosseini *et al.* [25] has been difficult to explain in terms of point defect (impurity) scattering. The basic problem is that the strong energy dependence of the low temperature quasiparticle density of states is directly reflected in a point defect scattering rate which is too energy dependent to produce a microwave conductivity that agrees with experiment. This suggests that an additional low temperature scattering mechanism may also be important.

We note that extended linear defect scattering is an appealing candidate. Unlike point defect scattering, line defect scattering does not sample the full quasiparticle density of states, so the line defect scattering rate need not inherit a strong energy dependence. Furthermore, lines are prevalent in as-grown YBCO in the form of twin boundaries. Although these twin boundaries are eliminated via the application of a uniaxial stress, if remnants of the twinning structure are left behind, they could take the form of line defects.

We have calculated (within the Born approximation) the self-energy and microwave conductivity due to scattering from a single domain of parallel, randomly spaced line defects, all aligned at $-45°$ to the crystal axes. We find that the anisotropic nature of line defect scattering clearly differentiates odd nodes (for which electrical current is perpendicular to the defect lines) from even nodes (for which electrical current is parallel to defect lines). For the former, both intra-node (forward) scattering and opposite-node (back) scattering are permitted, whereas for the latter, only intra-node (forward) scattering is allowed. By including vertex corrections in our calculation, we have accounted for the fact that back scattering is an effective means of degrading a current while forward scattering is not. Therefore, while odd nodes yield a nonzero transport scattering rate and microwave conductivity, even nodes make no contribution. The resulting conductivity tensor is anisotropic, reflective of the anisotropic nature of the scattering mechanism. Thus, for a sample in which all twin boundaries were parallel prior to detwinning, this anisotropy should be observable. (In fact, the measurement of the conductivity tensor in such a single-domain sample would serve as a good test for the presence of line defects.) However, since the samples in question contain multiple domains with line defects aligned at $\pm 45°$, we average over oppositely aligned domains to recover a conductivity scalar.

In the experimentally relevant limit, $1/\tau, \Omega \ll T \ll \Delta_0$, which we have called the thermal regime, our calculations simplify and we obtain an analytic expression for the microwave conductivity:

$$\overleftrightarrow{\sigma}(\Omega, T) = \frac{e^2}{\pi^2}\frac{v_f}{v_2} 2\ln(2) f(\Omega\tau_{tr}^o) \frac{\tau_{tr}^o}{1+(\Omega\tau_{tr}^o)^2} k_B T \overleftrightarrow{\mathbb{1}}. \tag{3.74}$$

As this result exhibits a linear temperature dependence and a near-Drude lineshape (modified logarithmically by the function $f(x)$ defined in Eq. (3.66)), it captures the most robust qualitative features of the Hosseini data. Furthermore, when we fit this expression to the temperature-dependent part of the measured conductivity (see Sec. 3.6.1), we obtain good quantitative agreement with reasonable values of our two fitting parameters, the transport lifetime and the Fermi-liquid renormalization factor. However, we note that this approximate analytical result fails to reproduce the more subtle features of the measured data: temperature-independent offsets and deviations of the temperature dependence from strict linearity at high frequencies. (We note that the deviations observed at low frequencies can be explained by the onset of inelastic scattering.)

In search of these subdominant features, we performed a numerical calculation, valid beyond the thermal regime. These numerical results (see Sec. 3.6.2) do exhibit deviations from linear temperature dependence at high frequencies, in qualitative agreement with experiment. While small temperature-independent offsets are also obtained, the magnitude of these is far smaller than observed experimentally. Perhaps the point defect scattering, which we have neglected herein, must be included to reproduce this feature.

The close agreement of our calculated conductivity with experiment strongly suggests that extended linear defects are indeed present in detwinned single crystals of $YBa_2Cu_3O_{6.993}$ and make an important contribution to the scattering. Our picture has been that these line defects are remnants of the twin boundary structure of the as-grown crystal, left behind after detwinning. We described, in Sec. 3.3, a detwinning scenario whereby the annihilation of twin boundaries leaves behind lines of oxygen vacancies in the CuO layer. While this is one example of a process that could yield extended linear defects, others are certainly possible. Our results, however, imply that something similar to this is taking place.

To answer remaining questions and provide a more complete picture of the low temperature scattering, future calculations should include the effects of both line defect scattering and point defect scattering in the same system. Nevertheless, these initial results suggest that scattering from extended linear defects has a significant influence on the observed microwave conductivity in detwinned single crystals of $YBa_2Cu_3O_{6.993}$.

Chapter 4

Quasiparticle Scattering from Vortices and Thermal Hall Conductivity in the Mixed State

I cannot end. I have already said too much; and know not whether I have yet said all, all that concerns thy interests; for to express the agitations of the vortex ... is beyond the power of words.

J. W. von Goethe

4.1 Introduction

The low energy excitations of a d-wave superconductor are the Bogoliubov quasiparticles which reside in the vicinity of the four gap nodes at which the order parameter vanishes. The physics of these quasiparticles can be probed experimentally via a variety of low temperature electrical and thermal transport measurements. Since quasiparticles are part electron and part hole, their energy is well defined but their charge is not. Thus, it is thermal current that follows quasiparticle current. As lattice vibrations can also transmit heat, the longitudinal thermal conductivity, κ_{xx}, has both an electronic and a phononic contribution. However, the thermal Hall conductivity, κ_{xy}, induced by a perpendicular magnetic field (the Righi-Leduc effect), is purely electronic in origin and the direct consequence of a transverse quasiparticle current. As a result, thermal Hall conductivity provides the most direct measure of low temperature quasiparticle transport in a d-wave superconductor.

Over the past few years, much progress has been made in measuring the thermal Hall conductivity of the cuprate superconductors in the mixed (vortex) state, $H_{c1} < H < H_{c2}$ [60, 61, 62, 63, 64]. Recently, Ong and co-workers [63] measured κ_{xy} in high-purity single crystals of slightly overdoped ($T_c = 89\ K$) $YBa_2Cu_3O_{6.99}$ (YBCO). The experiments were conducted in magnetic fields up to 14 Tesla and at temperatures ranging from 15 K to above T_c. Their data indicates that for temperatures less than 28 K, κ_{xy}/T^2 is only a function of the ratio $\sqrt{H}/T$. This is in agreement with the scaling theory proposed by Simon and Lee [65] which predicts that, for nodal

quasiparticles with a Dirac-like dispersion, the thermal Hall conductivity should scale as

$$\kappa_{xy}(H,T) \sim T^2 F_{xy}(\sqrt{H}/\gamma T) \tag{4.1}$$

where $\gamma = (k_B/v_f)\sqrt{c/\hbar e}$ and $F_{xy}(x)$ is a general scaling function. Furthermore, they find that for $\sqrt{H}/T < 0.042\sqrt{\text{Tesla}}/\text{K}$ the measured scaling function has the surprisingly simple form, $F_{xy}(x) \sim x$, such that

$$\kappa_{xy}(H,T) = C_0 T\sqrt{H} \tag{4.2}$$

where $C_0 = 1.51 \times 10^{-2}\text{W/mK}^2\sqrt{\text{Tesla}}$. For larger magnetic fields, the measured curves peak and then decrease. It is unusual to see $\sqrt{H}$ (rather than H) in a Hall response and this interesting result was theoretically unexpected. Yet such a simple functional form must have a simple explanation. In this investigation, we seek to provide it.

The key to this problem lies with the realization that we are dealing with the *high* temperature regime of low temperature quasiparticle transport. Since $T \ll T_c$ we are well within the superconducting state. Since $T \ll \Delta_0$ (the gap maximum), transport is dominated by quasiparticles excited in the vicinity of the gap nodes. (Quasiparticle dispersion is therefore given by the anisotropic Dirac spectrum, $E = (v_f^2 k_1^2 + v_2^2 k_2^2)^{1/2}$, where v_f is the Fermi velocity, v_2 is the slope of the gap, and k_1 and k_2 are defined locally about each node. We shall choose our axes such that gap nodes are located at $\pm p_F\hat{\mathbf{x}}$ and $\pm p_F\hat{\mathbf{y}}$ in momentum space.) Furthermore, the temperatures of interest are low enough that sources of inelastic scattering are frozen out. This is what we mean by low temperature quasiparticle transport. In the mixed state, the remaining energy scales are the impurity scattering rate, Γ_0, the vortex scattering rate, Γ_v, and the temperature. For the very clean samples in question, $\Gamma_0 \ll T$ for temperatures above a few Kelvin [25]. Since the interesting experimental results are obtained for $\sqrt{H} \ll \gamma T$, we are concerned with $\Gamma_v \ll T$. Hence, T is the dominant energy scale and this is the high temperature regime. As a result, the quasiparticles responsible for transport are thermally generated rather than impurity-induced [16, 20, 57] or magnetic field-induced [66, 67, 68]. (Note that thermal transport in the opposite, low T, regime has been discussed frequently in the recent literature [69, 70, 71, 72, 73].)

In this high T regime, the physical situation is relatively simple. Thermally excited quasiparticles carry the heat current. To understand the resulting thermal conductivity, we need only understand how they scatter from impurities and magnetic vortices. Furthermore, since $H \ll H_{c2}$, the vortices are dilute. We can therefore learn a lot by considering the scattering of a quasiparticle from a single vortex and assuming that all such scattering events are independent.

We take the following path. In Sec. 4.2 we discuss the nature of an extreme type II superconductor and show how the thermal conductivity (κ_{xx} and κ_{xy}) can be obtained from the single vortex scattering cross section. In Sec. 4.3, we develop our picture of a nodal quasiparticle scattering from a vortex. Then in Sec. 4.4, we consider the Bogoliubov-de Gennes equation, make a singular gauge transformation, and shift the origin of momentum space to the location of one of the gap nodes.

The resulting problem is one of an (anisotropic) Dirac fermion scattering from an effective non-central potential (due to the superflow) in the presence of antiperiodic boundary conditions (a consequence of our gauge choice) and small, yet important, curvature terms in the Hamiltonian. After obtaining the quasiparticle current functional in Sec. 4.5, we define our vortex model in Sec. 4.6 and make several important approximations. As far as scattering is concerned, the vortex has two parts: a circulating superflow and a Berry phase factor of (-1) acquired upon circling a vortex. We argue that the superflow is more important and neglect the Berry phase contribution. (Berry phase scattering in the absence of superflow is discussed in the Appendix (Sec. 4.14).) Furthermore, we neglect the anisotropy of the Dirac dispersion and take $v_f = v_2$. Although these approximations will prevent our results from being quantitatively accurate, we argue that our qualitative results reflect the essential physics of the problem. In Secs. 4.7 and 4.8, we expand the quasiparticle wave function in angular momentum eigenstates and obtain the resulting radial equations. We solve these equations outside the vortex, in Sec. 4.9, and inside the vortex, in Sec. 4.10. In Sec. 4.11, we match solutions and sum over all four gap nodes in order to obtain the single vortex scattering cross section. Results of our numerical calculations are presented in Sec. 4.12. We find $\kappa_{xx}(H,T)$ and $\kappa_{xy}(H,T)$ in surprisingly good qualitative agreement with experiment. In particular, we succeed in reproducing the simple, yet previously unexpected, form of the weak-field thermal Hall conductivity shown in Eq. (4.2). Conclusions are discussed in Sec. 4.13.

4.2 Thermal Conductivity from Vortex Cross Section

Consider the mixed state of a d-wave superconductor. Our picture is that of Fig. 4-1. In the presence of a magnetic field ($H > H_{c1}$), magnetic vortices penetrate the sample (a 2D CuO_2 layer). Vortices are distributed randomly, pinned to local defects. The cuprates are extreme type II superconductors in which the coherence length, ξ, is much smaller than the penetration depth, λ. As a result, while the vortex cores may be well separated, the magnetic field profiles overlap significantly such that there is little variation in the magnetic field across the sample. We therefore adopt the extreme type II limit of $\xi \to 0$ and $\lambda \to \infty$ and take the magnetic field to be constant, $\mathbf{H} = H\hat{\mathbf{z}}$. In this limit, there are only two remaining length scales. The first, $1/k$, is set by the temperature such that $k \equiv E/\hbar v_f = k_B T/\hbar v_f$. For anisotropic Dirac nodes, $k = \sqrt{k_1^2 + k_2^2(v_2/v_f)^2}$. Note that in the isotropic limit, this reduces to the magnitude of the quasiparticle momentum (measured from a node). The second length scale, R, is half of the average distance between vortices. With one flux quantum per vortex, $H\pi R^2 = \Phi_0 = hc/2e$, so we define $R \equiv \sqrt{\hbar c/eH}$. In terms of R, we can define the (2D) density of vortices to be $n_v = H/\Phi_0 = 1/\pi R^2$. Note that the ratio of these two length scales yields

$$kR = \frac{k_B T}{\hbar v_f}\sqrt{\frac{\hbar c}{eH}} = \frac{\gamma T}{\sqrt{H}} \tag{4.3}$$

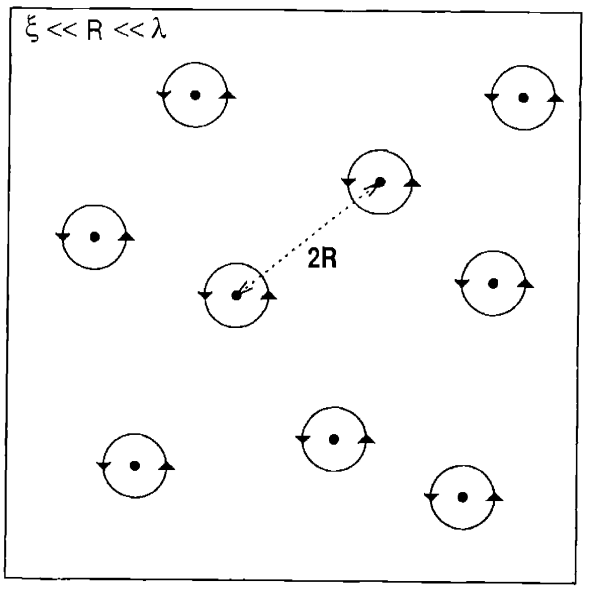

Figure 4-1: Schematic depiction of vortices in the mixed state of an extreme type II superconductor. Vortices are pinned to randomly distributed pinning centers and are separated by an average inter-vortex distance, $2R$. Since $\xi \ll R \ll \lambda$, vortex cores are point-like while the magnetic field profile of each vortex is quite extended. Therefore, the magnetic field is approximately uniform across the sample even though the vortices are well separated.

which is the inverse of the argument of the Simon-Lee scaling functions.

We shall consider nodal quasiparticles carrying a heat current in response to a thermal gradient applied in the x-direction. Thus we can express the thermal conductivity via

$$\mathbf{J} = \overleftrightarrow{\mathbf{K}}(-\nabla T) \quad \rightarrow \quad J_x = \kappa_{xx}(-\nabla T)_x \qquad J_y = \kappa_{yx}(-\nabla T)_x = -\kappa_{xy}(-\nabla T)_x \tag{4.4}$$

where we have used the fact that $\kappa_{xy} = -\kappa_{yx}$. In the parameter regime of interest, there are two sources of quasiparticle scattering, impurity scattering and vortex scattering. Both sources will contribute to the effective quasiparticle mean free path but only the vortices will contribute to the leftward deflection (skew scattering) of the quasiparticles.

Let us begin with the longitudinal component, κ_{xx}. Defining an effective quasiparticle mean free path, ℓ, we can express κ_{xx} in terms of the electronic specific heat, C_v, via

$$\kappa_{xx} = \frac{v\ell}{2} C_v \tag{4.5}$$

where v is the average quasiparticle velocity. (Note that in general, v will be a function of v_f and v_2, yet for the isotropic case, $v = v_f$.) The specific heat in the mixed state of a d-wave superconductor has been calculated (via semiclassical analysis) by Kopnin

and Volovik [67]. For magnetic fields small compared to the temperature, they find

$$C_v = \frac{9\zeta(3)}{\pi}\frac{k_B^3}{\hbar^2}\frac{n}{d}\frac{T^2}{v_f v_2}\left[1 + \frac{\ln(2)}{9\zeta(3)}\left(\frac{\sqrt{H}}{\gamma T}\right)^2\right] \tag{4.6}$$

where $\zeta(3) \approx 1.202$ and we have multiplied their single layer result by the stacking density of CuO_2 planes, n/d. Here the first term is the zero-field specific heat and the second is the leading small-H correction. The relative magnitude of these two terms is a measure of the extent to which the magnetic field contributes to the generation of nodal quasiparticles. Therefore, as long as $\sqrt{H} \ll \gamma T$, we are in the regime of thermally excited quasiparticles. As this condition corresponds to the parameter range of experimental interest, we can neglect the second term with respect to the first. Doing so, we obtain a very simple form for the longitudinal thermal conductivity

$$\frac{\kappa_{xx}}{T} = \alpha_0 k\ell \qquad \alpha_0 \equiv \frac{9\zeta(3)}{2\pi}\frac{k_B^2}{\hbar}\frac{n}{d}\frac{v}{v_2}. \tag{4.7}$$

Defining a thermal Hall angle, θ_H, we can write the transverse component as

$$\frac{\kappa_{xy}}{T} \equiv \frac{\kappa_{xx}}{T}\tan\theta_H = \alpha_0 k\ell \tan\theta_H. \tag{4.8}$$

Now we must calculate the mean free path and the thermal Hall angle.

The quasiparticle mean free path has contributions from both impurity scattering and vortex scattering. For small impurity densities and dilute vortices, we expect these contributions to be relatively independent. Thus, via Matthiessen's rule,

$$\frac{1}{\ell} = \frac{1}{\ell_0} + \frac{1}{\ell_v} \tag{4.9}$$

where ℓ_0 is the mean free path due to impurity scattering and ℓ_v is the mean free path due to vortex scattering. Since $1/\ell_v$ vanishes for $H = 0$, ℓ_0 can be obtained empirically via

$$\ell_0 = \frac{A}{k} \qquad A \equiv \frac{\kappa_e(T)}{\alpha_0 T} \tag{4.10}$$

where $\kappa_e(T)$ is the electronic part of $\kappa_{xx}(H = 0)$. As argued by Simon and Lee [65], we expect scaling even in the presence of disorder as long as the impurity scattering does not yield an additional length scale (as for Gaussian δ-function correlated disorder). If this is so, then A must be a T-independent constant. (Note that this is a different constant from that obtained in the universal limit [57].) Zero-field measurements of κ_{xx} in YBCO show that this is realized experimentally for $T < 30$ K [74, 62]. This is precisely the temperature range over which the κ_{xy} data obeys scaling [63]. As for the vortex scattering contribution, if we assume that vortex scattering events are uncorrelated, then we can express ℓ_v in terms of the single vortex transport cross section, $\sigma_{||}$, and the density of vortices, n_v. In this approximation, the transport

scattering rate is simply $1/\tau_v = n_v v \sigma_{||}$ and, since $\ell_v = v\tau_v$, we find

$$\ell_v = \frac{1}{n_v \sigma_{||}} = \frac{\pi R^2}{\sigma_{||}}. \tag{4.11}$$

Adding via Eq. (4.9) yields the total quasiparticle mean free path

$$\ell = \frac{1}{\frac{k}{A} + \frac{\sigma_{||}}{\pi R^2}}. \tag{4.12}$$

Since vortices are endowed with a circulation, it is also possible for the vortex scattering cross section to have a skew component, $\sigma_\perp$. If $\sigma_\perp$ is small, then when a quasiparticle encounters a vortex, there is a small probability that it will deflect to the side and contribute to J_y. The process repeats with each successive vortex until the quasiparticle has traveled a distance equal to its mean free path. Therefore, given a heat current, J_x, we can express the transverse heat current, J_y, via

$$J_y = J_x n_v \sigma_\perp \ell. \tag{4.13}$$

This relation, in conjunction with Eq. (4.4), yields a simple expression for the thermal Hall angle

$$\tan\theta_H \equiv \frac{\kappa_{xy}}{\kappa_{xx}} = -\frac{J_y}{J_x} = -\frac{\sigma_\perp \ell}{\pi R^2}. \tag{4.14}$$

The longitudinal and transverse components of the thermal conductivity are therefore related to the transport and skew components of the single vortex scattering cross section via

$$\frac{\kappa_{xx}}{T} = \alpha_0 k \frac{1}{\frac{k}{A} + \frac{\sigma_{||}}{\pi R^2}} \tag{4.15}$$

$$\frac{\kappa_{xy}}{T} = -\alpha_0 k \frac{\frac{\sigma_\perp}{\pi R^2}}{\left(\frac{k}{A} + \frac{\sigma_{||}}{\pi R^2}\right)^2} \tag{4.16}$$

When we calculate the vortex cross section explicitly, it will become clear that the skew cross section is a factor of k/p_F smaller than the transport cross section. It is therefore convenient to express these cross sections as

$$\sigma_{||} \equiv \frac{1}{k} f_{||}(kR) \qquad \sigma_\perp \equiv -\frac{1}{p_F} f_\perp(kR) \tag{4.17}$$

where $f_{||}(kR)$ and $f_\perp(kR)$ are dimensionless functions of a dimensionless argument. Defining $x \equiv 1/kR = \sqrt{H}/\gamma T$ and noting that $k/p_F = k_B T/2E_F$ we find that κ_{xx} and κ_{xy} take the form

$$\frac{\kappa_{xx}}{T} = \alpha_0 \frac{1}{\frac{1}{A} + \frac{1}{\pi} x^2 f_{||}\left(\frac{1}{x}\right)} \tag{4.18}$$

$$\frac{\kappa_{xy}}{T^2} = \frac{\alpha_0 k_B}{2E_F} \frac{\frac{1}{\pi}x^2 f_\perp\left(\frac{1}{x}\right)}{\left(\frac{1}{A} + \frac{1}{\pi}x^2 f_\parallel\left(\frac{1}{x}\right)\right)^2} \tag{4.19}$$

In the sections that follow, we proceed to explicitly calculate $f_\parallel(kR)$ and $f_\perp(kR)$ by considering the quantum mechanical scattering of a quasiparticle from a single vortex.

4.3 Single Vortex Scattering

We wish to consider a quasiparticle, in a state with a particular energy and current, scattering from a magnetic vortex into another state, of the same energy, with a different current. At low temperatures, quasiparticles are excited in the vicinity of the four gap nodes in momentum space. The nodal structure of the Brillouin zone is depicted in Fig. 4-2(a). Following Simon and Lee [65], we have defined coordinate axes, rotated by 45° from the usual crystal axes, such that the gap nodes are located on-axis at $\pm p_F\hat{\mathbf{x}}$ and $\pm p_F\hat{\mathbf{y}}$. In the neighborhood of a node, the quasiparticle excitation energy is given by the anisotropic Dirac spectrum, $E_k = \sqrt{v_f^2 k_1^2 + v_2^2 k_2^2}$, where the k_1 and k_2 axes are defined, respectively, to be perpendicular and parallel to the local Fermi surface. The surfaces of equal energy are therefore ellipses centered about each of the nodes. The quasiparticle current is given by the group velocity, $\mathbf{v}_G = \nabla_k E_k$, directed outward from the node centers, perpendicular to the ellipses of constant energy.

In coordinate space, the quasiparticle is represented as an incident plane wave. The single $(hc/2e)$ vortex is centered at the origin and surrounded by a circulating supercurrent. Due to the interaction between the quasiparticle and the vortex, the quasiparticle is scattered into an outgoing radial wave. The situation is depicted schematically in Fig. 4-2(b). By solving the Bogoliubov-de Gennes equation for the quasiparticle wave functions and considering the nature of the quasiparticle current before and after such a scattering event, we will compute the quasiparticle cross section for scattering from a vortex in a d-wave superconductor. Our analysis shall be similar in spirit to that conducted for the s-wave case by Cleary [75, 76], who extended the work of Caroli, de Gennes, and Matricon (on vortex core bound states) to the problem of quasiparticle scattering from a vortex in an s-wave superconductor.

4.4 Bogoliubov-de Gennes Equation

Consider the Bogoliubov-de Gennes (BdG) equation [78] for a d-wave superconductor in the presence of a constant perpendicular magnetic field, $\mathbf{A} = \frac{1}{2}Hr\hat{\phi}$, and with an order parameter that winds once about the origin, $\Delta(\mathbf{r}) = \Delta_0 e^{i\phi}$:

$$H'\Psi = E\Psi \qquad H' = \begin{pmatrix} \hat{H}'_e & \hat{\Delta}' \\ \hat{\Delta}'^* & -\hat{H}'^*_e \end{pmatrix} \tag{4.20}$$

$$\hat{H}'_e = \frac{1}{2m}\left(\mathbf{p} - \frac{e}{c}\mathbf{A}\right)^2 - E_F \tag{4.21}$$

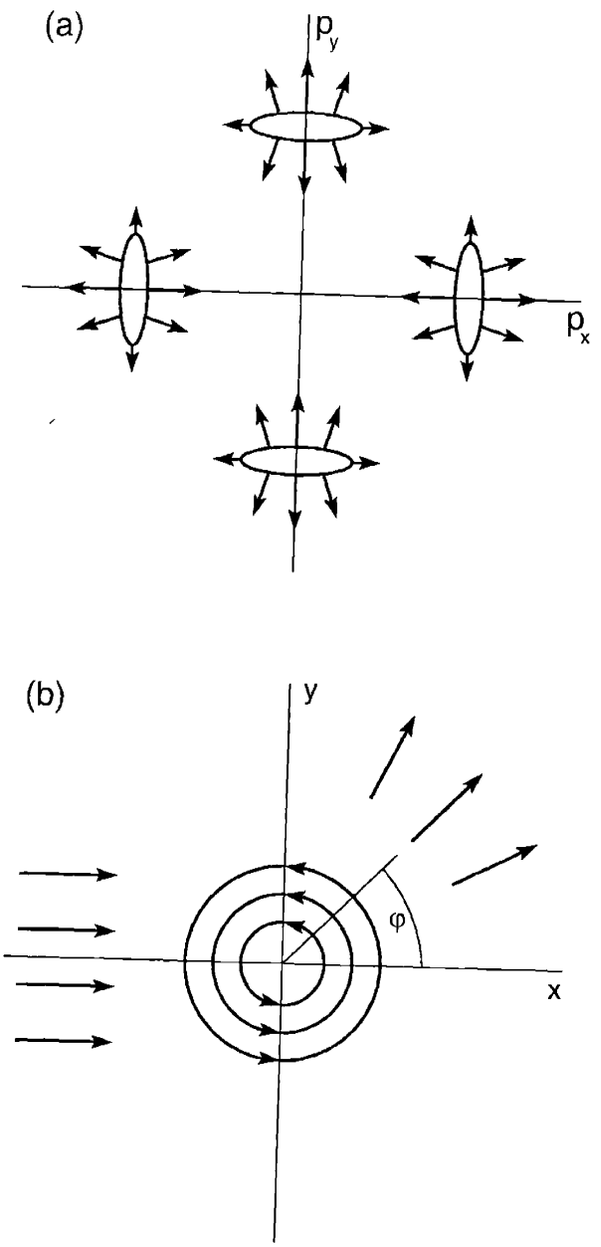

Figure 4-2: Schematic depictions of momentum space and coordinate space. (a) Gap nodes in the Brillouin zone of a CuO_2 layer. Ellipses denote surfaces of equal energy. Arrows represent the quasiparticle group velocity in the vicinity of each node. (b) Quasiparticle scattering from a single vortex. An incident plane wave scatters from an origin-centered vortex into an outgoing radial wave.

$$\hat{\Delta}' = \frac{1}{p_F^2}\{\hat{p_x}, \{\hat{p_y}, \Delta(\mathbf{r})\}\} - \frac{i}{4p_F^2}\Delta(\mathbf{r})(\partial_x\partial_y\phi) \tag{4.22}$$

Here $\mathbf{p} = -i\hbar\nabla$, $\{a, b\} = (ab+ba)/2$, E is the quasiparticle energy, and the form of the gap operator is that required to provide d-wave symmetry [79, 65]. Entangled within the complex differential form of the gap operator, $\hat{\Delta}$, is the fact that upon circling an $hc/2e$ vortex, the quasiparticle acquires a Berry phase factor of (-1). The Hamiltonian would be simplified if we could effectively strip the gap function, $\Delta(\mathbf{r})$, of its phase. This is accomplished via the application of the singular gauge transformation

$$U = \begin{pmatrix} e^{-i\phi/2} & 0 \\ 0 & e^{i\phi/2} \end{pmatrix} \qquad \Phi(\mathbf{r}) = U^{-1}\Psi(\mathbf{r}) \qquad H = U^{-1}H'U. \tag{4.23}$$

In this gauge, known as the Anderson gauge,

$$H\Phi = E\Phi \tag{4.24}$$

$$H = \tau_3\frac{v_f}{2p_F}\left[(\mathbf{p} + \tau_3\mathbf{P}_s)^2 - p_F^2\right] + \tau_1\frac{v_2}{2p_F}\left[2p_xp_y\right] \tag{4.25}$$

where

$$\mathbf{P}_s(\mathbf{r}) = \frac{\hbar}{2}\nabla\phi - \frac{e}{c}\mathbf{A} = \frac{\hbar}{2}\left(\frac{1}{r} - \frac{r}{R^2}\right)\hat{\phi} \tag{4.26}$$

is the gauge invariant superfluid momentum (superflow), $v_f = p_F/m$, $v_2 = \Delta_0/p_F$, and $R \equiv \sqrt{\hbar c/eH}$. Although this form of the Bogoliubov-de Gennes equation is much simplified, the boundary conditions have become more complicated. While the original wave function was defined with periodic boundary conditions, $\Psi(r, \phi) = \Psi(r, \phi + 2\pi)$, the transformed wave function is not single-valued and has antiperiodic boundary conditions, $\Phi(r, \phi) = -\Phi(r, \phi + 2\pi)$. Hence, we have introduced a branch cut such that with each trip around the origin, the wave function changes sign.

In effect, the Berry phase contribution has been extracted from the Hamiltonian and encoded in the antiperiodic boundary conditions imposed on the wave function. This Berry phase effect inherent in the physics of an $hc/2e$ vortex has been dubbed a *vison* by Senthil and Fisher [80]. Note that when considering a system of many vortices, the resulting sea of branch cuts can be problematic. In response, Franz and Tesanovic have recently introduced an alternate gauge transformation better suited to the vortex lattice [81, 79]. However, for the single vortex case that we consider, the Anderson gauge described above is most convenient.

Recall that the low energy excitations of a d-wave superconductor are concentrated about the four nodal points in momentum space where the gap vanishes. We can therefore further simplify our Hamiltonian by shifting the origin of momentum space to the location of one of the nodes. Shifting to node 1

$$p_x \rightarrow p_F + p_x \qquad p_y \rightarrow p_y \tag{4.27}$$

we find that

$$H = H_D + H_C \tag{4.28}$$

$$H_D = v_f \left[p_x \tau_3 + \alpha p_y \tau_1 + P_{sx} \right] \tag{4.29}$$

$$H_C = \frac{v_f}{2p_F} \left[(p^2 + P_s^2)\tau_3 + 2\mathbf{P}_s \cdot \mathbf{p} + \alpha 2 p_x p_y \tau_1 \right] \tag{4.30}$$

where $\alpha = v_2/v_f$ and we have used the fact that $\mathbf{P}_s = P_s(r)\hat{\phi}$ to commute $\mathbf{p}$ with $\mathbf{P}_s$. Here H is written as the sum of a linear (Dirac) Hamiltonian, H_D, and a quadratic (curvature) Hamiltonian, H_C, to emphasize that the second term is smaller than the first by a factor of E/E_F. In what follows we shall seek solutions to the Bogoliubov-de Gennes equation developed above. However, we must first consider the nature of quasiparticle current in a d-wave superconductor.

4.5 Quasiparticle Current

In order to calculate the cross section for a quasiparticle scattering from a vortex, we must be able to write down the currents corresponding to the incident and scattered wave functions. Since the incident and scattered currents will be considered in the far field where the quasiparticles are free, we wish to determine the quasiparticle current as a functional of Φ for $P_s = 0$. Setting $P_s = 0$ in Eq. (4.25) we find that the BdG Hamiltonian becomes

$$H = \begin{pmatrix} \hat{H}_e & \hat{\Delta} \\ \hat{\Delta}^* & -\hat{H}_e^* \end{pmatrix} \qquad \hat{H}_e = -\frac{v_f}{2p_F}\nabla^2 - E_F \qquad \hat{\Delta} = -\frac{v_2}{2p_F} 2\partial_x \partial_y \tag{4.31}$$

Following Ref. [78], we can write down a mean-field Hamiltonian in terms of the real-space electron creation/annihilations operators, $\Psi_\alpha^\dagger$ and Ψ_α.

$$H_{eff} = \int d^2 r \left[\Psi_\uparrow^\dagger \hat{H}_e \Psi_\uparrow + \Psi_\downarrow^\dagger \hat{H}_e \Psi_\downarrow + \hat{\Delta} \Psi_\uparrow^\dagger \Psi_\downarrow^\dagger + \hat{\Delta}^* \Psi_\downarrow \Psi_\uparrow \right] \tag{4.32}$$

Since quasiparticles carry well-defined spin (and heat) the quasiparticle current is equal to the spin current divided by the quasiparticle spin. The spin density operator is expressed as

$$\hat{\rho}^s(\mathbf{r}) = s \left[\Psi_\uparrow^\dagger(\mathbf{r}) \Psi_\uparrow(\mathbf{r}) - \Psi_\downarrow^\dagger(\mathbf{r}) \Psi_\downarrow(\mathbf{r}) \right] \tag{4.33}$$

where $s \equiv 1/2$ and the spin current operator is, in turn, determined via

$$\nabla \cdot \hat{\mathbf{j}}^s(\mathbf{r}) = -\dot{\hat{\rho}}^s = i \left[\hat{\rho}^s(\mathbf{r}), H_{eff} \right]. \tag{4.34}$$

Making use of the fermionic anticommutation relations,

$$\left\{ \Psi_\alpha(\mathbf{r}), \Psi_\beta(\mathbf{r}') \right\} = \left\{ \Psi_\alpha^\dagger(\mathbf{r}), \Psi_\beta^\dagger(\mathbf{r}') \right\} = 0 \qquad \left\{ \Psi_\alpha^\dagger(\mathbf{r}), \Psi_\beta(\mathbf{r}') \right\} = \delta_{\alpha\beta}\delta(\mathbf{r} - \mathbf{r}') \tag{4.35}$$

we find that

$$[\hat{\rho}^s(\mathbf{r}), H_{eff}] = -\frac{s}{2p_F} \sum_\alpha \left[v_f \eta_\alpha \Psi_\alpha^\dagger \nabla^2 \Psi_\alpha + v_2 \Psi_\alpha^\dagger 2\partial_x \partial_y \Psi_{\bar{\alpha}} - \text{h.c.} \right] \tag{4.36}$$

where $\eta_\alpha \equiv \pm 1$. Noting that each of these terms can be manipulated into the form of a divergence and making use of Eq. (4.34) we can write the spin current operator as

$$\hat{\mathbf{j}}^s = \frac{s}{2ip_F} \sum_\alpha \left[v_f \eta_\alpha \Psi_\alpha^\dagger \nabla \Psi_\alpha + v_2 \Psi_\alpha^\dagger \nabla_\perp \Psi_{\bar{\alpha}} - \text{h.c.} \right] \tag{4.37}$$

where $\nabla = \partial_x \hat{\mathbf{x}} + \partial_y \hat{\mathbf{y}}$ and $\nabla_\perp \equiv \partial_y \hat{\mathbf{x}} + \partial_x \hat{\mathbf{y}}$. The real-space creation/annihilation operators, $\Psi_\alpha^\dagger$ and Ψ_α, can be expressed as a weighted sum of Bogoliubov operators, $\gamma_{n\alpha}^\dagger$ and $\gamma_{n\alpha}$, via

$$\Psi_\uparrow(\mathbf{r}) = \sum_n \left(\gamma_{n\uparrow} u_n(\mathbf{r}) - \gamma_{n\downarrow}^\dagger v_n^*(\mathbf{r}) \right) \qquad \Psi_\downarrow(\mathbf{r}) = \sum_n \left(\gamma_{n\downarrow} u_n(\mathbf{r}) + \gamma_{n\uparrow}^\dagger v_n^*(\mathbf{r}) \right) \tag{4.38}$$

where u_n and v_n are particle and hole wave functions for state n. Plugging these forms into the spin current operator and evaluating for state ℓ and spin σ yields an expression for the spin current as a functional of u_ℓ and v_ℓ.

$$\mathbf{j}^s = \langle \ell\sigma | \hat{\mathbf{j}}^s | \ell\sigma \rangle = \frac{s\eta_\sigma}{2ip_F} \left[v_f (u_\ell^* \nabla u_\ell - v_\ell^* \nabla v_\ell) + v_2 (u_\ell^* \nabla_\perp v_\ell + v_\ell^* \nabla_\perp u_\ell) - \text{c.c.} \right] \tag{4.39}$$

Dropping the eigenstate label, dividing by the spin $s\eta_\sigma$, and writing the result in terms of the particle-hole 2-vector

$$\Phi = \begin{pmatrix} u \\ v \end{pmatrix} \qquad \Phi^\dagger = (u^*, v^*) \tag{4.40}$$

we obtain the quasiparticle current

$$\mathbf{j} = \frac{1}{p_F} \text{Im} \left[v_f \Phi^\dagger \tau_3 \nabla \Phi + v_2 \Phi^\dagger \tau_1 \nabla_\perp \Phi \right]. \tag{4.41}$$

As in the preceding section, it is convenient to shift the origin of momentum space to a nodal point. Shifting to node 1 yields

$$\mathbf{j} = \mathbf{j}_D + \mathbf{j}_C \tag{4.42}$$

$$\mathbf{j}_D = v_f \Phi^\dagger (\tau_3 \hat{\mathbf{x}} + \alpha \tau_1 \hat{\mathbf{y}}) \Phi \tag{4.43}$$

$$\mathbf{j}_C = \frac{v_f}{p_F} \text{Im} \left[\Phi^\dagger (\tau_3 \hat{\mathbf{x}} + \alpha \tau_1 \hat{\mathbf{y}}) \frac{\partial \Phi}{\partial x} + \Phi^\dagger (\tau_3 \hat{\mathbf{y}} + \alpha \tau_1 \hat{\mathbf{x}}) \frac{\partial \Phi}{\partial y} \right] \tag{4.44}$$

where $\alpha = v_2/v_f$. Once again, the second (curvature) term is smaller than the first (Dirac) term by a factor of E/E_F.

4.6 Model and Approximations

Given the BdG Hamiltonian and the quasiparticle current functional, we are ready to consider a model of quasiparticle scattering from a single vortex. In reality, each quasiparticle encounters a sea of vortices separated by distances on the order of $2R =$

$\sqrt{4\hbar c/eH}$. The superflow circulating around each vortex is peaked near the vortex centers but falls off slowly and overlaps in the regions between vortices. The total flux through the sample is equal to one ($hc/2e$) flux quantum per vortex but is distributed smoothly since the penetration depth is much larger than the inter-vortex distance. In order to model this situation via single vortex scattering, we approximate the effect of neighboring vortices by cutting off the superflow distribution about our single vortex at a distance R from its center. By construction, the flux through this circle is exactly one flux quantum. Thus, the superfluid momentum takes the form of Eq. (4.26) inside the vortex ($r < R$) and is zero outside the vortex ($r > R$)

$$\mathbf{P}_s(\mathbf{r}) = \frac{\hbar}{2}\left(\frac{1}{r} - \frac{r}{R^2}\right)\theta(R-r)\hat{\phi}. \tag{4.45}$$

Note that at the vortex edge ($r = R$), the phase gradient and vector potential terms cancel and the superflow goes continuously to zero. We shall consider a quasiparticle plane wave incident upon such a vortex and calculate the scattering cross section. Before going forward, however, we make the following additional approximations.

First, recall from Sec. 4.4 that, with our gauge choice, the wave function must obey antiperiodic boundary conditions such that it changes sign each time the quasiparticle winds around the vortex. This is the Berry phase contribution to the problem and it has the interference effect of an Aharonov-Bohm π-flux at the origin. Thus, even in the absence of a superflow, it is possible for quasiparticles to scatter, due solely to the antiperiodic boundary conditions. In the Appendix (Sec. 4.14), we show explicitly that the cross section due only to the Berry phase (with no superflow) is equal to the Aharonov-Bohm cross section for an electron scattering from an enclosed π-flux. However, we note that subtleties associated with the Berry phase contribution to forward scattering serve to complicate the calculation. As a result, in what follows, we neglect the Berry phase effect and instead adopt periodic boundary conditions for the quasiparticle, which is equivalent to considering the case of an hc/e (double) vortex. While the Berry phase does not induce skew scattering on its own, it could modify the effect of the superflow. Thus, while we neglect it here to simplify our analysis, we note that this effect should be considered more carefully in the future.

Second, recall that the quasiparticle excitation spectrum for a d-wave superconductor is that of an anisotropic Dirac cone with two characteristic velocities, v_f and v_2, which can be quite different. This anisotropy enters the BdG equation and current functional in the form of the parameter $\alpha = v_2/v_f$. The fact that α is not equal to one has the effect of complicating the form of the BdG equation in polar coordinates. Thus, in order to make this partial differential equation separable, we should scale out the anisotropy. This can be accomplished by scaling the y-coordinate by a factor of α. In the scaled coordinates, the elliptical gap nodes become circular and we obtain the isotropic Dirac equation. Unfortunately, this scaling also has a negative consequence. Whereas the vortex was originally circular in real space, the scaling makes it elliptical. Thus, in the scaled coordinates, the superfluid momentum (and the vortex boundary) become much more complicated. While such complications can be dealt with (via a significantly more involved computation), they were not considered in this

investigation. For simplicity, rather than scaling out the anisotropy, we consider the more straightforward case where the gap nodes are isotropic and $v_f = v_2$. For this isotropic case, both the gap nodes and the vortex are circular and we can separate the BdG equation in polar coordinates. However, since v_f exceeds v_2 by a factor of 10 to 20 in the cuprates [42], this is clearly an approximation.

Finally, recall that the BdG Hamiltonian can be expressed as the sum of a linearized (Dirac) part, H_D, and a quadratic (curvature) part, H_C. From Eqs. (4.29) and (4.30) we see that H_C is small compared to H_D as long as we are sufficiently far from the vortex center ($r > 1/p_F$). Since we must cutoff our model at the scale of the vortex core ($\xi \sim 10/p_F$), curvature terms can be considered perturbatively. As our final assumption, we select a reasonable core size and model the vortex core as a region with vanishing superflow; which is the best we can do in the absence of further experimental input.

We now have a well-defined scattering problem, which is first solved considering the linearized Hamiltonian, and then perturbed to first order in the curvature terms. Since we shall only consider the isotropic case from this point forward, the Hamiltonian becomes

$$H = H_D + H_C \tag{4.46}$$

$$H_D = v_f \left[\tau_3 p_x + \tau_1 p_y + P_{sx}\right] \tag{4.47}$$

$$H_C = \frac{v_f}{2p_F}\left[\tau_3(p^2 + P_s^2) + 2\mathbf{P}_s \cdot \mathbf{p} + \tau_1(2p_x p_y)\right] \tag{4.48}$$

the quasiparticle energy is

$$E = v_f\sqrt{k_x^2 + k_y^2} = v_f k \tag{4.49}$$

and the quasiparticle current functional takes the form

$$\mathbf{j} = \mathbf{j}_D + \mathbf{j}_C \tag{4.50}$$

$$\mathbf{j}_D = v_f \Phi^\dagger(\tau_3 \hat{\mathbf{x}} + \tau_1 \hat{\mathbf{y}})\Phi \tag{4.51}$$

$$\mathbf{j}_C = \frac{v_f}{p_F}\mathrm{Im}\left[\Phi^\dagger(\tau_3 \hat{\mathbf{x}} + \tau_1 \hat{\mathbf{y}})\frac{\partial \Phi}{\partial x} + \Phi^\dagger(\tau_3 \hat{\mathbf{y}} + \tau_1 \hat{\mathbf{x}})\frac{\partial \Phi}{\partial y}\right]. \tag{4.52}$$

As a result of the above approximations, we cannot expect our results to be quantitatively accurate. However, as we shall see, the qualitative agreement with the experimental results is surprisingly good, which leads us to believe that we have retained the essential physics of the problem.

4.7 Angular Momentum Eigenstates

Consider the linearized Hamiltonian, H_D, in the isotropic limit, Eq. (4.47). Note that for $P_s = 0$, this is just the Dirac Hamiltonian for massless spin-1/2 fermions in two dimensions

$$H_D^0 = v_f[\tau_3 p_x + \tau_1 p_y] = v_f[\alpha \cdot \mathbf{p} + \beta m] \qquad m = 0 \qquad \beta = \gamma^0 \qquad \alpha^i = \gamma^0\gamma^i \tag{4.53}$$

with the γ-matrix representation

$$\gamma^0 = \tau_2 \qquad \gamma^1 = i\tau_1 \qquad \gamma^2 = -i\tau_3 \qquad \rightarrow \qquad \beta = \tau_2 \qquad \alpha^1 = \tau_3 \qquad \alpha^2 = \tau_1 \tag{4.54}$$

For the physical Dirac equation we know that the total angular momentum operator takes the form, $J = L + \frac{1}{2}\Sigma$ where $\Sigma = \frac{i}{2}\epsilon_{3jk}\gamma^j\gamma^k$. Therefore, in the above γ-matrix representation

$$J = L + \frac{\Sigma}{2} = -i\frac{\partial}{\partial\phi} + \frac{\tau_2}{2}. \tag{4.55}$$

Evaluating the commutator with H_D^0 we find (as expected)

$$\left[J, H_D^0\right] = -\tau_2 H_D^0 + \tau_2 H_D^0 = 0. \tag{4.56}$$

Therefore, there exists a complete set of simultaneous eigenstates of H_D^0 and J.

The eigenstates of $L = -i\frac{\partial}{\partial\phi}$ take the form

$$L\Psi = \ell\Psi \qquad \rightarrow \qquad \Psi = e^{i\ell\phi}\begin{pmatrix} a(r) \\ b(r) \end{pmatrix} \tag{4.57}$$

and the eigenstates of $\Sigma = \tau_2$ take the form

$$\Sigma\Psi = \lambda\Psi \qquad \rightarrow \qquad \lambda = \pm 1 \qquad \Psi_+ = c(r,\phi)\begin{pmatrix} 1 \\ i \end{pmatrix} \qquad \Psi_- = d(r,\phi)\begin{pmatrix} 1 \\ -i \end{pmatrix} \tag{4.58}$$

Therefore, the simultaneous eigenstates of J and H_D^0 have the form

$$J\Phi_n = (n + 1/2)\Phi_n \qquad \rightarrow \qquad \Phi_n = f_n(r)e^{in\phi}\begin{pmatrix} 1 \\ i \end{pmatrix} + g_n(r)e^{i(n+1)\phi}\begin{pmatrix} 1 \\ -i \end{pmatrix} \tag{4.59}$$

where the radial functions, $f_n(r)$ and $g_n(r)$, are determined from the solution of a pair of coupled radial equations. Since we have neglected the Berry phase contribution and adopted periodic boundary conditions, the requirement of single-valued wave functions demands that n is an integer.

For $P_s \neq 0$, H_D looks like the massless Dirac equation in the presence of an effective scalar potential, $V = v_f P_{sx} = -v_f P_s(r)\sin\phi$. Since the effective potential is non-central, it mixes angular momentum eigenstates. (See Refs. [82, 83] for a discussion of electron scattering from a similar (dipole) potential.) While the general solution can still be expressed as a linear combination of angular momentum eigenstates

$$\Phi(\mathbf{r}) = \sum_n \left[f_n(r)e^{in\phi}\begin{pmatrix} 1 \\ i \end{pmatrix} + g_n(r)e^{i(n+1)\phi}\begin{pmatrix} 1 \\ -i \end{pmatrix}\right] \tag{4.60}$$

the radial equations for different n are now all coupled together. The inclusion of the curvature terms in the full Hamiltonian, $H = H_D + H_C$, serves to further mix the angular momentum eigenstates. Nonetheless, general solutions can still be written in the form of Eq. (4.60). In the following section, we apply the full Hamiltonian to a

wave function of this form and proceed to determine the resulting radial equations.

4.8 Radial Equations

We shall now plug the general form of our wave function, Eq. (4.60), into the Bogoliubov-de Gennes equation. For this purpose, it is useful to write the BdG Hamiltonian, $H = H_D + H_C$, in polar coordinates. Doing so, we find

$$H_D = -iv_f \left[(\tau \cdot \hat{\mathbf{r}}) \frac{\partial}{\partial r} + \frac{(\tau \cdot \hat{\mathbf{r}})}{r} i\tau_2 \frac{\partial}{\partial \phi} - P_s i \sin\phi \right] \tag{4.61}$$

$$\begin{aligned} H_C = -\frac{v_f}{2p_F} \Bigg[& \left(\frac{\partial^2}{\partial r^2} + \frac{1}{r}\frac{\partial}{\partial r} - P_s^2 \right) \tau_3 + \frac{1}{r^2}\tau_3 \frac{\partial^2}{\partial \phi^2} + i\frac{2P_s}{r}\frac{\partial}{\partial \phi} \\ & + \left(\frac{\partial^2}{\partial r^2} + \frac{1}{r}\frac{\partial}{\partial r} \right) \tau_1 \sin 2\phi - \frac{1}{r^2}\tau_1 \sin 2\phi \frac{\partial^2}{\partial \phi^2} + 2\left(\frac{1}{r}\frac{\partial}{\partial r} - \frac{1}{r^2} \right) \tau_1 \cos 2\phi \frac{\partial}{\partial \phi} \Bigg] \end{aligned} \tag{4.62}$$

where $(\tau \cdot \hat{\mathbf{r}}) \equiv \tau_3 \cos\phi + \tau_1 \sin\phi$ and we note that $(\tau \cdot \hat{\mathbf{r}})^2 = 1$. It is also useful to write the wave function as

$$\Phi(\mathbf{r}) = \sum_n \left[f_n(r)\chi_n^+ + g_n(r)\chi_n^- \right] \tag{4.63}$$

where we have defined

$$\chi_n^+ \equiv e^{in\phi} \begin{pmatrix} 1 \\ i \end{pmatrix} \qquad \chi_n^- \equiv e^{i(n+1)\phi} \begin{pmatrix} 1 \\ -i \end{pmatrix}. \tag{4.64}$$

Note that $(\tau \cdot \hat{\mathbf{r}})$ transforms χ_n^+ into χ_n^- and vice versa,

$$(\tau \cdot \hat{\mathbf{r}})\chi_n^+ = \chi_n^- \qquad (\tau \cdot \hat{\mathbf{r}})\chi_n^- = \chi_n^+, \tag{4.65}$$

and also that cosines and sines shift the χ's up and down in angular momentum,

$$\cos\phi\chi_n^\pm = \frac{\chi_{n+1}^\pm + \chi_{n-1}^\pm}{2} \qquad \sin\phi\chi_n^\pm = \frac{\chi_{n+1}^\pm - \chi_{n-1}^\pm}{2i}. \tag{4.66}$$

Making use of these relations, we see that both $H\Phi$ and $E\Phi$ can be written as sums over $\chi_n^\pm$ weighted by coefficients that are functions only of the radial coordinate. Equating coefficients of $\chi_n^\pm$ on both sides of the BdG equation and dividing out an overall factor of $-iv_f k$ yields a set of fully coupled differential equations for f_n and g_n,

$$\frac{\partial f_n}{\partial \rho} - \left[\frac{n}{\rho} f_n + i g_n + \frac{P_s}{2}(g_{n-1} - g_{n+1}) \right] =$$

$$
\begin{aligned}
&-i\frac{k}{p_F}\left[(n+1)\frac{P_s}{\rho}g_n-\frac{1}{2}\left(\frac{\partial^2}{\partial\rho^2}+\frac{1}{\rho}\frac{\partial}{\partial\rho}-P_s^2-\frac{(n+1)^2}{\rho^2}\right)f_{n+1}\right.\\
&-\frac{1}{4}\left(\frac{\partial^2}{\partial\rho^2}+\frac{1-2n}{\rho}\frac{\partial}{\partial\rho}+\frac{(n-1)(n+1)}{\rho^2}\right)f_{n-1}\\
&\left.+\frac{1}{4}\left(\frac{\partial^2}{\partial\rho^2}+\frac{5+2n}{\rho}\frac{\partial}{\partial\rho}+\frac{(n+1)(n+3)}{\rho^2}\right)f_{n+3}\right] \qquad (4.67)
\end{aligned}
$$

$$
\begin{aligned}
&\frac{\partial g_n}{\partial\rho}-\left[-\frac{n+1}{\rho}g_n+if_n+\frac{P_s}{2}(f_{n-1}-f_{n+1})\right]=\\
&\quad -i\frac{k}{p_F}\left[n\frac{P_s}{\rho}f_n-\frac{1}{2}\left(\frac{\partial^2}{\partial\rho^2}+\frac{1}{\rho}\frac{\partial}{\partial\rho}-P_s^2-\frac{n^2}{\rho^2}\right)g_{n-1}\right.\\
&\quad -\frac{1}{4}\left(\frac{\partial^2}{\partial\rho^2}+\frac{3+2n}{\rho}\frac{\partial}{\partial\rho}+\frac{n(n+2)}{\rho^2}\right)g_{n+1}\\
&\quad \left.+\frac{1}{4}\left(\frac{\partial^2}{\partial\rho^2}+\frac{3-2n}{\rho}\frac{\partial}{\partial\rho}+\frac{n(n-2)}{\rho^2}\right)g_{n-3}\right] \qquad (4.68)
\end{aligned}
$$

where we have defined a dimensionless radial coordinate, $\rho \equiv kr$, and a dimensionless superfluid momentum, $P_s(\rho) \equiv (1/\rho - \rho/(kR)^2)/2$. In this manner, the solution of the BdG equation is reduced to the that of a system of coupled ordinary differential equations. Note that the RHS of each equation is smaller than the LHS by a factor of E/E_F.

4.9 Outside the Vortex

According to our model of the single vortex, the superfluid momentum vanishes at a distance, R, from the origin. Thus, for $\rho > kR$, we sit outside the vortex. Here $P_s = 0$ and the quasiparticles are free. Two of the four curvature terms survive even for $P_s = 0$. However, they are small by a factor of E/E_F and we shall assume that they can be neglected outside the vortex. Thus, for $\rho > kR$, we consider quasiparticles subject only to the free Dirac Hamiltonian, H_D^0, and with current defined via the linearized current functional, $\mathrm{j}_D[\Phi]$. In this regime, it is possible to obtain explicit solutions to the BdG equation, define incident and scattered wave functions, and, by constructing these incident and scattered waves from the free basis functions, write down an expression for the scattering cross section in terms of the coefficients of the basis functions. Then we need only match solutions with those inside the vortex to obtain the cross section.

4.9.1 Free Solutions

For $P_s = 0$ and neglecting curvature terms, the radial equations, (4.67) and (4.68), take the dramatically simpler form

$$\left(\frac{\partial}{\partial\rho} - \frac{n}{\rho}\right) f_n = i g_n \qquad \left(\frac{\partial}{\partial\rho} + \frac{n+1}{\rho}\right) g_n = i f_n. \tag{4.69}$$

Note in particular that, while f_n is coupled to g_n, the equations for functions of different n are independent. Eliminating g_n from the equations above yields

$$\left[\frac{\partial^2}{\partial\rho^2} + \frac{1}{\rho}\frac{\partial}{\partial\rho} + \left(1 - \frac{n^2}{\rho^2}\right)\right] f_n = 0 \tag{4.70}$$

which is the defining equation for the Bessel functions. Therefore,

$$f_n(\rho) = A_n J_n(\rho) + B_n Y_n(\rho) \tag{4.71}$$

where A_n and B_n are complex constants and $J_n(\rho)$ and $Y_n(\rho)$ are Bessel functions of the first and second kind. Substituting back for g_n then yields

$$g_n(\rho) = i A_n J_{n+1}(\rho) + i B_n Y_{n+1}(\rho) \tag{4.72}$$

where we have used the Bessel function identity $(\partial/\partial\rho - \nu/\rho) Z_\nu = -Z_{\nu+1}$. Hence, we can write down the free wave function

$$\Phi(\mathbf{r}) = \sum_n \left[(A_n J_n + B_n Y_n) e^{in\phi} \begin{pmatrix} 1 \\ i \end{pmatrix} + i(A_n J_{n+1} + B_n Y_{n+1}) e^{i(n+1)\phi} \begin{pmatrix} 1 \\ -i \end{pmatrix}\right] \tag{4.73}$$

where the coefficients shall remain undetermined until we match with solutions inside the vortex.

4.9.2 Incident and Scattered Waves

We wish to obtain the cross section for a plane wave, with quasiparticle current in the incident direction, scattering off a vortex as a radial wave, with quasiparticle current in the scattered direction. If the incident momentum is $\mathbf{k} = (k, \theta)$ and the final momentum is $\mathbf{k}' = (k, \phi)$, then the incident direction is the direction of the group velocity at momentum $\mathbf{k}$ and the scattered direction is the direction of the group velocity at momentum $\mathbf{k}'$. For general, anisotropic nodes, the group velocity need not be parallel to the momentum. However, for the isotropic case that we consider

$$\mathbf{v}_G(\mathbf{k}) = \frac{\partial E_k}{\partial \mathbf{k}} = v_f \frac{\epsilon_k}{E_k}\hat{\mathbf{x}} + v_2 \frac{\Delta_k}{E_k}\hat{\mathbf{y}} = v_f\left(\cos\theta\hat{\mathbf{x}} + \sin\theta\hat{\mathbf{y}}\right) = v_f\hat{\mathbf{k}} \tag{4.74}$$

and the group velocity and momentum are parallel. Therefore, if Φ_i denotes the incident wave function and Φ_s denotes the scattered wave function, then we require

$$\mathbf{j}_D[\Phi_i] \sim (\cos\theta\hat{\mathbf{x}} + \sin\theta\hat{\mathbf{y}}) \sim \hat{\mathbf{k}} \qquad \mathbf{j}_D[\Phi_s] \sim (\cos\phi\hat{\mathbf{x}} + \sin\phi\hat{\mathbf{y}}) \sim \hat{\mathbf{k}}' \sim \hat{\mathbf{r}}. \tag{4.75}$$

Inspection of the form of the current functional, $\mathbf{j}_D = v_f\Phi^\dagger(\tau_3\hat{\mathbf{x}} + \tau_1\hat{\mathbf{y}})\Phi$ reveals that the appropriate incident plane wave is

$$\Phi_i(\mathbf{r}) = e^{i\mathbf{k}\cdot\mathbf{r}}\begin{pmatrix}\cos\frac{\theta}{2}\\ \sin\frac{\theta}{2}\end{pmatrix} \tag{4.76}$$

since

$$\mathbf{j}_D[\Phi_i] = v_f\left[\left(\cos^2\frac{\theta}{2} - \sin^2\frac{\theta}{2}\right)\hat{\mathbf{x}} + \left(2\sin\frac{\theta}{2}\cos\frac{\theta}{2}\right)\hat{\mathbf{y}}\right] = v_f\hat{\mathbf{k}}. \tag{4.77}$$

Note also that this form solves the BdG equation, as it must in the absence of the vortex. The appropriate scattered radial wave is then

$$\Phi_s(\mathbf{r}) = e^{i\frac{\phi}{2}}f(\phi-\theta)\frac{e^{ikr}}{\sqrt{r}}\begin{pmatrix}\cos\frac{\phi}{2}\\ \sin\frac{\phi}{2}\end{pmatrix} \tag{4.78}$$

since

$$\mathbf{j}_D[\Phi_s] = v_f\frac{|f|^2}{r}\left[\left(\cos^2\frac{\phi}{2} - \sin^2\frac{\phi}{2}\right)\hat{\mathbf{x}} + \left(2\sin\frac{\phi}{2}\cos\frac{\phi}{2}\right)\hat{\mathbf{y}}\right] = v_f\frac{|f|^2}{r}\hat{\mathbf{r}}. \tag{4.79}$$

Here $f(\phi-\theta)$ is the scattering amplitude and the $e^{i\phi/2}$ prefactor has been added to make the wave function single-valued.

4.9.3 Constructing the Cross Section

We shall now construct, from our free solution basis functions, an asymptotic wave function containing the correct incident and scattered waves. The factor in front of the scattered wave will then be our scattering amplitude.

We begin with the free wave function obtained in Eq. (4.73). Note that in the asymptotic limit, the integer-index Bessel functions can be expressed as

$$J_n(\rho) = \eta_n\sqrt{\frac{2}{\pi\rho}}\cos(\rho - \pi/4 - |n|\pi/2) \qquad Y_n(\rho) = \eta_n\sqrt{\frac{2}{\pi\rho}}\sin(\rho - \pi/4 - |n|\pi/2) \tag{4.80}$$

where $\eta_n = 1$ for $n \geq 0$ and $\eta_n = (-1)^n$ for $n < 0$. Therefore, if we shift $n \to n-1$ in the second term of Eq. (4.73), plug in the asymptotic forms, and decompose the sines and cosines into exponentials, we obtain

$$\Phi = \sum_n e^{in\phi}\sqrt{\frac{2}{\pi\rho}}\frac{\eta_n}{2}\left[\left((A_n - iB_n)e^{i(\rho-\frac{\pi}{4}-\frac{\pi}{2}|n|)} + (A_n + iB_n)e^{-i(\rho-\frac{\pi}{4}-\frac{\pi}{2}|n|)}\right)\begin{pmatrix}1\\ i\end{pmatrix}\right.$$

$$+\left(i(A_{n-1}-iB_{n-1})e^{i(\rho-\frac{\pi}{4}-\frac{\pi}{2}|n|)}+i(A_{n-1}+iB_{n-1})e^{-i(\rho-\frac{\pi}{4}-\frac{\pi}{2}|n|)}\right)\begin{pmatrix}1\\-i\end{pmatrix}\Bigg]. \tag{4.81}$$

We can replace our two complex constants, A_n and B_n, with two new complex constants, a_n and b_n, by defining

$$A_n - iB_n \equiv i^n e^{-i(n+\frac{1}{2})\theta}\left(1/2 + e^{i\frac{\pi}{4}}b_n\right) \tag{4.82}$$

$$A_n + iB_n \equiv i^n e^{-i(n+\frac{1}{2})\theta}\left(1/2 + e^{i\frac{\pi}{4}}(-1)^n a_n\right). \tag{4.83}$$

Making use of these definitions, noting that $\eta_n i^n = i^{|n|}$, and reorganizing terms, we find

$$\Phi = \sum_n i^n e^{in(\phi-\theta)}\eta_n\sqrt{\frac{2}{\pi\rho}}\cos(\rho-\pi/4-|n|\pi/2)\frac{1}{2}\left[e^{-i\frac{\theta}{2}}\begin{pmatrix}1\\i\end{pmatrix}+e^{i\frac{\theta}{2}}\begin{pmatrix}1\\-i\end{pmatrix}\right]$$
$$+\sum_n e^{in(\phi-\theta)}\sqrt{\frac{2}{\pi\rho}}\frac{1}{2}\left[\left(b_n e^{i\rho}+a_n e^{-i\rho}\right)e^{-i\frac{\theta}{2}}\begin{pmatrix}1\\i\end{pmatrix}+\left(b_{n-1}e^{i\rho}-a_{n-1}e^{-i\rho}\right)e^{i\frac{\theta}{2}}\begin{pmatrix}1\\-i\end{pmatrix}\right] \tag{4.84}$$

Noting the Bessel function expansion of a plane wave

$$e^{i\rho\cos(\phi-\theta)} = \sum_n i^n J_n(\rho)e^{in(\phi-\theta)} = \sum_n i^n e^{in(\phi-\theta)}\eta_n\sqrt{\frac{2}{\pi\rho}}\cos(\rho-\pi/4-|n|\pi/2) \tag{4.85}$$

and shifting $n \to n+1$ in the final term of Eq. (4.84) yields

$$\Phi = e^{i\mathbf{k}\cdot\mathbf{r}}\begin{pmatrix}\cos\frac{\theta}{2}\\ \sin\frac{\theta}{2}\end{pmatrix}+\sqrt{\frac{2}{\pi\rho}}e^{i(\phi-\theta)/2}\sum_n e^{in(\phi-\theta)}\left[b_n e^{i\rho}\begin{pmatrix}\cos\frac{\phi}{2}\\ \sin\frac{\phi}{2}\end{pmatrix}+a_n e^{-i\rho}\begin{pmatrix}-i\sin\frac{\phi}{2}\\ i\cos\frac{\phi}{2}\end{pmatrix}\right] \tag{4.86}$$

Regrouping terms and defining $\varphi \equiv \phi - \theta$, this becomes

$$\Phi = e^{i\mathbf{k}\cdot\mathbf{r}}\begin{pmatrix}\cos\frac{\theta}{2}\\ \sin\frac{\theta}{2}\end{pmatrix}+e^{i\frac{\varphi}{2}}\left[f(\varphi)\frac{e^{ikr}}{\sqrt{r}}\begin{pmatrix}\cos\frac{\phi}{2}\\ \sin\frac{\phi}{2}\end{pmatrix}+ig(\varphi)\frac{e^{-ikr}}{\sqrt{r}}\begin{pmatrix}-\sin\frac{\phi}{2}\\ \cos\frac{\phi}{2}\end{pmatrix}\right] \tag{4.87}$$

where

$$f(\varphi) \equiv \sqrt{\frac{2}{\pi k}}\sum_n b_n e^{in\varphi} \tag{4.88}$$

$$g(\varphi) \equiv \sqrt{\frac{2}{\pi k}}\sum_n a_n e^{in\varphi}. \tag{4.89}$$

Since we have yet to restrict a_n and b_n, this asymptotic wave function is still totally general. However, we have succeeded in rearranging it into a suggestive form. The three terms above are easily understood. The first is our incident plane wave, the second is the outgoing radial wave, and the third is an incoming radial wave. By

construction, we require an incident plane wave and an outgoing radial wave. To realize this scenario, our asymptotic boundary conditions require that there be no additional incoming wave. Thus, we require $g(\varphi) = 0$ and must therefore set $a_n = 0$ for all n. In terms of our original constants, this restriction requires that

$$B_n = i\left(A_n - A_n^0\right) \qquad A_n^0 \equiv \tfrac{1}{2} i^n e^{-i(n+\frac{1}{2})\theta} \tag{4.90}$$

and sets

$$b_n = e^{-i\frac{\pi}{4}}\left(\frac{A_n}{A_n^0} - 1\right). \tag{4.91}$$

Furthermore, we obtain a simple form for the asymptotic wave function

$$\Phi(\mathbf{r}) = e^{i\mathbf{k}\cdot\mathbf{r}}\begin{pmatrix}\cos\frac{\theta}{2}\\ \sin\frac{\theta}{2}\end{pmatrix} + e^{i\frac{\varphi}{2}} f(\varphi)\frac{e^{ikr}}{\sqrt{r}}\begin{pmatrix}\cos\frac{\phi}{2}\\ \sin\frac{\phi}{2}\end{pmatrix} \tag{4.92}$$

where we recall that $\mathbf{k} = (k, \theta)$, $\mathbf{r} = (r, \phi)$, and $\varphi = \phi - \theta$.

Applying the current functional, $\mathbf{j}_D$, to both the incident and scattered parts of this wave function yields the incident and scattered current density

$$\mathbf{j}_i = \mathbf{j}_D[\Phi_i] = v_f\hat{\mathbf{k}} \qquad \mathbf{j}_s = \mathbf{j}_D[\Phi_s] = v_f\frac{|f(\varphi)|^2}{r}\hat{\mathbf{r}}. \tag{4.93}$$

Then the differential cross section is

$$\frac{d\sigma}{d\varphi} = \frac{\mathbf{j}_s\cdot\mathbf{r}}{|\mathbf{j}_i|} = |f(\varphi)|^2. \tag{4.94}$$

Integrating over φ yields the total cross section

$$\sigma = \int_{-\pi}^{\pi} d\varphi\,\frac{d\sigma}{d\varphi} = \frac{4}{k}\sum_n |b_n|^2. \tag{4.95}$$

By weighting with a factor of $(1 - \cos\varphi)$, we obtain the transport cross section

$$\sigma_{\|} = \int_{-\pi}^{\pi} d\varphi\,\frac{d\sigma}{d\varphi}(1-\cos\varphi) = \frac{4}{k}\sum_n b_n\left[b_n - (b_{n+1} + b_{n-1})/2\right]^* \tag{4.96}$$

and by weighting with a factor of $\sin\varphi$ we find the the skew cross section

$$\sigma_{\perp} = \int_{-\pi}^{\pi} d\varphi\,\frac{d\sigma}{d\varphi}\sin\varphi = \frac{2}{ik}\sum_n b_n\left[b_{n+1} - b_{n-1}\right]^*. \tag{4.97}$$

All that remains is to calculate the coefficients b_n. These, of course, are determined by the details of the quasiparticle scattering. Hence, we must now look inside the vortex.

4.10 Inside the Vortex

Inside the vortex, the situation is more complicated. For $\rho < kR$, the superfluid momentum is nonzero and takes the form, $P_s = (1/\rho - \rho/(kR)^2)/2$. Therefore, even the linearized Hamiltonian, H_D, mixes angular momentum eigenstates. As before, the curvature term, H_C, is small by a factor of E/E_F. Thus, it is tempting to neglect the curvature and work only with the linearized equations. This is justified if we are only interested in the transport cross section, $\sigma_{||}$. However, since we are also interested in the skew cross section, $\sigma_\perp$, the linearized equations are insufficient. As discussed by Simon and Lee [65], Ye [71], and Vishwanath [72], since the linearized Hamiltonian is time-reversal invariant, the resulting skew cross section (after summing over all four nodes) is zero. Therefore, the physical skew cross section is a direct consequence of curvature. Hence, we cannot neglect H_C. Rather, we shall include the curvature terms perturbatively to first order in E/E_F. We can therefore solve for the radial functions, $f_n(\rho)$ and $g_n(\rho)$ via a two-step procedure. In the first iteration, we shall neglect curvature all together, solving Eqs. (4.67) and (4.68) with the RHS set to zero. This yields the 0th order solutions, $f_n^0(\rho)$ and $g_n^0(\rho)$. In the second iteration we shall evaluate the curvature terms using these 0th order functions and solve for $f_n(\rho)$ and $g_n(\rho)$ to first order in the curvature. Hence, the radial equations look as follows:

$$\frac{\partial f_n}{\partial \rho} - \left[\frac{n}{\rho} f_n + i g_n + \frac{P_s}{2}(g_{n-1} - g_{n+1})\right] = q_n^f(\rho) \tag{4.98}$$

$$\frac{\partial g_n}{\partial \rho} - \left[-\frac{n+1}{\rho} g_n + i f_n + \frac{P_s}{2}(f_{n-1} - f_{n+1})\right] = q_n^g(\rho) \tag{4.99}$$

In our first iteration, $q_n^f(\rho)$ and $q_n^g(\rho)$ are set to zero. In the second iteration, these functions are set equal to the RHS of Eqs. (4.67) and (4.68) evaluated using the results of the first iteration.

Since the radial equations are fully coupled by the superfluid momentum terms, the equations for all n should be solved simultaneously via an infinite-dimensional matrix equation. By numerical necessity, we shall cut off the coupling at some large n such that we consider a total of N angular momentum eigenstates where $-\frac{N}{2} \leq n \leq \frac{N}{2} - 1$. This is physically reasonable as we do not expect very large angular momenta to have a significant effect on the low energy physics. The result is a $2N \times 2N$ matrix differential equation

$$\frac{d\mathbf{z}}{d\rho} = \mathbf{M}(\rho)\mathbf{z} + \mathbf{q}(\rho) \tag{4.100}$$

where $\mathbf{z}(\rho)$ is a $2N$-component vector containing the f_n's and the g_n's, $\mathbf{M}(\rho)$ is a $2N \times 2N$ matrix, and $\mathbf{q}(\rho)$ is a $2N$-component vector containing the q_n^f's and the q_n^g's. Since only neighboring angular momenta are coupled, $\mathbf{M}(\rho)$ is a rather sparse matrix. Furthermore, due to the form of Eqs. (4.98) and (4.99) and the simple ρ-dependence of the superfluid momentum, this matrix can be written as

$$\mathbf{M}(\rho) = \mathbf{B}\frac{1}{\rho} + \mathbf{A}_0 + \mathbf{A}_1\rho \tag{4.101}$$

where $\mathbf{B}$, $\mathbf{A}_0$, and $\mathbf{A}_1$ are constant $2N \times 2N$ matrices. In terms of this matrix notation, our procedure will be to solve the homogenous equation ($\mathbf{q} = 0$) for the 0th order solution, plug the results into $\mathbf{q}(\rho)$, and then calculate the particular integral to yield solutions to 1st order in E/E_F.

4.10.1 Homogeneous Solutions via Method of Frobenius

Consider the homogeneous equation

$$\frac{d\mathbf{z}}{d\rho} = \mathbf{M}(\rho)\mathbf{z} \qquad \rightarrow \qquad \rho\frac{d\mathbf{z}}{d\rho} = \left(\mathbf{B} + \mathbf{A}_0\rho + \mathbf{A}_1\rho^2\right)\mathbf{z} \tag{4.102}$$

Since $\mathbf{M}(\rho)$ diverges as $1/\rho$ at the origin, the equation has a regular singular point at $\rho = 0$. Thus, its solution requires local analysis about the origin. In particular, we shall employ a matrix generalization of what is known as the Method of Frobenius [84].

Consider a solution of the (Frobenius) form

$$\mathbf{z} = \sum_{m=0}^{\infty} \mathbf{a}_m \rho^{\alpha+m} \tag{4.103}$$

where α is a complex number and $\mathbf{a}_m$ is a vector coefficient for each integer m. Plugging this into our differential equation yields

$$\sum_{m=0}^{\infty} \left[(\mathbf{B} - (\alpha+m))\,\mathbf{a}_m\rho^{\alpha+m} + \mathbf{A}_0\mathbf{a}_m\rho^{\alpha+m+1} + \mathbf{A}_1\mathbf{a}_m\rho^{\alpha+m+2}\right] = 0. \tag{4.104}$$

Shifting $m \rightarrow m-1$ for the $\mathbf{A}_0$ term, shifting $m \rightarrow m-2$ for the $\mathbf{A}_1$ term, and noting that the total coefficient of each power of ρ must equal zero, we obtain the following equations:

$$(\mathbf{B} - \alpha)\,\mathbf{a}_0 = 0 \tag{4.105}$$

$$(\mathbf{B} - (\alpha+1))\,\mathbf{a}_1 = -\mathbf{A}_0\mathbf{a}_0 \tag{4.106}$$

$$(\mathbf{B} - (\alpha+m))\,\mathbf{a}_m = -\mathbf{A}_0\mathbf{a}_{m-1} - \mathbf{A}_1\mathbf{a}_{m-2} \qquad m = 2, 3, 4, \ldots \tag{4.107}$$

Note that Eq. (4.105) is just the eigenvalue equation for $\mathbf{B}$. It is solved if α is an eigenvalue of $\mathbf{B}$ and $\mathbf{a}_0$ is the corresponding eigenvector. This eigensystem has $2N$ solutions which we can label α_k and $\mathbf{a}_0^k$ for $k = 1 \ldots 2N$. The other two equations, (4.106) and (4.107), define matrix recursion relations. If $\mathbf{B} - (\alpha_k + m)\mathbb{1}$ is non-singular for $m = 1, 2, 3, \ldots$, then we can solve these equations to obtain $\mathbf{a}_m^k$ given $\mathbf{a}_0^k$ and α_k. This condition will always be satisfied for the largest eigenvalue of $\mathbf{B}$ but will fail for any α_k for which $\alpha_k + m$ is also an eigenvalue of $\mathbf{B}$. In general, this circumstance would require additional solutions not of the Frobenius form. Fortunately, for $P_s \neq 0$, the eigenvalues of $\mathbf{B}$ are separated by non-integer numbers. Therefore, we can obtain $2N$ solutions of the Frobenius form

$$\mathbf{z}^k = \sum_{m=0}^{m_{\max}} \mathbf{a}_m^k \rho^{\alpha_k+m} \qquad k = 1 \ldots 2N \tag{4.108}$$

and use the equations above to calculate the vector coefficients recursively. Due to the constraints of our numerics, we cutoff each series at $m = m_{\max}$. As such series represent expansions about the origin, the more terms we include the larger the ρ at which the solutions will be valid. Since the differential equation contains no singular points besides the origin, the solution can be pushed as far from the origin as necessary by including additional terms. Since our solutions need only be valid out to the edge of the vortex, $\rho = kR$, we shall cutoff each series at the $m_{\max}$ for which the solutions are valid out to kR.

4.10.2 Boundary Condition at Origin

Although all $2N$ solutions, $\mathbf{z}^k$, satisfy the homogeneous equation (4.102), we must reject solutions that show unphysical behavior at the origin. While it is permissible for the wave function or the current density to diverge at the origin, we must require that observable quantities like the total probability at the origin and the total current passing through the origin be well behaved. Since solutions of the Frobenius form yield contributions to the wave function of the form $\Phi(\rho \to 0) \sim \rho^\alpha$ for small ρ, we seek conditions on the allowed values of α.

Consider a circle of radius $\epsilon \to 0$ about the origin. The total quasiparticle probability within the circle is

$$\text{Prob} = \int^{\epsilon} d^2\rho\, \Phi^\dagger(\rho \to 0)\Phi(\rho \to 0) \sim \int_0^{\epsilon} (\rho d\rho)\, \rho^\alpha \rho^\alpha \sim \int_0^{\epsilon} d\rho\, \rho^{2\alpha+1}. \tag{4.109}$$

If the origin is to be just like any other point in space, then this probability must vanish as $\epsilon \to 0$. Hence, we require $\alpha > -1$. While this restricts the allowed solutions, it turns out that the quasiparticle current provides a more restrictive condition.

Now consider a semicircle of radius $\epsilon \to 0$ about the origin, oriented about the $\hat{\theta}$ direction. The total current passing though such a semicircle in the $\hat{\theta}$ direction is

$$I_\theta = \int_{\theta-\pi/2}^{\theta+\pi/2} (\epsilon d\phi)\, v_f \Phi^\dagger(\rho \to 0)(\tau_3 \hat{\mathbf{x}} + \tau_1 \hat{\mathbf{y}})\Phi(\rho \to 0) \cdot \hat{\theta} \sim \epsilon \epsilon^\alpha \epsilon^\alpha \sim \epsilon^{2\alpha+1}. \tag{4.110}$$

For the origin to be physical, this current must vanish as $\epsilon \to 0$. Hence, we require $\alpha \geq -1/2$. (Note that the special case of $\alpha = -1/2$ requires additional consideration. See the Appendix (Sec. 4.14) for details.)

For $P_s \neq 0$, the eigenvalues of $\mathbf{B}$ are always such that N of them are strictly larger than $-1/2$ and N of them are strictly smaller than $-1/2$. Thus, in order to satisfy these boundary conditions at the origin, we shall keep only the N solutions, $\mathbf{z}^k$, for which $\alpha_k > -1/2$. The full solution to the homogeneous equation is then

$$\mathbf{z}(\rho) = \sum_{k=1}^{N} c_k \mathbf{z}^k(\rho) \tag{4.111}$$

where the c_k are N complex coefficients to be determined via solution matching at the edge of the vortex.

4.10.3 Particular Integral via Variation of Parameters

The next step is to require that our radial solutions are continuous across the edge of the vortex. More details of this solution matching are discussed in Sec. 4.11. For now it suffices to say that this condition determines the N outside-vortex coefficients, A_n, as well as the N inside-vortex coefficients, c_k. Given the c_k, Eq. (4.111) yields the 0th order (in curvature) solutions, f_n^0 and g_n^0, and our first iteration is complete. Plugging these solutions into the curvature terms yields the "forcing function", $\mathbf{q}(\rho)$, and we can proceed to calculate the particular integral of the inhomogeneous differential equation

$$\frac{d\mathbf{z}}{d\rho} = \mathbf{M}\mathbf{z} + \mathbf{q}. \tag{4.112}$$

To do so we shall employ a matrix generalization of the method of Variation of Parameters [85]. Given the $2N$ homogeneous solutions obtained in Sec. 4.10.1 (both the convergent ones and the divergent ones) we can construct a $2N \times 2N$ fundamental matrix

$$\mathbf{X} \equiv \left[\begin{pmatrix} \\ \mathbf{z}^1 \\ \\ \end{pmatrix} \begin{pmatrix} \\ \mathbf{z}^2 \\ \\ \end{pmatrix} \cdots \begin{pmatrix} \\ \mathbf{z}^{2N} \\ \\ \end{pmatrix} \right] \tag{4.113}$$

which satisfies

$$\frac{d\mathbf{X}}{d\rho} = \mathbf{M}\mathbf{X}. \tag{4.114}$$

Defining $\mathbf{v}$ and $\mathbf{u}$ such that $\mathbf{z} = \mathbf{X}\mathbf{v}$ and $\mathbf{u} = d\mathbf{v}/d\rho$ we note that

$$\frac{d\mathbf{z}}{d\rho} = \frac{d\mathbf{X}}{d\rho}\mathbf{v} + \mathbf{X}\frac{d\mathbf{v}}{d\rho} = \mathbf{M}\mathbf{X}\mathbf{v} + \mathbf{X}\mathbf{u} = \mathbf{M}\mathbf{z} + \mathbf{X}\mathbf{u} \tag{4.115}$$

which means that $\mathbf{u} = \mathbf{X}^{-1}\mathbf{q}$ and therefore

$$\mathbf{z}(\rho) = \mathbf{X}(\rho)\left[\mathbf{c} + \int_{\rho_0}^{\rho} d\rho'\, \mathbf{X}^{-1}(\rho')\,\mathbf{q}(\rho')\right] \tag{4.116}$$

where $\mathbf{c}$ is a constant vector and ρ_0 is a constant. Clearly, the first term is a linear combination of the homogeneous solutions and the second is the particular integral.

Once again, we must require that our solution be well behaved at the origin. Since the particular integral can also be divergent at the origin, the easiest way to do this is to set $\rho_0 = 0$ such that the particular integral is zero at $\rho = 0$. Then $\mathbf{c}$ can simply be restricted such that only the first N components (the ones multiplying well-behaved homogeneous solutions) are nonzero. But with this choice, the integrand diverges at $\rho' = 0$. This is a consequence of the fact that the curvature terms are only small (and our perturbation theory is only valid) for $r > 1/p_F$. That is, for distances larger than the lattice spacing. Yet before we reach the scale of the lattice spacing, the supercurrent will have already exceeded the critical current at some core size, ξ. Since the nature of the vortex core in the cuprates is still uncertain, we shall not attempt to include vortex core physics in our model. Our expectation, however, is that thermal transport will not be strongly core-dependent. We shall therefore simply

cutoff our theory at $r = \xi$ and assume that the superflow shuts off inside the vortex core. With this approximation, we set the lower bound of our integration at $\rho_0 = k\xi$. For sufficiently small ξ (as is physical for the cuprates), it is still approximately correct to neglect the lower half of the c-vector, retaining only the components which multiply homogeneous solutions that are well-behaved at the origin. Our solutions then take the form

$$\mathbf{z}(\rho) = \sum_{k=1}^{N} c_k \mathbf{z}^k(\rho) + \mathbf{Z}(\rho) \tag{4.117}$$

where

$$\mathbf{Z}(\rho) = \mathbf{X}(\rho) \int_{k\xi}^{\rho} d\rho' \, \mathbf{X}^{-1}(\rho') \, \mathbf{q}(\rho') \tag{4.118}$$

and the $\mathbf{z}^k$ are restricted to the ones that are well behaved at the origin. By matching the above (1st order in curvature) inside-vortex radial solutions to the outside-vortex solutions, we can obtain coefficient values valid to 1st order in E/E_F.

By necessity, we have introduced an additional length scale, ξ, into the problem. As the physical core size is not an easily accessible quantity, any dependence of our results on ξ is a source of uncertainty. However, we find that while our quantitative calculations have some dependence on our choice of core size, the qualitative nature of our results is unaffected.

4.11 Four-Node Cross Section

For $\rho > kR$, we found $2N$ radial solutions (Bessel functions) and reduced the $2N$ coefficients (A_n,B_n) to N coefficients with the condition that there be no incident radial wave in the asymptotic limit. (This required $B_n = i(A_n - A_n^0)$.) For $\rho < kR$, we found $2N$ radial solutions (Frobenius series plus particular integral) and reduced the $2N$ coefficients to N coefficients with the condition that the solutions be well-behaved at the origin. (This required $c_k = 0$ for $\alpha_k < -\frac{1}{2}$.) At $\rho = kR$, all $2N$ radial solutions must be continuous. (Note that since the Dirac equation is 1st order, only continuity is required, while for the 2nd order Schrodinger equation, differentiability would also be required.) Thus, we have $2N$ equations which can be solved for the remaining $2N$ coefficients by matching solutions at $\rho = kR$. We solve the resulting $2N \times 2N$ matrix equation via LU decomposition to obtain c_k for $1 \leq k \leq N$ and A_n for $-\frac{N}{2} \leq n \leq \frac{N}{2} - 1$.

As discussed in prior sections, solutions are matched twice: first with no particular integral to obtain the 0th order coefficients and then including the particular integral to obtain the 1st order coefficients. After the second iteration, we use Eq. (4.91) to find b_n from A_n and then plug the b_n into Eqs. (4.94), (4.95), (4.96), and (4.97) to obtain the differential, total, transport, and skew cross sections.

Recall that at the outset of this calculation, we shifted the origin of momentum space to the center of node 1. Thus, in the discussions that followed, we have been considering quasiparticles scattered from one state in the vicinity of node 1 to another state in the vicinity of node 1. The resulting cross section is therefore only the cross section for these node-1 quasiparticles. However, given a quasiparticle current in

any particular direction, quasiparticles from all four nodes will contribute equally. Thus to obtain the physical cross section, we must average over the cross sections for quasiparticles at each of the four nodes.

Our results for node 1 can be easily generalized to node $j = \{1, 2, 3, 4\}$ by transforming coordinates to those appropriate to node j. In accordance with the d-wave structure of the gap, we can define a local coordinate system at each of the four nodes with a $\hat{\mathbf{k}}_1$ axis pointing along the direction of increasing ϵ_k and a $\hat{\mathbf{k}}_2$ axis pointing along the direction of increasing Δ_k. Note that while nodes 1 and 3 define right-handed coordinate systems, nodes 2 and 4 define left-handed coordinate systems. We can therefore transform from node 1 to node j simply by rotating our incident and scattered angles (θ and ϕ) and then changing the sign of these angles to account for the handedness of the local coordinate system.

$$\begin{array}{lllll} \text{Node 1:} & \theta_1 = \theta & \phi_1 = \phi & \varphi_1 = \phi_1 - \theta_1 = \varphi \\ \text{Node 2:} & \theta_2 = -(\theta - \frac{\pi}{2}) & \phi_2 = -(\phi - \frac{\pi}{2}) & \varphi_2 = \phi_2 - \theta_2 = -\varphi \\ \text{Node 3:} & \theta_3 = \theta + \pi & \phi_3 = \phi + \pi & \varphi_3 = \phi_3 - \theta_3 = \varphi \\ \text{Node 4:} & \theta_4 = -(\theta + \frac{\pi}{2}) & \phi_4 = -(\phi + \frac{\pi}{2}) & \varphi_4 = \phi_4 - \theta_4 = -\varphi \end{array} \tag{4.119}$$

Thus, to obtain results for quasiparticles about node j, we need only input each θ_j and take the output as a function of $(-1)^{j+1}\varphi$. Then the physical cross sections are

$$\frac{d\sigma}{d\varphi} = \frac{1}{4}\sum_{j=1}^{4}\left(\frac{d\sigma}{d\varphi}\right)_j \qquad \sigma = \frac{1}{4}\sum_{j=1}^{4}\sigma^j \qquad \sigma_{\|} = \frac{1}{4}\sum_{j=1}^{4}\sigma_{\|}^j \qquad \sigma_{\perp} = \frac{1}{4}\sum_{j=1}^{4}\sigma_{\perp}^j \tag{4.120}$$

Note that we do not account for quasiparticles that are scattered from one node to another. However, since the effective potential (induced by the superflow) is smooth on the scale of $1/p_F$, the Fourier components for large-momentum inter-node scattering will be small. Hence, it is reasonable to neglect such contributions.

4.12 Results

The procedure outlined in the preceding sections was implemented numerically for a range of intervortex distances, $kR = \gamma T/\sqrt{H}$, from 0.5 to 15. The larger the kR, the more angular momentum eigenstates that contribute to the vortex scattering cross section, and the more runtime-intensive the computation. For $kR = 15$, we set $N = 46$ and considered total angular momenta, $n + 1/2$, ranging from -22.5 to 22.5. Calculating solutions to the BdG equation both inside and outside of the vortex, the program matches solutions at $\rho = kR$ to obtain the coefficients, b_n, first for node 1 and then for nodes 2, 3, and 4. For each of the four nodes, Eqs. (4.88) and (4.94) are then used to calculate the differential cross section for quasiparticles in the vicinity of that node. The coefficients and differential cross sections for $kR = 8$ are shown in Fig. 4-3. Note that while the $d\sigma/d\varphi$ for each node can be quite skew, the four-node $d\sigma/d\varphi$ is approximately left-right symmetric. Although this left-right symmetry would be exact for the linearized Hamiltonian, the computation yields a net skewness, small by a factor of E/E_F, due to the perturbative contribution of the

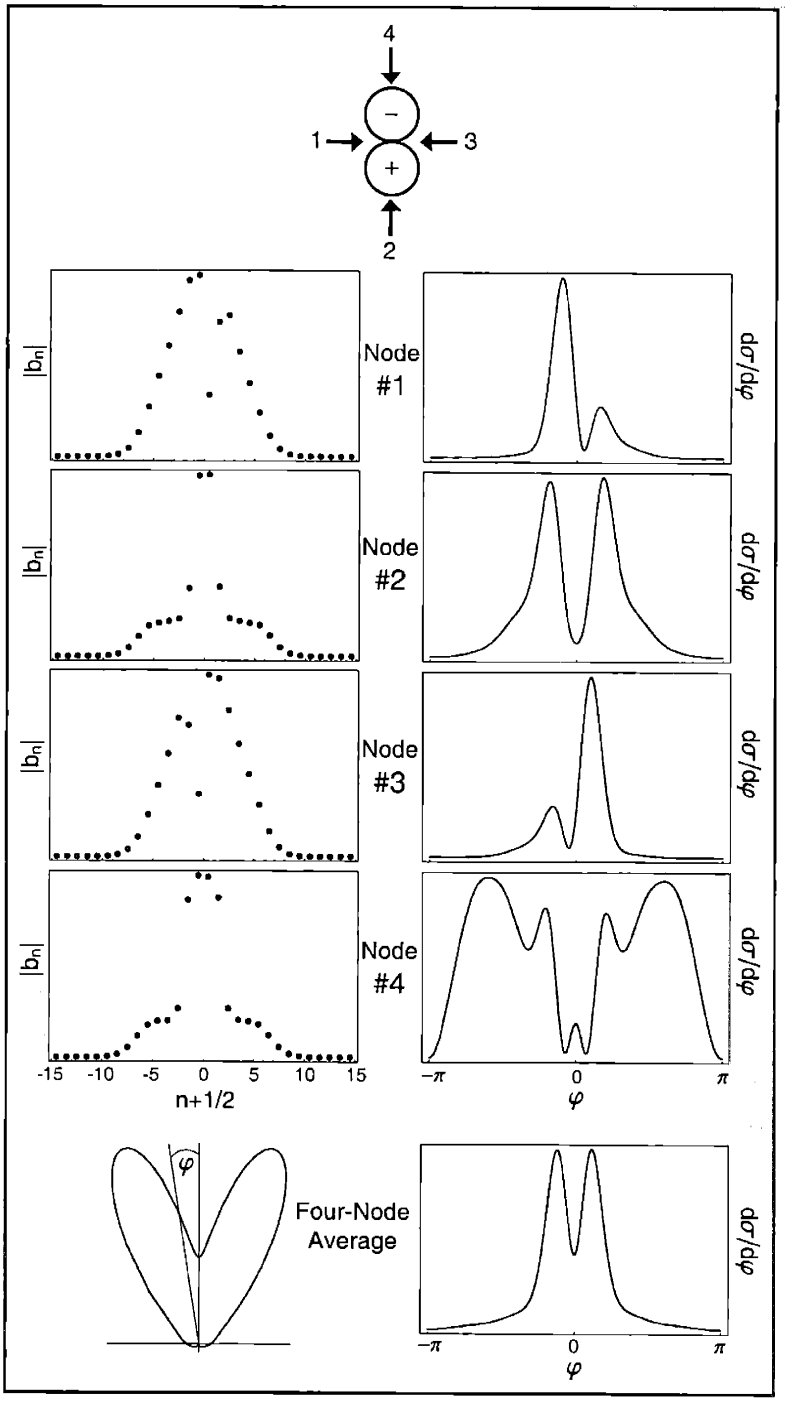

Figure 4-3: Matched coefficients and differential cross sections for $kR = 8$. The coefficients, b_n, denote the contributions from eigenstates with total angular momentum $n + 1/2$. These coefficients and the corresponding differential cross sections are plotted for quasiparticles about nodes 1, 2, 3, and 4. The final row contains the four-node average $d\sigma/d\varphi$ plotted in both Cartesian and polar form. The schematic above indicates the directions from which quasiparticles about each node approach the non-central effective potential.

curvature terms in the BdG equation. (Note that for our perturbative calculation of the skew scattering, we have selected a core size, $\xi = 10/p_F$, inside of which the superflow vanishes. While quantitative results depend on our choice of ξ, qualitative functional dependence is unaffected.) Polar plots of the four-node differential cross sections for integer kR from 1 to 15 are shown in Figs. 4-4 and 4-5. In all cases, $d\sigma/d\varphi$ has a two peak structure and vanishes for $\varphi = \pi$. For small kR, the peaks are centered about $\pm\pi/2$. As kR increases, the magnitude of $d\sigma/d\varphi$ increases while the peaks sweep closer to the forward direction. By integrating over angles, or utilizing Eqs. (4.95), (4.96), and (4.97), the total cross section, σ, the transport cross section, $\sigma_{\|}$, and the skew cross section, $\sigma_{\perp}$, are obtained as a function of kR. These results are plotted in Fig. 4-6. After a slow initial increase, the total cross section increases linearly with kR. The transport cross section initially follows the total cross section but then saturates toward a constant asymptotic value for $kR > 4$. This indicates that for large kR, while the magnitude of the cross section continues to increase, the peaks of the differential cross section sweep forward just enough that the transport cross section (weighted by a factor of $(1 - \cos\varphi)$) is unchanged. Like the total cross section, the skew cross section increases linearly with kR. Note that while σ and $\sigma_{\|}$ are plotted in units of $1/k$, $\sigma_{\perp}$ is plotted in units of $-1/p_F$. This reflects the fact that the skew cross section, induced by the curvature terms of the Hamiltonian, is small by a factor of k/p_F. The minus sign indicates that the quasiparticles get deflected to the right, just as an electron would in response to the Lorentz force. The oscillating component of the $\sigma_{\perp}$ data is believed to be a numerical artifact. (It is seen here because of the relative smallness of $\sigma_{\perp}$ and is likely due to the fact that we neglected curvature terms in the far field.) The lines through the σ and $\sigma_{\perp}$ data are fits to straight lines with small negative intercepts. The line through the $\sigma_{\|}$ data is an interpolation of the data points. In what follows, we shall assume that for larger kR, beyond the range of our numerical calculation, $\sigma_{\|}$ maintains its constant value and σ and $\sigma_{\perp}$ continue their linear dependence on kR.

The single vortex cross section discussed above was calculated to all orders in the linearized potential and to first order in the curvature terms. However, to gain some physical insight regarding the calculated form of our results, it is instructive to consider the more transparent Born-limit calculation (valid to first order in the potential) whereby $d\sigma/d\varphi$ is proportional to the square of the Fourier transform of the scattering potential. For the linearized Hamiltonian, our effective potential is $V^D = -v_f(1/r - r/R^2)\theta(R-r)\sin\phi$ where the θ-function imposes a cutoff at $r = R$. Given this input, the Born approximation yields an analytical expression for the differential cross section. We find

$$\left.\frac{d\sigma}{d\varphi}\right|_{\text{Born}} = \frac{\pi}{8k}\frac{\cos^2(\varphi/2)}{1-\cos\varphi}\left(1 - \frac{J_1(2kR\sin(\varphi/2))}{kR\sin(\varphi/2)}\right)^2 \tag{4.121}$$

where $J_1(x)$ is the first order Bessel function of the first kind. This form comes about because the two-dimensional Fourier transform of $1/r$ yields $1/q$ where $q^2 = |\mathbf{k}-\mathbf{k}'|^2 = 2k(1-\cos\varphi)$. Hence the square is proportional to $1/(1-\cos\varphi)$ and goes like $1/\varphi^2$ for small angles. The rest of the expression results from our cutoff at the vortex edge

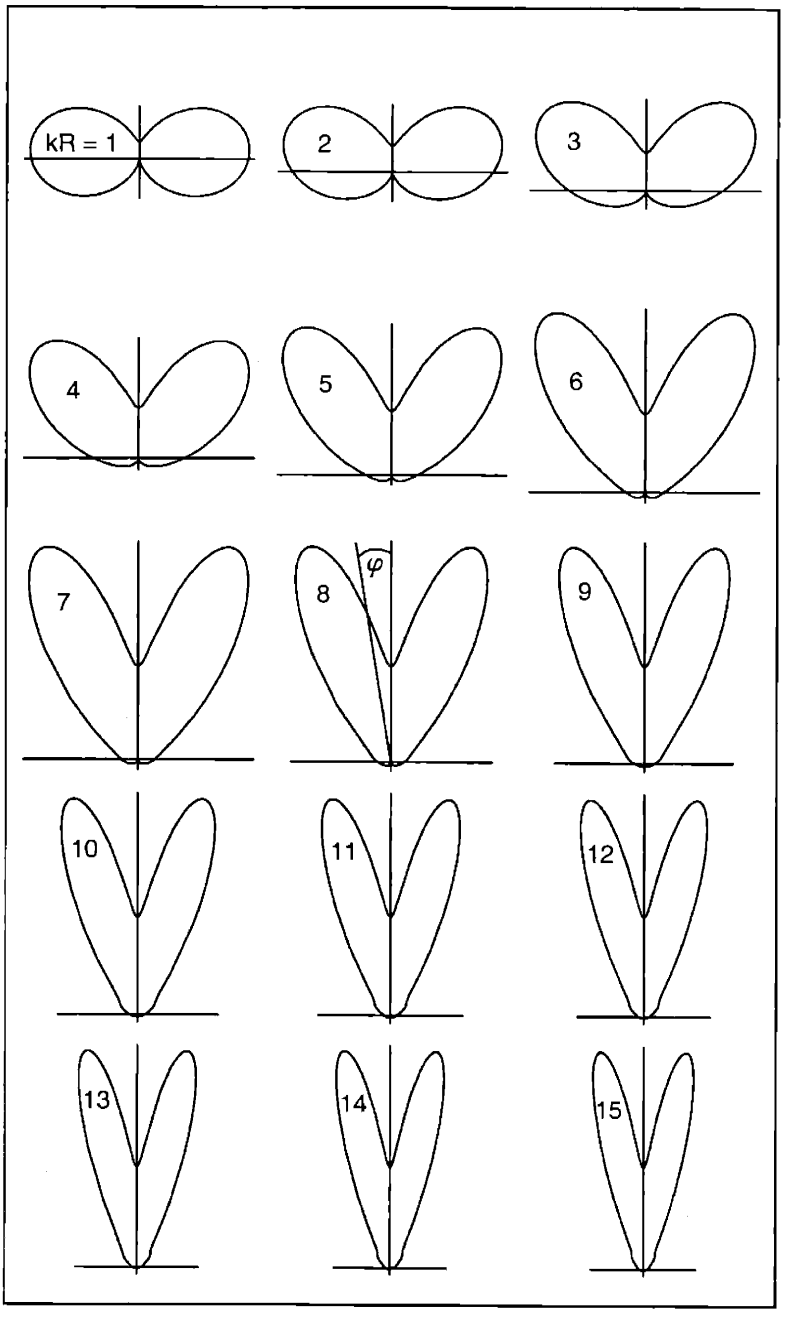

Figure 4-4: Polar plots of the four-node differential cross section for integer kR from 1 to 15. Scales are normalized to allow for easy comparison of angular profiles. Note that the peaks sweep toward the forward direction with increasing kR.

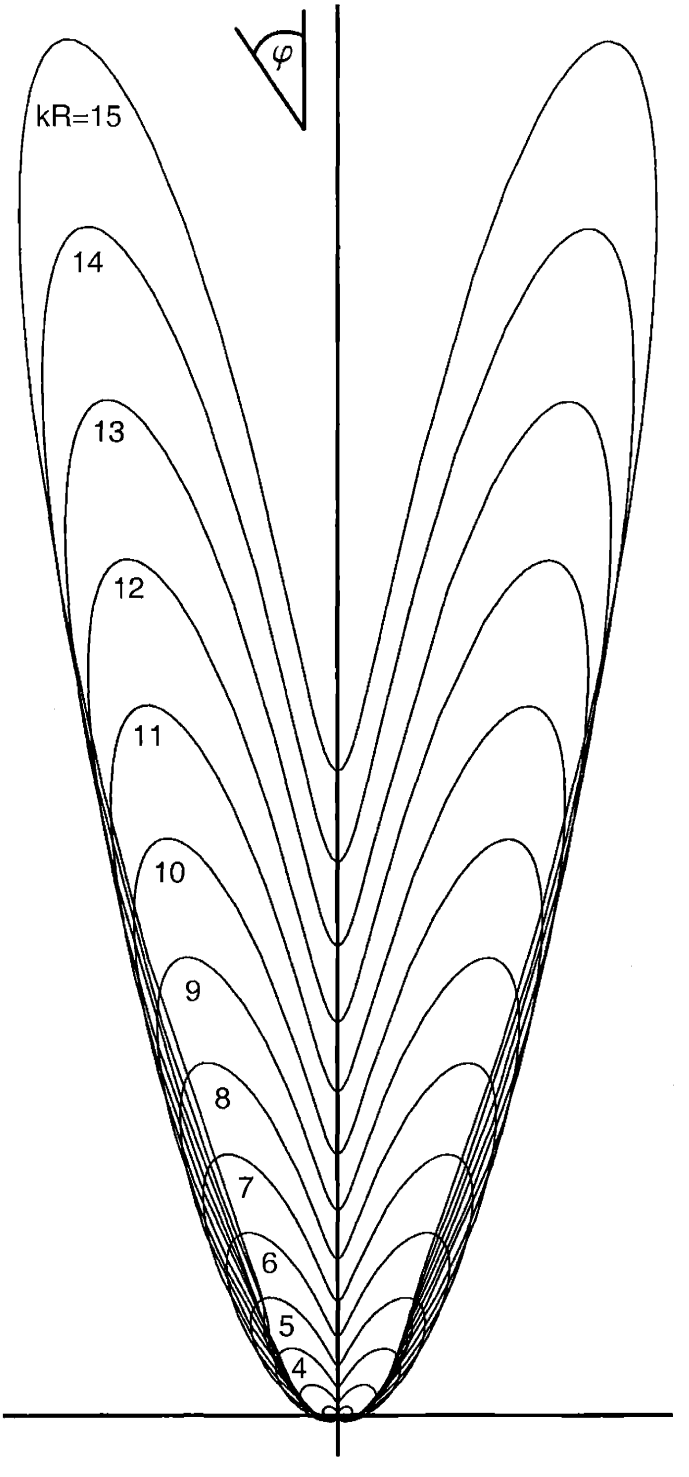

Figure 4-5: Fixed-scale polar plots of the four-node differential cross section for integer kR from 1 to 15. Note that the cross section magnitude grows with increasing kR.

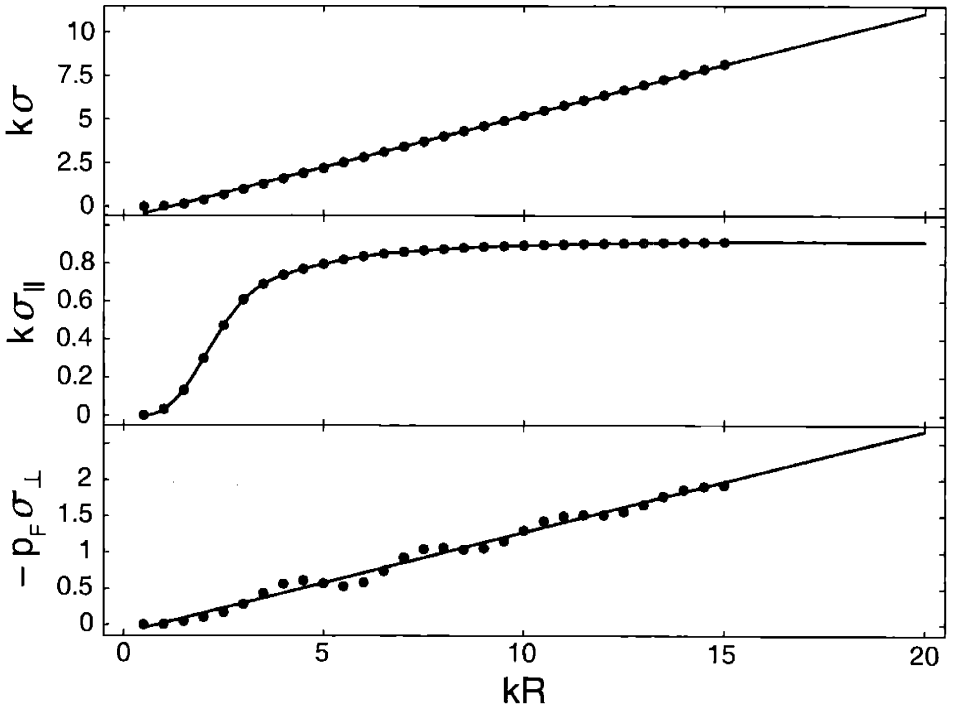

Figure 4-6: Calculated total cross section, transport cross section, and skew cross section as a function of kR from 0.5 to 15. For σ and $\sigma_\perp$, solid lines are fits to straight lines with small negative intercepts. For $\sigma_\parallel$, the solid line is an interpolation of the numerical data in which the constant large-kR behavior is extrapolated to larger kR. The oscillating component of the $\sigma_\perp$ data is believed to be a numerical artifact.

$(r = R)$ and serves to suppress $d\sigma/d\varphi$ for $\varphi < 1/kR$. Integrating over angles therefore yields a total cross section that is linear in kR for large kR. Recall that the transport cross section includes an additional weighting factor of $(1 - \cos\varphi)$. This precisely cancels the leading functional dependence of $d\sigma/d\varphi$ and results in a transport cross section that approaches a constant for large kR. Our numerical results for σ and $\sigma_{||}$ are therefore quite logical. To obtain the Born-limit skew cross section, we must also include the curvature terms. While this is easily done, the calculation unfortunately yields zero skewness to order k/p_F. Thus, while the Born approximation is sufficient to capture the qualitative features of our total and transport cross sections, it misses the skew cross section entirely. Hence, the simplest calculation that will recover a nonzero skew cross section must be valid to at least second order in the linearized potential and first order in the curvature terms.

We shall now use the fits to our numerical results as the input to our expressions for the longitudinal thermal conductivity, κ_{xx}, and the thermal Hall conductivity, κ_{xy}. As expressed in Eqs. (4.18) and (4.19)

$$\frac{\kappa_{xx}}{\alpha_0 T} \equiv F_{xx}(x) = \frac{1}{\frac{1}{A} + \frac{1}{\pi}x^2 f_{||}\left(\frac{1}{x}\right)} \qquad \frac{\kappa_{xy}}{\frac{\alpha_0 k_B}{2E_F}T^2} \equiv F_{xy}(x) = \frac{\frac{1}{\pi}x^2 f_{\perp}\left(\frac{1}{x}\right)}{\left(\frac{1}{A} + \frac{1}{\pi}x^2 f_{||}\left(\frac{1}{x}\right)\right)^2} \tag{4.122}$$

where $f_{||} \equiv k\sigma_{||}$, $f_{\perp} \equiv -p_F\sigma_{\perp}$, and $x = 1/kR = \sqrt{H}/\gamma T$. The other input, $A \equiv \kappa_e(T)/\alpha_0 T = k\ell_0$, is obtained empirically from (the electronic part of) the measured zero-field thermal conductivity in YBCO [74]. In the scaling regime, $T < 28$ K, the measured $\kappa_e(T)$ is linear in T, so A is a constant. The slope of the data yields $A \approx 112$. The resulting κ_{xx} and κ_{xy} scaling functions, $F_{xx}(x)$ and $F_{xy}(x)$, are plotted in Fig. 4-7. The F_{xx} curve begins at a constant value for $x = 0$, then falls off for larger x, and finally levels out. The F_{xy} curve is zero at $x = 0$, rises linearly for small x, then peaks and falls off for larger x, before finally leveling out. These results agree qualitatively with the mixed state thermal conductivity data measured in YBCO by Ong and co-workers [63, 62].

The functional form of our scaling curves can be understood as follows. In the small magnetic field regime, the quasiparticle mean free path is dominated by impurity scattering ($\ell_0 \ll \ell_v$). Since $x = 1/kR = \sqrt{H}/\gamma T$ is small, the cross sections take on their simple large-kR form,

$$f_{||}\left(\frac{1}{x}\right) \approx c_{||} \qquad f_{\perp}\left(\frac{1}{x}\right) \approx \frac{c_{\perp}}{x} \tag{4.123}$$

where $c_{||}$ and $c_{\perp}$ are constants. Therefore, the scaling functions are

$$F_{xx}(x) = A \qquad F_{xy}(x) = \frac{c_{\perp}A^2}{\pi}x \tag{4.124}$$

and we find that the weak-field thermal Hall conductivity is

$$\kappa_{xy}(H,T) = C_0 T\sqrt{H} \qquad C_0 \equiv \frac{\alpha_0 k_B c_{\perp} A^2}{2\pi\gamma E_F} \tag{4.125}$$

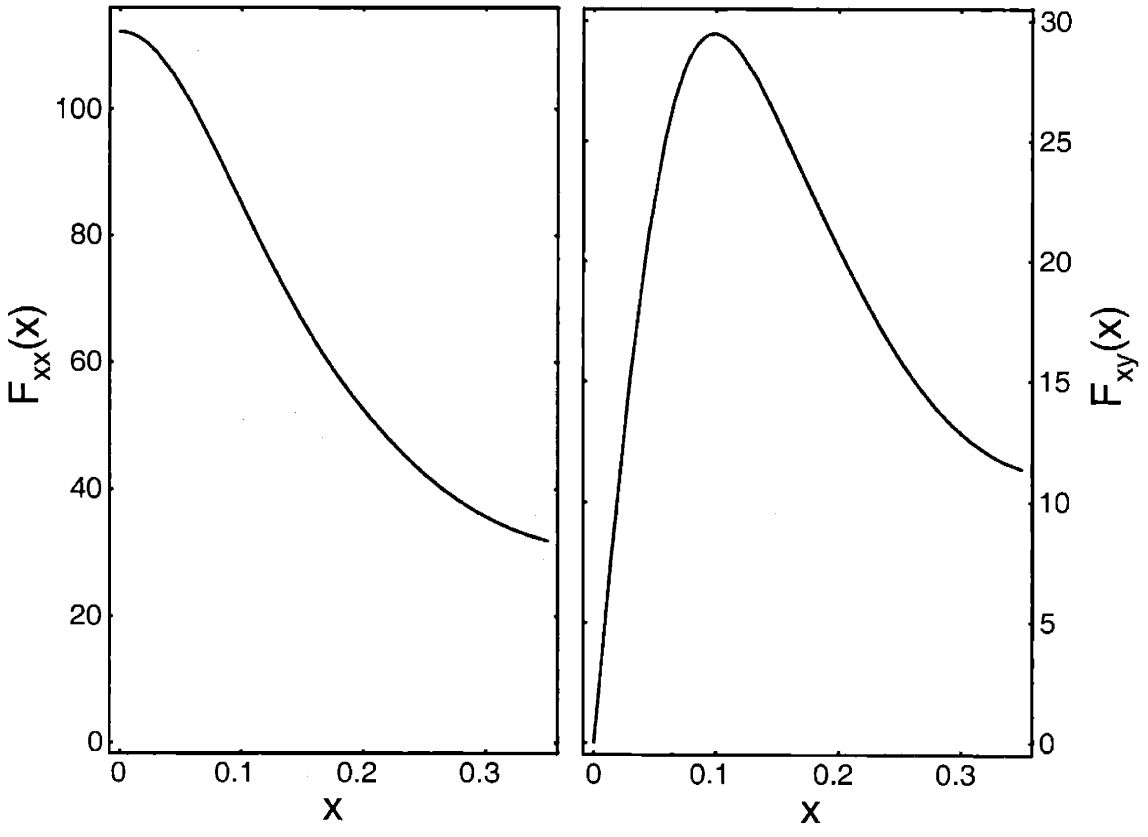

Figure 4-7: Calculated scaling functions for the longitudinal thermal conductivity, $F_{xx}(x) \sim \kappa_{xx}(H,T)/T$, and the thermal Hall conductivity, $F_{xy}(x) \sim \kappa_{xy}(H,T)/T^2$, plotted as a function of $x = \sqrt{H}/\gamma T$.

which is precisely the small-H form identified experimentally in YBCO [63]. As the magnetic field grows, vortex scattering increases, increasing the skew scattering while reducing the mean free path (and therefore κ_{xx}). Near the point where vortex scattering becomes comparable to impurity scattering ($\ell_0 \approx \ell_v$), the competition between the decreasing mean free path and the increasing skew scattering results in a peak for the κ_{xy} scaling curve. If the impurity scattering is sufficiently weak, this peak can occur for small enough H that the cross sections still take their simple large-kR forms. Thus, for sufficiently clean samples, at temperatures where scaling is satisfied, it follows from Eq. (4.122) that the peak height and location should be proportional to $A^{3/2}$ and $A^{-1/2}$ respectively. Recall, as well, that $C_0 \sim A^2$. These are predictions that can be checked experimentally by comparing results for samples of differing purity. Once vortex scattering dominates the mean free path ($\ell_0 \gg \ell_v$), κ_{xy} decreases with increasing magnetic field. Assuming we are still in the regime where Eq. (4.123) is valid, the scaling functions become

$$F_{xx}(x) = \frac{\pi}{c_{\|}} \frac{1}{x^2} \qquad F_{xy}(x) = \frac{\pi c_{\perp}}{c_{\|}^2} \frac{1}{x^3}. \tag{4.126}$$

As we push this model toward the strong-field (large x) regime, the transport cross section decreases from its large-kR value, increasing the mean free path and causing a leveling out and eventual upturn in the scaling curves for both κ_{xx} and κ_{xy}. However, in this strong-field regime ($\sqrt{H} > \gamma T$), there is a magnetic field contribution to the quasiparticle density of states and so our picture of thermally-excited quasiparticles scattering from dilute vortices ceases to be valid.

To this point we have considered only the (relatively low) temperatures where Simon-Lee scaling is observed. However, it is instructive to consider how and why it is violated at slightly higher temperatures. The reason the scaling works is that the massless Dirac equation has no intrinsic length scale aside from that provided by the temperature and magnetic field. Scaling will persist as long as the zero-field scattering does not introduce an additional length scale. At low temperatures, where impurity scattering dominates the zero-field mean free path, this is apparently satisfied since $\kappa_e(T) \sim T$, which implies $\ell_0 \sim 1/T$. However at higher temperatures, where inelastic scattering becomes important, $\kappa_e(T)$ deviates from linearity. As a result, $A = \kappa_e(T)/\alpha_0 T$ is no longer a constant and Simon-Lee scaling is violated. However, we are still able to calculate the thermal conductivity by simply using the temperature-dependent $A(T)$ as an input to our expressions. The $A(T)$ obtained from the zero-field $\kappa_e(T)$ measured in YBCO [74] is plotted in Fig. 4-8. Note that $A(T)$ is a constant for $T < 30$ K but decreases for larger temperatures where inelastic scattering becomes important. By plugging $A(T)$ into Eq. (4.122), we obtain a series of κ_{xx} and κ_{xy} curves, each corresponding to a different temperature. These are plotted (in scaling form) in Fig. 4-9. In each plot we show 15 curves for temperatures ranging from 15 K to 70 K. The low temperature curves (for which $A \approx$ const) satisfy Simon-Lee scaling and therefore lie nearly on top of each other. At higher temperatures, the curves gradually deviate from scaling, presumably due to the onset of inelastic scattering. This behavior agrees surprisingly well with experiment [63].

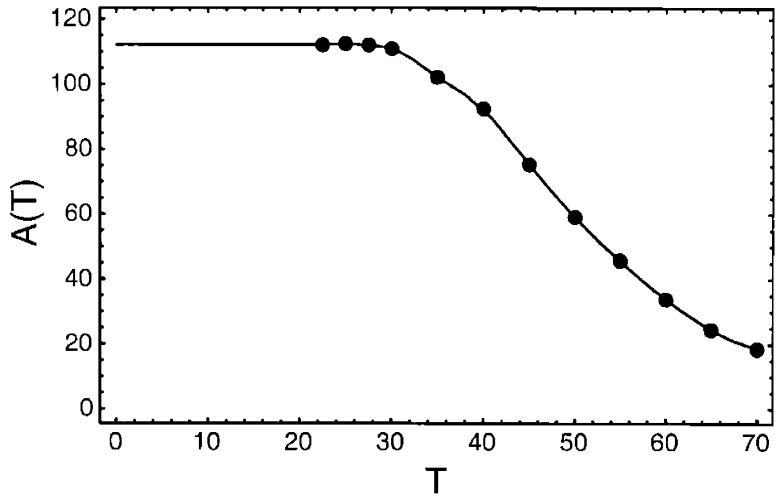

Figure 4-8: Temperature-dependence of $A(T) = \kappa_e(T)/\alpha_0 T$ as obtained from the electronic part of the zero-field longitudinal thermal conductivity measured in $YBa_2Cu_3O_{6.99}$ by Zhang and Ong [74]. The solid line is an interpolation of the measured data for $T \geq 22.5$ K and an extrapolation of the constant value ($A \approx 112$) for lower temperatures.

4.13 Conclusions

We set out to explain the temperature and magnetic field dependence of the thermal conductivity (κ_{xx} and κ_{xy}) measured in the mixed state of a d-wave superconductor. The key to this problem is the fact that the parameter regime of experimental interest is that in which the magnetic field is small compared to the temperature. Our picture is therefore one of thermally excited quasiparticles scattering from impurities and dilute vortices. In this simple regime, we were able to express κ_{xx} and κ_{xy} in terms of the transport cross section, $\sigma_{||}$, and skew cross section, $\sigma_{\perp}$, for quasiparticle scattering from a single vortex. Within certain approximations (see Sec. 4.6) we were able to obtain numerical solutions to the Bogoliubov-de Gennes equation for a single vortex and thereby construct the transport and skew cross sections for quasiparticle scattering. For $\sigma_{||}$ it was sufficient to consider the BdG Hamiltonian linearized about a gap node. However, since the linearized problem yields zero skewness, the calculation of $\sigma_{\perp}$ required a first order perturbation in the curvature terms of the Hamiltonian, which are small by a factor of $k_B T/E_F$. Fitting these numerical results and plugging into our expressions for the thermal conductivity, we calculated the Simon-Lee scaling functions for κ_{xx} and κ_{xy} (see Fig. 4-7). One input to the calculation is the electronic part of the zero-field thermal conductivity, $\kappa_e(T)$. We note that the scaling regime corresponds to that in which $\kappa_e(T) \sim T$. For higher temperatures at which inelastic scattering contributes to the zero-field mean free path, $\kappa_e(T)$ deviates from linearity and scaling is violated. Extending our calculation to this non-scaling regime, we demonstrated the manner in which the κ_{xx} and κ_{xy} curves deviate from scaling (see Fig. 4-9). Both the functional form of the scaling curves and the manner in which

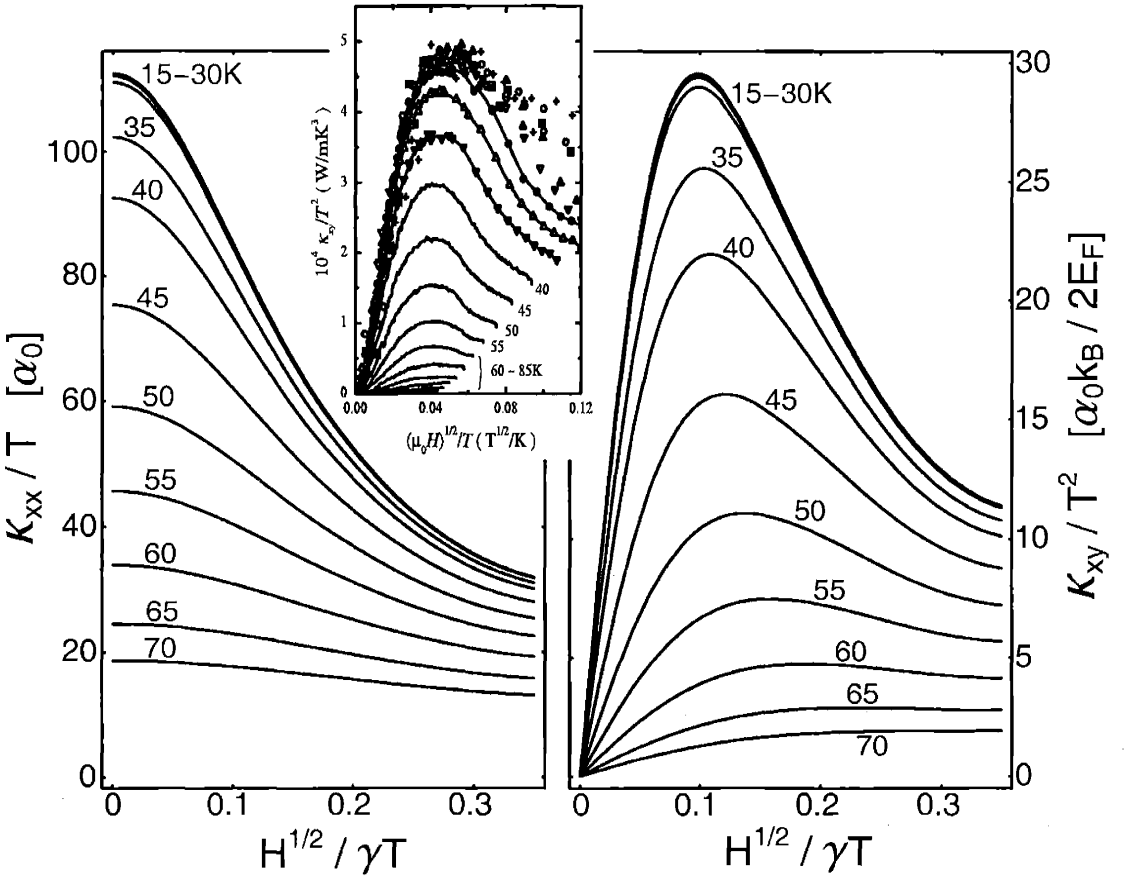

Figure 4-9: Calculated longitudinal thermal conductivity (left) and thermal Hall conductivity (right) plotted in scaling form (in units defined in the text). The inset is the measured thermal Hall conductivity (in SI units) obtained by Ong and co-workers for $YBa_2Cu_3O_{6.99}$ and reproduced here from Ref. [63].

scaling is violated agree qualitatively with the mixed state thermal conductivity data measured in YBCO by Ong and co-workers [63].

In particular, we have reproduced the simple, yet previously unexpected, form of the measured weak-field thermal Hall conductivity, $\kappa_{xy} \sim T\sqrt{H}$. This result is easily understood in terms of our analysis. Summarizing the discussion of Sec. 4.2, we write $\kappa_{xx} \sim C_v \ell$ and $\kappa_{xy} \sim \kappa_{xx} n_v \sigma_\perp \ell \sim C_v \ell^2 n_v \sigma_\perp$, where C_v is the specific heat and n_v is the vortex density. In the weak-field limit, since quasiparticles are thermally excited, $C_v \sim T^2$. Furthermore, for small magnetic fields, the quasiparticle mean free path is dominated by impurity scattering. Therefore $\ell \sim \ell_0 \sim \kappa_e(T)/C_v \sim 1/T$. The vortex density is just proportional to the magnetic field, $n_v \sim H$. Thus we need only find the H and T dependence of the single vortex skew scattering cross section. Our numerics yield $\sigma_\perp \sim (k/p_F)R \sim T/\sqrt{H}$, which says that, aside from being small by a factor of k/p_F, the skew cross section is just proportional to the effective vortex radius, R. Putting it all together yields $\kappa_{xy} \sim (T^2)(1/T)^2(H)(T/\sqrt{H}) \sim T\sqrt{H}$. The simple form of this result is due to the simple nature of the weak-field regime. Here we have thermally excited quasiparticles with a mean free path due to impurity scattering. The only effect of the vortices is to add a small skew component to the scattering. The unusual $\sqrt{H}$ Hall response results because, while the number of vortices goes like H, the skew cross section per vortex goes like $1/\sqrt{H}$.

While our analysis appears to yield the correct functional form of the thermal conductivity, we do not expect our results to be quantitative due to the approximations we made in calculating the single vortex cross section. To obtain more quantitative results, one must include the Berry phase contribution, consider anisotropic Dirac nodes, and account (via empirical input) for the details of the vortex core. This is left for future work.

4.14 Appendix: Berry Phase Scattering of Incident Plane Wave

Quasiparticles scatter from vortices via both the circulating superflow and the Berry phase factor of (-1) acquired upon circling the vortex. This phase is encoded in the antiperiodic boundary conditions imposed on quasiparticles in our chosen gauge. In the body of this work, we neglect the Berry phase contribution and consider only the scattering from the superflow. In this appendix, we neglect the superflow and consider only the Berry phase contribution. That is, we consider the scattering of quasiparticles due only to the presence of antiperiodic boundary conditions. As we shall see, the antiperiodic boundary conditions yield the Aharonov-Bohm interference effect of an enclosed π-flux.

As in Sec. 4.9, we consider the isotropic Dirac Hamiltonian

$$H = v_f \left[\tau_3 p_x + \tau_1 p_y\right] \tag{4.127}$$

and seek solutions to the Bogoliubov-de Gennes equation, $H\Phi = E\Phi$. We express the quasiparticle wave function as a linear combination of angular momentum eigenstates

which satisfy $J\Phi_\mu = \mu\Phi_\mu$. Since we have neglected the superflow, there is no effective potential and the general solution is easily found to be

$$\Phi = \sum_\mu \left[(A_\mu J_{\mu-\frac{1}{2}} + B_\mu Y_{\mu-\frac{1}{2}}) e^{i(\mu-\frac{1}{2})\phi} \begin{pmatrix} 1 \\ i \end{pmatrix} + i(A_\mu J_{\mu+\frac{1}{2}} + B_\mu Y_{\mu+\frac{1}{2}}) e^{i(\mu+\frac{1}{2})\phi} \begin{pmatrix} 1 \\ -i \end{pmatrix} \right] \tag{4.128}$$

where A_μ and B_μ are complex constants and $J_{\mu\pm\frac{1}{2}}$ and $Y_{\mu\pm\frac{1}{2}}$ are Bessel functions of argument $\rho = kr$. However, rather than imposing periodic boundary conditions by requiring that $\mu = n + 1/2$ with $n =$ integer, here we shall impose antiperiodic boundary conditions,

$$\Phi(r, \phi + 2\pi) = -\Phi(r, \phi) \tag{4.129}$$

by requiring that $\mu =$ integer. The radial functions are therefore half-integer Bessel functions rather than integer Bessel functions. The coefficients, A_μ and B_μ, are determined by satisfying boundary conditions at both long and short distances.

At long distances, we require an asymptotic wave function that is equal to the sum of an incident plane wave, Φ_i, and an outgoing radial wave, Φ_s. In terms of the current functional, $\mathbf{j}[\Phi] = v_f \Phi^\dagger(\tau_3 \hat{\mathbf{x}} + \tau_1 \hat{\mathbf{y}})\Phi$, we require that $\mathbf{j}[\Phi_i] \sim \hat{\mathbf{k}}$ and $\mathbf{j}[\Phi_s] \sim \hat{\mathbf{r}}$. In the presence of antiperiodic boundary conditions, we seek an incident wave of the form

$$\Phi_i(\mathbf{r}) = e^{i\gamma\frac{\varphi}{2}} e^{i\mathbf{k}\cdot\mathbf{r}} \begin{pmatrix} \cos\frac{\theta}{2} \\ \sin\frac{\theta}{2} \end{pmatrix} \qquad \gamma = \pm 1 \tag{4.130}$$

and a scattered wave of the form

$$\Phi_s(\mathbf{r}) = f(\varphi)\frac{e^{ikr}}{\sqrt{r}} \begin{pmatrix} \cos\frac{\phi}{2} \\ \sin\frac{\phi}{2} \end{pmatrix} \tag{4.131}$$

where $\mathbf{k} = (k, \theta)$, $\mathbf{r} = (r, \phi)$, and $\varphi = \phi - \theta$. In analogy with the problem of Aharonov-Bohm [86] scattering from an enclosed magnetic flux, we can say that $\gamma = -1$ corresponds to an effective π-flux while $\gamma = +1$ corresponds to an effective $(-\pi)$-flux. Since these two cases are equivalent, the choice of $\gamma = \pm 1$ is arbitrary. In the asymptotic limit, the half-integer Bessel functions take the form

$$J_{\mu-\frac{1}{2}}(\rho) = \eta_\mu \sqrt{\frac{2}{\pi\rho}} \cos(\rho - |\mu|\pi/2) \qquad Y_{\mu-\frac{1}{2}}(\rho) = \eta_\mu \sqrt{\frac{2}{\pi\rho}} \sin(\rho - |\mu|\pi/2) \tag{4.132}$$

where $\eta_\mu = 1$ for $\mu > 0$ and $\eta_\mu = (-1)^\mu$ for $\mu \leq 0$. Proceeding along the lines of Sec. 4.9.3, we can plug these asymptotic expressions into Eq. (4.128), reorganize terms, and thereby obtain a suggestive (yet still general) form for the quasiparticle wave function. Doing so, we find that

$$\Phi = e^{i\gamma\frac{\varphi}{2}} e^{i\mathbf{k}\cdot\mathbf{r}} \begin{pmatrix} \cos\frac{\theta}{2} \\ \sin\frac{\theta}{2} \end{pmatrix} + f(\varphi)\frac{e^{ikr}}{\sqrt{r}} \begin{pmatrix} \cos\frac{\phi}{2} \\ \sin\frac{\phi}{2} \end{pmatrix} - i\gamma g(\varphi)\frac{e^{-ikr}}{\sqrt{r}} \begin{pmatrix} -\sin\frac{\phi}{2} \\ \cos\frac{\phi}{2} \end{pmatrix} \tag{4.133}$$

where

$$f(\varphi) \equiv \sqrt{\frac{2}{\pi k}} \sum_{\mu} b_\mu e^{i\mu\varphi} \qquad g(\varphi) \equiv \sqrt{\frac{2}{\pi k}} \sum_{\mu} a_\mu e^{i\mu\varphi} \tag{4.134}$$

and a_μ and b_μ are complex constants defined via

$$A_\mu - iB_\mu \equiv i^\mu e^{-i\mu\theta} \left(e^{-i\frac{\pi}{4}}/2 + b_\mu \right) \tag{4.135}$$

$$A_\mu + iB_\mu \equiv -\gamma i^\mu e^{-i\mu\theta} \left(e^{i\frac{\pi}{4}}/2 + (-1)^\mu a_\mu \right). \tag{4.136}$$

If the plane wave is to be the only incident wave, we must eliminate the incident radial wave by requiring that $a_\mu = 0$ for all μ. With this restriction, B_μ and b_μ are related to A_μ via

$$B_\mu = i \left(A_\mu + i\gamma \; A_\mu^0 \right) \qquad b_\mu = e^{-i\frac{\pi}{4}} \left(\frac{A_\mu}{A_\mu^0} - \frac{1 - i\gamma}{2} \right) \tag{4.137}$$

where $A_\mu^0 \equiv i^{\mu - 1/2} e^{-i\mu\theta}/2$. The asymptotic wave function then takes the desired form

$$\Phi = e^{i\gamma\frac{\varphi}{2}} e^{i\mathbf{k}\cdot\mathbf{r}} \begin{pmatrix} \cos\frac{\theta}{2} \\ \sin\frac{\theta}{2} \end{pmatrix} + f(\varphi) \frac{e^{ikr}}{\sqrt{r}} \begin{pmatrix} \cos\frac{\phi}{2} \\ \sin\frac{\phi}{2} \end{pmatrix} \tag{4.138}$$

and the differential cross section is given by

$$\frac{d\sigma}{d\varphi} = |f(\varphi)|^2 = \frac{2}{\pi k} \left| \sum_{\mu} b_\mu e^{i\mu\varphi} \right|^2. \tag{4.139}$$

We can now determine the b_μ by imposing appropriate boundary conditions at the origin. As discussed in Sec. 4.10.2, the most restrictive condition is that the current through the origin (a point of zero area) must be zero. More precisely, we consider a semicircle of radius ϵ, oriented about the $\hat{\theta}$ direction, and require that the total current passing through it, I_θ, vanishes as $\epsilon \to 0$. If $\Phi(\rho \to 0) \sim \rho^\alpha$, then $I_\theta \sim \epsilon^{2\alpha+1}$. Thus, to ensure that I_θ does not diverge at the origin, we must eliminate all terms in Eq. (4.128) which diverge faster than $\rho^{-1/2}$ as $\rho \to 0$. Since the half-integer Bessel functions exhibit the small-argument behavior, $J_{\mu\pm\frac{1}{2}} \sim \rho^{\mu\pm\frac{1}{2}}$ and $Y_{\mu\pm\frac{1}{2}} \sim \rho^{-\mu\mp\frac{1}{2}}$, this clearly requires that

$$B_\mu = 0 \text{ for } \mu > 0 \qquad A_\mu = 0 \text{ for } \mu < 0 \tag{4.140}$$

The condition for $\mu = 0$ is more subtle. Enforcing the above, the resulting wave function is dominated, as $\rho \to 0$, by the terms which diverge exactly as $\rho^{-1/2}$. We therefore find that

$$\Phi(\rho \to 0) = \sqrt{\frac{2}{\pi\rho}} \left[(A_0 - iB_0) \begin{pmatrix} \cos\frac{\theta}{2} \\ \sin\frac{\theta}{2} \end{pmatrix} + i(A_0 + iB_0) \begin{pmatrix} -\sin\frac{\theta}{2} \\ \cos\frac{\theta}{2} \end{pmatrix} \right]. \tag{4.141}$$

From Eq. (4.137), we know that $A_0 + iB_0 = -i\gamma A_0^0$ where $A_0^0 = e^{-i\pi/4}/2$. Furthermore,

we can define a complex constant, β, such that $A_0 - iB_0 \equiv -i\gamma A_0^0 \beta$. With this definition, the current density near the origin takes the form

$$\mathbf{j}(\rho \to 0) = \frac{v_f}{2\pi\rho}\left[\left(|\beta|^2 - 1\right)\hat{r} + 2\,\mathrm{Im}[\beta]\hat{\phi}\right]. \tag{4.142}$$

Explicitly computing the current through the origin, we find that

$$I_\theta = \lim_{\epsilon\to 0}\int_{\theta-\pi/2}^{\theta+\pi/2} \epsilon\, d\phi\, \mathbf{j}(\epsilon)\cdot\hat{\theta} = v_f \int \frac{d\phi}{2\pi}\left[\left(|\beta|^2 - 1\right)\hat{r}\cdot\hat{\theta} + 2\,\mathrm{Im}[\beta]\hat{\phi}\cdot\hat{\theta}\right] \tag{4.143}$$

which must be set to zero for all directions $\hat{\theta}$. This requires that $\beta = \pm 1$.

Putting everything together yields the values of our original coefficients

$$A_\mu = -i\gamma A_\mu^0 \left\{ \begin{array}{cc} 1 & \mu > 0 \\ \frac{1+\beta}{2} & \mu = 0 \\ 0 & \mu < 0 \end{array} \right\} \qquad B_\mu = -\gamma A_\mu^0 \left\{ \begin{array}{cc} 0 & \mu > 0 \\ \frac{1-\beta}{2} & \mu = 0 \\ 1 & \mu < 0 \end{array} \right\} \tag{4.144}$$

where $\gamma = \pm 1$ and $\beta = \pm 1$. The Z_2 ambiguity in γ and β is a consequence of the equivalence of a π-flux with a $(-\pi)$-flux, which cannot affect observable quantities. For $\beta = \gamma = \pm 1$,

$$b_\mu = \frac{1}{\sqrt{2}} \left\{ \begin{array}{cc} i & \gamma\mu > 0 \\ -1 & \gamma\mu \leq 0 \end{array} \right\}. \tag{4.145}$$

Plugging this into Eq. (4.139) and summing over μ (with a convergence factor $e^{-|\mu|0^+}$), yields

$$\frac{d\sigma}{d\varphi} = \frac{1}{2\pi k\,\sin^2(\varphi/2)} - \gamma\frac{2}{k}\frac{\delta(\varphi)}{\varphi}. \tag{4.146}$$

The same result is obtained for $\beta = -\gamma$. Note, however, that the above is only valid for $\varphi \neq 0$. As discussed (for the electron scattering case) in the original paper by Aharonov and Bohm [86], as well as in an excellent review by Olariu and Popescu [87], our asymptotic approximations are only valid away from the forward direction. Thus, the second term above, which is only nonzero for $\varphi = 0$ and is an artifact of our casual treatment of the forward direction, can be dropped. (For a detailed treatment of the Aharonov-Bohm scattering of an electron in the forward direction, see the paper by Stelitano [88].) Our differential cross section therefore takes the form

$$\frac{d\sigma}{d\varphi} = \frac{1}{2\pi k\,\sin^2(\varphi/2)} \tag{4.147}$$

which is exactly the differential cross section for the Aharonov-Bohm scattering of an electron from an enclosed π-flux. As expected, this result is independent of our choice of $\gamma = \pm 1$ and $\beta = \pm 1$ and is the same for quasiparticles about any of the four gap nodes. Due to the infinite range of the Berry phase effect, the total cross section diverges. However, the transport cross section is finite and given by $\sigma_{||} = 1/\pi k$. Since left-right symmetry is not broken in the absence of a superflow, the skew cross section is zero. Therefore, the Berry phase interference effect does not, on its own, yield a

thermal Hall conductivity. It could, however, serve to modify the skew scattering induced by the presence of a superflow.

In the zero-superflow case considered above, it was easy enough to neglect the subtleties associated with forward scattering in the presence of antiperiodic boundary conditions. However, if we were to consider the superflow and the Berry phase effects together, it would be necessary to treat such nuances more carefully. This is left for future work.

Bibliography

[1] H. Kamerlingh Onnes, Comm. Phys. Lab. Univ. Leiden, Nos. 119, 120, 122 (1911)

[2] W. Meissner and R. Ochsenfeld, Naturwiss. bf 21, 787 (1933)

[3] C. J. Gorter and H. G. B. Casimir, Phys. Z. **35**, 963 (1934); Z. Tech. Phys. **15**, 539 (1934)

[4] F. London and H. London, Proc. Roy. Soc. (London) **A149**, 71 (1935); Physica **2** 341 (1935)

[5] V. L. Ginsburg and L. D. Landau, J. Exptl. Theoret. Phys. (USSR) **20**, 1064 (1950)

[6] J. Bardeen, L. N. Cooper, and J. R. Schrieffer, Phys. Rev. **106**, 162 (1957); **108**, 1175 (1957)

[7] J. R. Schrieffer, *Theory of Superconductivity* (Addison-Wesley Publishing Company, Reading, MA, 1964)

[8] P. A. Lee, Science **277**, 50 (1997)

[9] J. G. Bednorz and K. A. Muller, Z. Phys. B **64**, 189 (1986)

[10] J. Orenstein and A. J. Millis, Science **288**, 468 (2000)

[11] J. R. Kirtley *et al.*, Nature **373**, 225 (1995); D. J. Van Harlingen, Rev. Mod. Phys. **67** 515 (1995)

[12] P. A. Lee and X. G. Wen, Phys. Rev. Lett. **78**, 4111 (1997)

[13] G. D. Mahan, *Many-Particle Physics* (Plenum Press, New York, 1990)

[14] J. M. Ziman, *Principles of the Theory of Solids* (Cambridge University Press, Cambridge, 1964)

[15] N. W. Ashcroft and N. D. Mermin, *Solid State Physics* (Saunders College Publishing, Fort Worth, 1976)

[16] P. A. Lee, Phys. Rev. Lett. **71**, 1887 (1993)

[17] P. J. Hirschfeld, W. O. Putikka, and D. J. Scalapino, Phys. Rev. Lett. **71**, 3705 (1993)

[18] P. J. Hirschfeld, W. O. Putikka, and D. J. Scalapino, Phys. Rev. B **50**, 10250 (1994)

[19] P. J. Hirschfeld and W. O. Putikka, Phys. Rev. Lett. **77**, 3909 (1996)

[20] M. J. Graf, S-K. Yip, J. A. Sauls, and D. Rainer, Phys. Rev. B **53**, 15147 (1996)

[21] T. Senthil, M. P. A. Fisher, L. Balents, and C. Nayak, Phys. Rev. Lett. **81**, 4704 (1998)

[22] A. V. Balatsky, A. Rosengren, and B. L. Altshuler, Phys. Rev. Lett. **73**, 720 (1994)

[23] A. J. Millis, S. M. Girvin, L. B. Ioffe, and A. I. Larkin, J. Phys. Chem. Solids **59**, 1742 (1998)

[24] D. Xu, S. K. Yip, and J. A. Sauls, Phys. Rev. B **51**, 16233 (1995)

[25] A. Hosseini, R. Harris, S. Kamal, P. Dosanjh, J. Preston, R. Liang, W. N. Hardy, and D. A. Bonn, Phys. Rev. B **60**, 1349 (1999)

[26] L. Taillefer, B. Lussier, R. Gagnon, K. Behnia, and H. Aubin, Phys. Rev. Lett. **79**, 483 (1997)

[27] M. Chiao, R. W. Hill, C. Lupien, B Popic, R. Gagnon, and L. Taillefer, Phys. Rev. Lett. **82**, 2943 (1999)

[28] D. A. Bonn, S. Kamal, A. Bonakdarpour, R. Liang, W. N. Hardy, C. C. Holmes, D. N. Basov, and T. Timusk, Czech. J. Phys. **46**, 3195 (1996)

[29] J. Mesot, M. R. Norman, H. Ding, M. Randeria, J. C. Campuzano, A. Paramekanti, H. M. Fretwell, A. Kaminski, T. Takeuchi, T. Yokoya, T. Sato, T. Takahashi, T. Mochiku, and K. Kadowaki, Phys. Rev. Lett. **83**, 840 (1999)

[30] L. P. Gorkov and P. A. Kalugin, Pis'ma Zh. Eksp. Teor. Fiz. **41**, 208 (1985) [JETP Lett. **41**, 253 (1985)]

[31] A. A. Nersesyan, A. M. Tsvelik, and F. Wenger, Nucl. Phys. **B438**, 561 (1995)

[32] T. Senthil and M. P. A. Fisher, Phys. Rev. B **60**, 6893 (1999)

[33] V. Ambegaokar and A. Griffin, Phys. Rev. **137**, A1151 (1965)

[34] V. Ambegaokar and L. Tewordt, Phys. Rev. **134**, A805 (1964)

[35] H. Monien, K. Scharnberg, and D. Walker, Solid State Commun. **63**, 263 (1987)

[36] P. J. Hirschfeld, P. Wölfle, and D. Einzel, Phys. Rev. B **37**, 83 (1988)

[37] A. I. Larkin and A. B. Migdal, Zh. Eksp. Teor. Fiz. **44**, 1703 (1963) [JETP **17**, 1146 (1963)]

[38] A. I. Larkin, Zh. Eksp. Teor. Fiz. **46**, 2188 (1964) [JETP **19**, 1478 (1964)]

[39] A. J. Leggett, Phys. Rev. **140**, A1869 (1965)

[40] D. Pines and P. Nozieres, *The Theory of Quantum Liquids* (Addison-Wesley Publishing Company, Reading, MA, 1966)

[41] J. Moreno and P. Coleman, cond-mat/9603079 (unpublished)

[42] M. Chiao, R. W. Hill, C. Lupien, L. Taillefer, P. Lambert, R. Gagnon, and P. Fournier, Phys. Rev. B **62**, 3554 (2000)

[43] S. F. Lee, D. C. Morgan, R. J. Ormeno, D. M. Broun, R. A. Doyle, and J. R. Waldram, Phys. Rev. Lett. **77**, 735 (1996)

[44] D. A. Bonn, R. Liang, T. M. Riseman, D. J. Baar, D. C. Morgan, K. Zhang, P. Dosanjh, T. L. Duty, A. MacFarlane, G. D. Morris, J. H. Brewer, W. N. Hardy, C. Kallin, and A. J. Berlinsky, Phys. Rev. B **47**, 11314 (1993)

[45] D. A. Bonn, P. Dosanjh, R. Liang, and W. N. Hardy, Phys. Rev. Lett. **68**, 2390 (1992)

[46] P. J. Hirschfeld, P. Wölfe, J. A. Sauls, D. Einzel, and W. O. Putikka, Phys. Rev. B **40**, 6695 (1989)

[47] P. J. Hirschfeld, D. Vollhardt, and P. Wölfe, Solid State Comm. **59**, 111 (1986)

[48] M. J. Graf, M. Palumbo, D. Rainer, and J. A. Sauls, Phys. Rev. B **52**, 10588 (1995)

[49] Y. Sun and K. Maki, Europhys. Lett. **32**, 355 (1995)

[50] M. B. Walker and M. F. Smith, Phys. Rev. B **61**, 11285 (2000)

[51] A. J. Berlinksy, D. A. Bonn, R. Harris, and C. Kallin, Phys. Rev. B **61**, 9088 (2000)

[52] Note that Hettler and Hirschfeld have recently proposed a more complex theory of impurity scattering, involving order parameter suppression at impurity sites, to fit the experimental data using a point defect model. [M. H. Hettler and P. J. Hirschfeld, Phys. Rev. B **61**, 11313 (2000); Phys. Rev. B **59**, 9606 (1999)]

[53] Note that Zhitomirsky and Walker have studied scattering in a twinned d-wave superconductor (prior to detwinning) and calculated the electronic states and thermal conductivity associated with the twin boundaries. [M. E. Zhitomirsky and M. B. Walker, Phys. Rev. Lett. **79**, 1734 (1997); Phys. Rev. B **57**, 8560 (1998)]

[54] R. Harris, (private communication)

[55] H. Shaked, P. M. Keane, J. C. Rodriguez, F. F. Owen, R. L. Hitterman, and J. D. Jorgensen, *Crystal Structures of the High-T_c Superconducting Copper-Oxides* (Elsevier Science B. V., Amsterdam, The Netherlands 1994)

[56] J. L. Tallon, Phys. Rev. B **39**, 2784 (1989)

[57] A. C. Durst and P. A. Lee, Phys. Rev. B **62**, 1270 (2000)

[58] L. Taillefer, Bull. Am. Phys. Soc. **46**, 363 (2001)

[59] K. Zhang, D. A. Bonn, S. Kamal, R. Liang, D. J. Baar, W. N. Hardy, D. Basov, and T. Timusk, Phys. Rev. Lett. **73**, 2484 (1994)

[60] K. Krishana, J. M. Harris, and N. P. Ong, Phys. Rev. Lett. **75**, 3529 (1995)

[61] K. Krishana, N. P. Ong, Y. Zhang, Z. A. Xu, R. Gagnon, and L. Taillefer, Phys. Rev. Lett. **82**, 5108 (1999)

[62] N. P. Ong, K. Krishana, Y. Zhang, and Z. A. Xu, cond-mat/9904160 (unpublished)

[63] Y. Zhang, N. P. Ong, P. W. Anderson, D. A. Bonn, R. Liang, and W. N. Hardy, Phys. Rev. Lett. **86**, 890 (2001)

[64] R. Ocana, A. Taldenkov, P. Esquinazi, and Y. Kopelevich, J. Low Temp. Phys. **123**, 181 (2001)

[65] S. H. Simon and P. A. Lee, Phys. Rev. Lett. **78**, 1548 (1997)

[66] G. E. Volovik, JETP Lett. **58**, 469 (1993)

[67] N. B. Kopnin and G. E. Volovik, JETP Lett. **64**, 690 (1996)

[68] G. E. Volovik, JETP Lett. **65**, 491 (1997)

[69] M. Franz, Phys. Rev. Lett. **82**, 1760 (1999)

[70] I. Vekhter and A. Houghton, Phys. Rev. Lett. **83**, 4626 (1999)

[71] J. Ye, Phys. Rev. Lett. **86**, 316 (2001)

[72] A. Vishwanath, Phys. Rev. Lett. **87**, 217004 (2001); cond-mat/0104213 (unpublished)

[73] O. Vafek, A. Melikyan, and Z. Tesanovic, Phys. Rev. B **64**, 224508 (2001)

[74] Y. Zhang and N. P. Ong (private communication)

[75] R. Cleary, Phys. Rev. **175**, 587 (1968)

[76] R. Cleary, Phys. Rev. B **1**, 169 (1970)

[77] C. Caroli, P. G. de Gennes, and J. Matricon, Phys. Lett. **9**, 307 (1964)

[78] P. G. de Gennes, *Superconductivity of Metals and Alloys* (Perseus Books, Reading, MA, 1966)

[79] O. Vafek, A. Melikyan, M. Franz, and Z. Tesanovic, Phys. Rev. B **63**, 134509 (2001)

[80] T. Senthil and M. P. A. Fisher, Phys. Rev. B **62**, 7850 (2000)

[81] M. Franz and Z. Tesanovic, Phys. Rev. Lett. **84**, 554 (2000)

[82] M. H. Mittleman and R. E. von Holdt, Phys. Rev. **140**, A726 (1965)

[83] S. Altshuler, Phys. Rev. **107**, 114 (1957)

[84] See for example, C. M. Bender and S. A. Orszag, *Advanced Mathematical Methods for Scientists and Engineers* (McGraw-Hill Book Company, New York, 1978)

[85] See for example, N. J. Pullman, *Matrix Theory and its Applications* (Marcel Dekker, Inc., New York, 1976)

[86] Y. Aharonov and D. Bohm, Phys. Rev. **115**, 485 (1959)

[87] S. Olariu and I. Popescu, Rev. Mod. Phys. **57**, 339 (1985)

[88] D. Stelitano, Phys. Rev. D **51**, 5876 (1995)